COMPTONIZATION AND THE SHAPING OF X-RAY SOURCE SPECTRA: MONTE CARLO CALCULATIONS

LEV A. POZDNYAKOV and IL'YA M. SOBOL'

Keldysh Institute of Applied Mathematics, USSR Academy of Sciences, Moscow

and

RASHID A. SYUNYAEV

Institute for Space Research, USSR Academy of Sciences, Moscow

Contents

1 Introduction

Astrophysicists have grown accustomed to Thomson-scattering effects. For example, in view of the 1981 total eclipse it is timely to recall that when we observe the solar corona we are looking at photospheric radiation, scattered (and polarized) by coronal electrons. Scattering contributes strongly to the opacity of matter in stellar interiors, and it proves to be an important factor in the photospheres of hot giant stars.

In all these situations the frequency change that the photons undergo as they are scattered has generally been neglected. The only occasion to allow for the frequency shift in classical theoretical astrophysics has been in treating the influence of electron scattering upon emission and absorption line profiles in the spectra of celestial bodies. Dirac in 1925 calculated the broadening of an emission line due to scattering by Maxwellian electrons. Chandrasekhar discussed in his classic book (1950) the problem of how an emission spectrum will evolve as the photons lose energy by recoil when they are scattered by free electrons.

If photons of energy† $h\nu \ll mc^2$ are scattered by Maxwellian electrons having $kT_e \ll mc^2$, the frequency shift will be very small [$\Delta\nu/\nu \sim \pm v_e/c \sim (kT_e/mc^2)^{1/2}$ because of the Doppler effect, or $\Delta\nu/\nu \sim -h\nu/mc^2$ through recoil]; but if the scattering process is repeated many times, the small amounts of energy exchanged between the electrons and photons can build up and give rise to substantial effects.

In hot, rarefied plasma, multiple scattering will control the rate of energy exchange between the electrons and the radiation field, and will generate certain specific emission spectra. The energy losses to bremsstrahlung and to recombination radiation are in fact proportional to the square of the plasma density, whereas the Thomson scattering probability is proportional only to the density itself, so in order for Compton losses to predominate the plasma must be tenuous. Moreover, for free–free absorption the Rosseland cross section is proportional to $T_e^{-3.5}$. Clearly Comptonization will be dominant in high-temperature plasma.

Thomson scattering conserves the number of photons (for the time being we shall neglect photon production by the double Compton effect; see Sec. 4.3); hence in the problem at hand we cannot do without extra photon sources. Photons could be supplied, for instance, by the plasma's own bremsstrahlung or cyclotron radiation, by the double Compton effect, by the synchrotron radiation of relativistic electrons in magnetic fields concentrated in the same volume, or by the emission of a central source that contains denser plasma. These photons will be redistributed over the spectrum. If $4kT_e > h\bar{\nu}$, then energy will be withdrawn from the electrons and transferred to the photons; conversely, if $h\bar{\nu} \geqslant 4kT_e$ the radiation will serve to heat the electrons, as exemplified by Figure 1. In the event of a very large optical depth, the Comptonization process will result in a Wien

†Throughout m denotes the electron mass; c, the velocity of light; h, k, the Planck and Boltzmann constants.

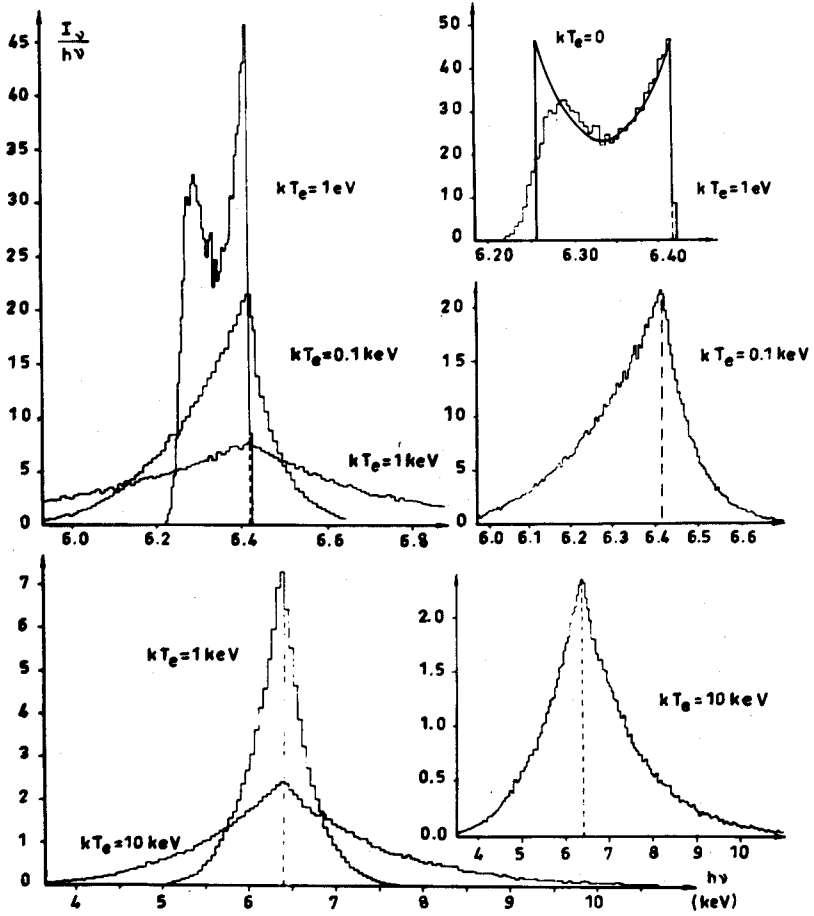

Figure 1 Profiles of the iron x-ray line at $h\nu_0 = 6.4$ keV after a single scattering by Maxwellian electrons of specified temperature (nonrelativistic plasma). When $h\nu \gg kT_e$ the profile broadens and shifts downward along the energy axis, mainly because of the recoil effect. In the range $4kT_e < h\nu < (kT_e \cdot mc^2)^{1/2}$, the Doppler effect broadens the lines but the recoil effect lowers the average energy of the photons. For $h\nu < 4kT_e$ the Doppler effect raises the average photon energy during the scattering process and the right wing of the line becomes stronger than the left one. The radiation serves to withdraw energy from the electrons (see Sec. 3.3.3).

radiation spectrum having the specified number of photons and a radiation temperature $T_r = T_e$.

A vital step forward in developing the theory of Comptonization was taken in 1949, when Kompaneets (1956) derived the kinetic equation that describes how the radiation field will interact with Maxwellian electrons. Then in the 1960s detailed studies were made of the inverse Compton effect, wherein the Doppler effect raises the energy of low-frequency photons undergoing single scattering by ultrarelativistic electrons (Ginzburg and Syrovatskiĭ 1974, Felten and Morrison 1966, Jones 1968, Blumenthal and Gould 1970). This process has turned out to be one of the chief mechanisms in high-energy astrophysics for producing hard radiation spectra.

When the primordial background radiation that permeates the whole universe was discovered it became clear that *Comptonization—the change in the spectrum of radiation due to multiple scattering of photons by thermal electrons*—must have played a crucial role in interactions between matter and radiation in the early universe (Weymann 1967, Zel'dovich and Syunyaev 1969, Syunyaev and Zel'dovich 1970, Illarionov and Syunyaev 1974*a, b*). The process captured the interest of physicists as well (Woodward 1970, Cooper 1971).

Cosmology confronts the researcher with a problem in which the plasma and radiation-field parameters are independent of the coordinates: they depend only on time. For this homogeneous problem a number of most important results have been obtained to show how radiation spectra should evolve [see the reviews by Danese and De Zotti (1977) and by Syunyaev and Zel'dovich (1980)].

It was soon realized that Comptonization also plays a most important part in molding the spectra of compact x-ray sources (Zel'dovich and Shakura 1969, Illarionov and Syunyaev 1972, Felten and Rees 1972). These objects furnished astrophysicists with conditions perfect for Comptonization to work: high temperatures ($kT_e \approx 1$–100 keV), plasma having a large depth with respect to Thomson scattering ($\tau_T \approx 1$–100), and availability of photon sources (dense plasma zones, intrinsic bremsstrahlung from the plasma, gyroline emission).

In the first attempts to calculate the spectra of x-ray sources (Zel'dovich and Shakura 1969, Illarionov and Syunyaev 1972) the results of the homogeneous problem (applicable to cosmology) were carried over in naive fashion to the context of spatially bounded plasma clouds, where the principal role is played by the distribution of photons with respect to their time for escape from the source. The photons in such a cloud will suffer

differing numbers of collisions, with decisive effects upon the spectrum of the radiation produced by Comptonization and emerging from the plasma cloud—a situation illustrated in Figure 2.

Valuable progress was made when it was understood that the radiation spectrum formed through Comptonization of low-frequency photons in a hot thermal plasma cloud may be described by a power law (Katz 1976; Shapiro *et al.* 1976; Pozdnyakov *et al.* 1976, 1977; Syunyaev and Titarchuk 1980). It was found that Comptonization by Maxwellian electrons can explain the power-law x-ray spectra observed in galaxy nuclei and quasars (see Figure 3). If we should now observe a power-law radiation spectrum somewhere, we no longer have to call it nonthermal and seek mechanisms for accelerating relativistic particles with a power-law energy distribution. The hot Maxwellian plasma in accretion disks (Figure 4) or in material infalling toward neutron stars might well give rise to power-law radiation spectra. For $kT_e \ll mc^2$, $\tau_T \gg 1$, and in the ultrarelativistic case for $kT_e \gg mc^2$, $\tau_T < 1$, these spectra are adequately described by the analytic expressions set forth in Sec. 4 of this review. In mildly relativistic plasma ($kT_e \sim mc^2$), however, it is hard to treat the problem analytically.

One finds that the required spectra of plasma with $kT_e \sim mc^2$ can be simulated more easily by the Monte Carlo method. The exposition of the Monte Carlo technique given in Sec. 9 will, we trust, enable anyone interested to retrace our path and to explore further the operation of Comptonization processes.†

To conclude this Introduction let us summarize the chief astrophysical objects where the spectrum formation mechanism that we shall discuss should be able to work (Figure 5).

The first example is an accretion disk around a *black hole*. The plasma flowing over from the companion star or entering the black hole from surrounding space will have a pronounced angular momentum. As a result it will not fall in radially, but at a certain radius it will form a gaseous ring around the gravitating center. Turbulent viscosity will spread the ring out into a disk, whose material will move toward the gravitating center along gradual spiral trajectories. During this motion gravitational energy will naturally be released, heating the disk surface to high temperatures (Pringle and Rees 1972, Shakura and Syunyaev 1973). Many astrophysicists believe that disks of just this kind are responsible for the x rays emitted by the source Cygnus X-1 (Liang and Price 1977, Eardley *et al.*

†We are indebted to the Polish scientist W. Wielczewski for an important remark which enabled us to improve the calculation procedure described in Sec. 9.

1978) as well as by quasars and galaxy nuclei (Lynden-Bell 1969, Lynden-Bell and Rees 1971, Shakura and Syunyaev 1976, Lightman *et al.* 1978). The x rays would be generated in a zone smaller than 10 R_g [a black hole of mass M will have a gravitational radius $R_g = 2GM/c^2 = 3(M/M_\odot)$ km]. Maximum energy release should occur within the belt $5 < R/R_g < 10$, and the disk should have there its smallest optical depth for Thomson scattering (Shakura and Syunyaev 1976, Syunyaev 1983). Disk accretion is a highly efficient mechanism for producing energy: as the accreting matter falls inward about 10 percent of its rest mass will be liberated as radiation. Even so, in order to yield as much energy as we observe in, say, the quasar 3C 273, about one earth mass would have to fall into the black hole every three seconds.

When disk accretion takes place onto a *neutron star* with a comparatively weak magnetic field ($H < 10^{10}$ gauss), half the energy released will be emitted by the extended accretion disk but the other half will come from a narrow boundary layer near the surface of the star, within which the velocity of the infalling material drops from the Keplerian value $v_\varphi = \sqrt{GM/R} = 80{,}000$ km/sec to the relatively modest rotational speed of the spinning stellar surface. It is in this layer that the plasma will reach its highest temperatures coupled with comparatively low density, and Comptonization will proceed efficiently. At the same time the neutron-star surface will act as a source of the low-frequency photons required to carry off energy by Comptonization. One interesting feature of the process is that some of the energetic photons from the hot zone will diffuse down into the dense zones of the neutron-star atmosphere, heating them. The atmosphere will then give off this extra energy in the form of low-frequency radiation.

If the magnetic field of the neutron star is strong enough ($H \approx 10^{12}$–10^{13} gauss), it will halt the accreting stream at large distances from the star and will channel the accretion, directing the flow toward the magnetic-pole regions. Close to the surface the material will speed up to $\approx 0.4c$; the kinetic energy will be liberated in a shock wave, where Comptonization will take place (Basko and Syunyaev 1976, Lyubarskiĭ and Syunyaev 1982).

Hot plasma zones should also develop in the shock waves formed near the surface of a *white dwarf* undergoing spherically symmetric accretion (DeGregoria 1974, Katz and Salpeter 1974, Fabian *et al.* 1976, Kylafis and Lamb 1979) and in an expanding *supernova envelope* (Weaver and Chapline 1974, Colgate 1975, Imshennik and Morozov 1981); indeed anywhere that we find rarefied, high-temperature gas, Comptonization

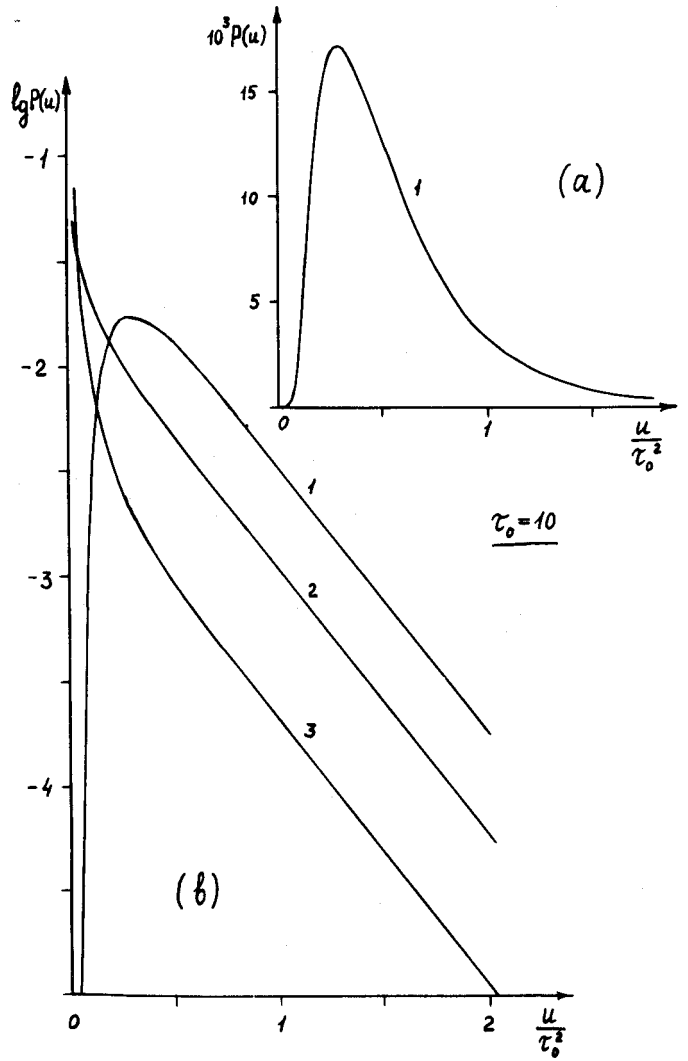

Figure 2 The distribution $P(u)$ of photons with respect to their escape time from a spherical plasma cloud whose Thomson-scattering optical depth $\tau = 10$ (Syunyaev and Titarchuk 1980). *a*) The cloud has a central photon source which at time $t = 0$ emits a momentary pulse of radiation. The number $u = \sigma_T N_e ct$ of scatterings which the photons undergo in the cloud represents a dimensionless time. *b*) Dependence of $P(u)$ on the distribution of photon sources: (*1*) source at center of cloud; (2) sources distributed uniformly over cloud; (*3*) cloud embedded in an external field of isotropic low-frequency radiation whose photons enter the cloud and are scattered several times before leaving it. Significantly, the asymptotic curves for large u are entirely similar in all cases; it is this limiting $P(u)$ relation which produces the power-law radiation spectra that result from Comptonization (see Sec. 4.1).

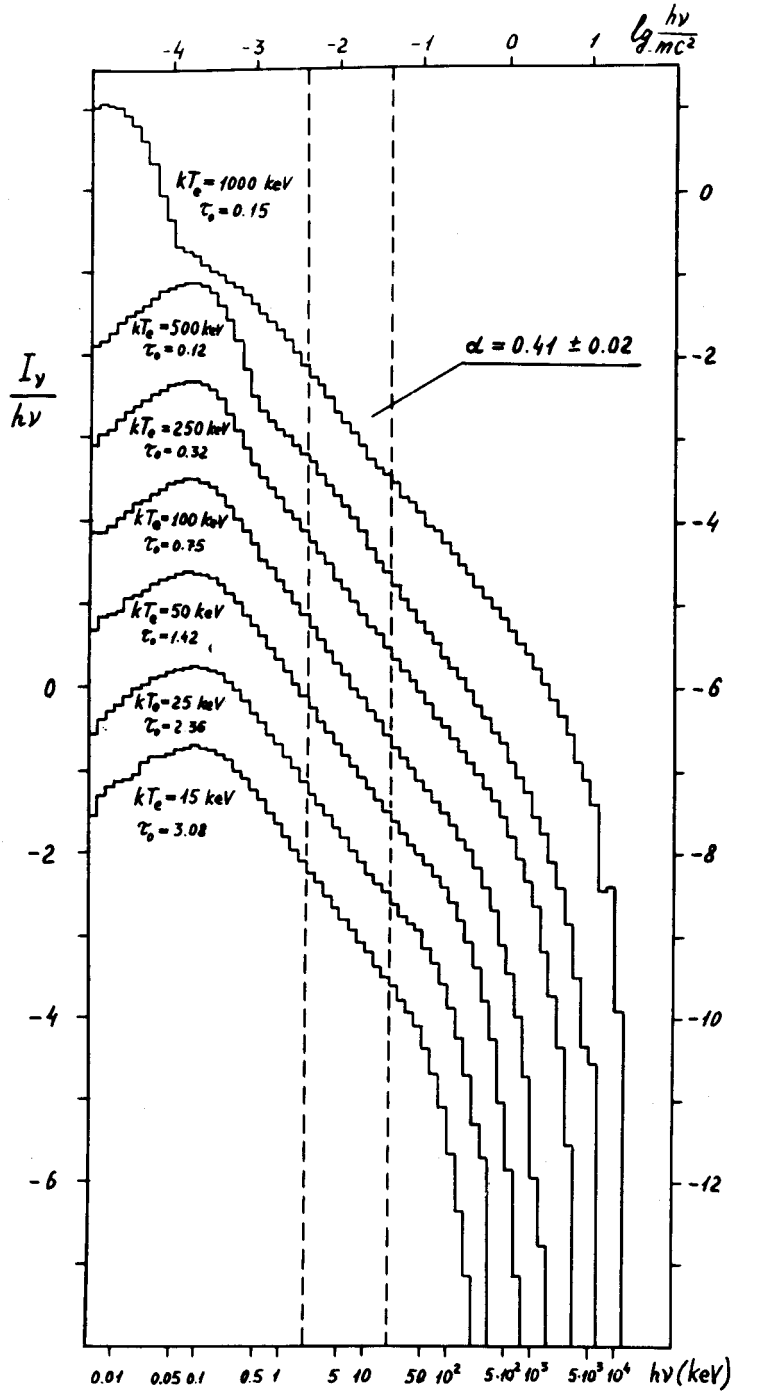
$\lg \frac{h\nu}{mc^2}$
-4
-3
-2
-1
0
1
$kT_e = 1000$ keV
$\tau_0 = 0.15$
$kT_e = 500$ keV
$\tau_0 = 0.12$
$kT_e = 250$ keV
$\tau_0 = 0.32$
$kT_e = 100$ keV
$\tau_0 = 0.75$
$kT_e = 50$ keV
$\tau_0 = 1.42$
$kT_e = 25$ keV
$\tau_0 = 2.36$
$kT_e = 15$ keV
$\tau_0 = 3.08$
$\alpha = 0.41 \pm 0.02$
$\frac{I_\nu}{h\nu}$
0
-2
-4
-6
-8
-10
-12
0.01
0.05
0.1
0.5
1
5
10
50
10^2
$5 \cdot 10^2$
10^3
$5 \cdot 10^3$
10^4
$h\nu$ (keV)

should be the primary mechanism for relieving the electrons of their energy and forming the radiation spectrum.

One should take multiple scattering, and thus Comptonization, into account even when considering the inverse Compton effect of low-frequency photons upon the relativistic electrons present in the radio-emitting clouds in *radio galaxies* and *quasars* (Rees 1967).

A final word about the geometry of the plasma clouds. We shall deal with isothermal flat disks and spheres of uniform density (Figure 6a). The low-frequency photon sources then may be located in the central plane of the disk (or at the center of the sphere), or they may be distributed uniformly throughout the disk or even outside (Figure 6b). It is interesting to find (Sec. 4.2.2, Figure 26) that the hard-radiation spectrum resulting from Comptonization is insensitive to the spatial distribution of the low-frequency photon sources.

2 Basic Equations

2.1 *Compton Scattering*

Assume that a photon of energy $h\nu$ and momentum $(h\nu/c)\mathbf{\Omega}$ is scattered by an electron of energy γmc^2 and momentum $\mathbf{p} = \gamma m\mathbf{v}$, with $\gamma = (1 - v^2/c^2)^{-1/2}$. Let $h\nu'$ and $(h\nu'/c)\mathbf{\Omega}'$ denote the energy and momentum of the photon after the scattering event.

2.1.1 Photon Frequency Shift By introducing the electron and photon four-momenta $p_4 = (\mathbf{p}', i\gamma mc)$, $k_4 = (h\nu\mathbf{\Omega}/c, ih\nu/c)$ prior to the scattering event and $p_4' = (\mathbf{p}', i\gamma' mc)$, $k_4' = (h\nu'\mathbf{\Omega}'/c, ih\nu'/c)$ afterward, one can easily find how the frequency of the photon will change when it is

Figure 3 A simulation of the x-ray spectrum of the quasar 3C 273. The x rays are regarded as generated by Comptonization of low-frequency blackbody radiation of temperature $kT_r = 0.05$ keV (except for the top curve, for which $kT_r = 0.005$ keV) in an accretion disk containing hot Maxwellian electrons ($T_e \gg T_r$). In these calculations the photon sources are confined to the central plane of the disk. Each spectrum is labeled with the electron temperature and the disk optical depth with respect to Thomson scattering. In the classical x-ray range ($2 < h\nu < 20$ keV) the spectrum obeys a power law for every case computed: the spectral flux density I_ν [Jy] $\propto \nu^{-\alpha}$, in agreement with the *HEAO A2* measurements (Worrall *et al.* 1979). For $h\nu > 3kT_e$ the spectrum approaches the Wien law $I_\nu \propto \nu^3 \exp(-h\nu/kT_e)$. As T_e rises, the spectrum hardens and its power-law segment becomes larger. One can evaluate T_e only from measurements in this high-energy range ($h\nu > 3kT_e$); the data presently available (2–20 keV) are inadequate to determine either the temperature or the optical depth of the radiating plasma. Figure 27 (Sec. 4.2) shows the results obtained by calculating the angular distribution of photons emerging from a disk with the same T_e and τ_0 values as in the third curve of this figure, for several energy ranges, while Figure 30 illustrates how the hard radiation of a disk will be polarized (as calculated in the Thomson approximation). Polarization effects have been neglected in calculating these spectra; while they would alter the numerical results, the qualitative behavior would remain the same.

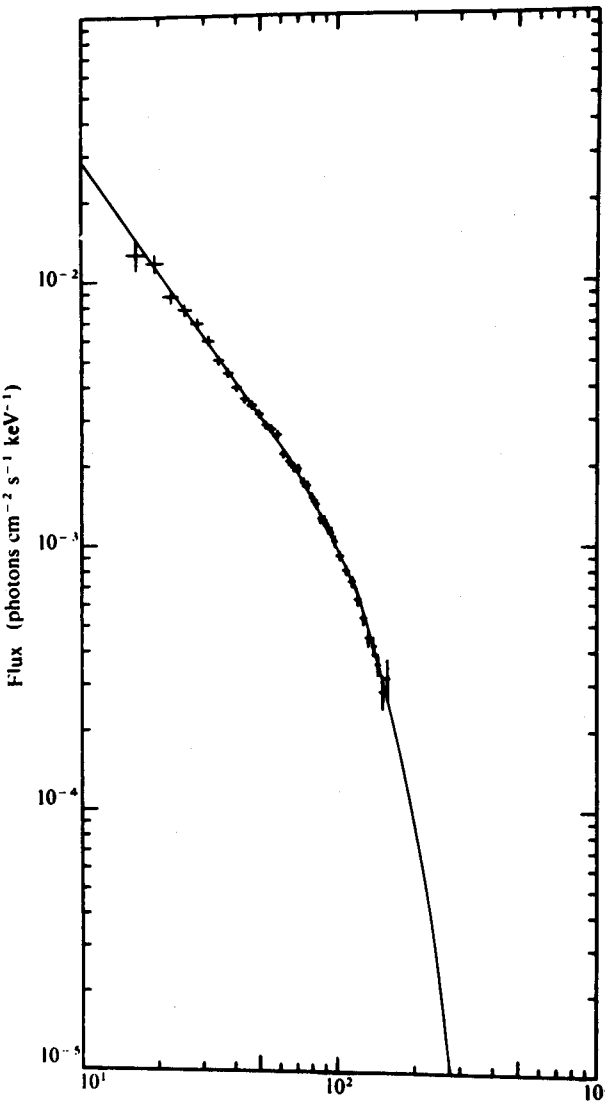

Figure 4 *Crosses*, the x-ray spectrum of Cygnus X-1 according to balloon measurements by J. Trümper's group at the Max-Planck-Institut near Munich. *Curve*, analytic solution obtained by Syunyaev and Titarchuk (1980) for $\alpha = 0.57$, $\gamma = 2$, $kT_e = 26.5$ keV. For a disk geometry, the corresponding Thomson-scattering optical depth of the disk would be $\tau_0 = 2$ (see Sec. 4.1); for spherical geometry, $\tau_0 = 5$.

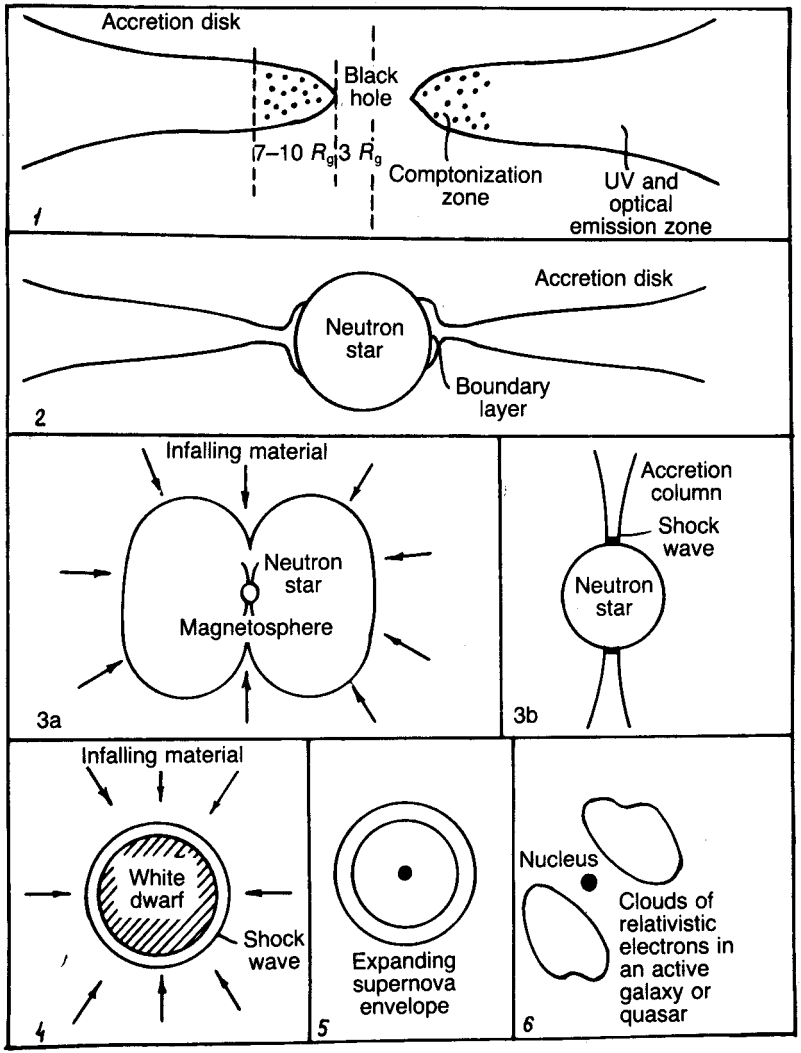

Figure 5 The principal astrophysical objects in which the Comptonization mechanism should operate efficiently.

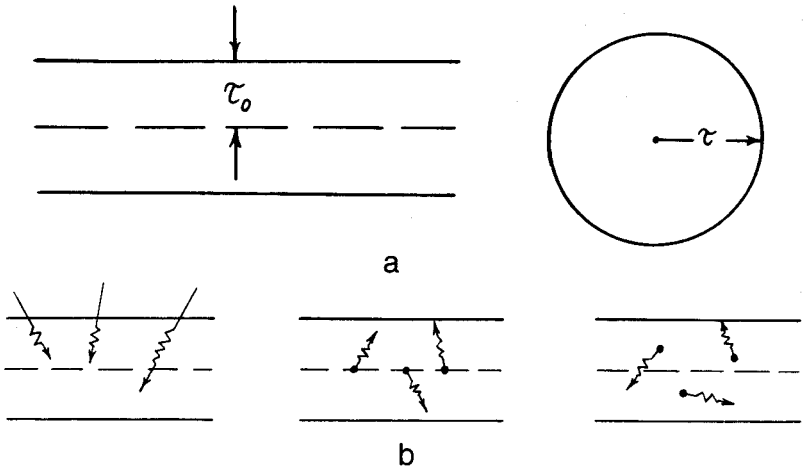

Figure 6 *a*) Geometry of the rarefied plasma clouds (a disk and a sphere) on which the calculations are based. *b*) Several cases illustrating the spatial distribution of low-frequency photon sources: outside a disk, in its central plane, and uniformly distributed over the disk.

scattered [see, for example, Akhiezer and Berestetskiĭ (1969)]. In fact,

$$p_4 + k_4 = p_4' + k_4'. \tag{2.1}$$

Squaring this relation and noting that $p_4^2 = p_4'^2 = -m^2c^2$ while $k_4^2 = k_4'^2 = 0$, we see that

$$p_4 k_4 = p_4' k_4'. \tag{2.2}$$

On the other hand, if we multiply Eq. (2.1) by k_4' we find

$$p_4' k_4' = p_4 k_4' + k_4 k_4', \tag{2.3}$$

or by Eq. (2.2),

$$p_4 k_4 = p_4 k_4' + k_4 k_4'.$$

Defining $\mu = \boldsymbol{\Omega} \cdot \mathbf{v}/v$, $\mu' = \boldsymbol{\Omega}' \cdot \mathbf{v}/v$, and the scattering angle $\alpha = \cos^{-1}(\boldsymbol{\Omega} \cdot \boldsymbol{\Omega}')$, we may therefore write

$$\frac{\nu'}{\nu} = \frac{1 - \mu v/c}{1 - \mu' v/c + (h\nu/\gamma mc^2)(1 - \cos\alpha)}. \tag{2.4}$$

If the photon is scattered by an electron at rest ($v = 0$), its frequency will change solely because of the *recoil* effect:

$$\frac{\nu'}{\nu} = \frac{1}{1 + (h\nu/mc^2)(1 - \cos\alpha)}. \tag{2.5}$$

In the case of a photon with $h\nu \ll mc^2$ we will have $\Delta\nu/\nu = -(h\nu/mc^2)(1 - \cos\alpha)$. If instead the electrons are traveling at high speed, the *Doppler effect* will play the dominant role in changing the frequency of low-energy photons. For in a reference frame comoving with the scattering electron, the photon frequency prior to the scattering event will be $\nu_0 = \gamma\nu(1 - \mu v/c)$, and if $h\nu_0 \ll mc^2$, we may neglect the frequency shift of the scattered photon in the electron rest frame: $\nu_0' \approx \nu_0$. Reverting to the laboratory reference frame, we obtain

$$\nu' = \frac{\nu_0'}{\gamma(1 - \mu' v/c)} \approx \frac{\nu_0}{\gamma(1 - \mu' v/c)} = \nu \cdot \frac{1 - \mu v/c}{1 - \mu' v/c}, \tag{2.6}$$

which will agree with Eq. (2.4) if the condition $h\nu/\gamma mc^2 \ll 1$ holds. In the nonrelativistic limit $v/c \ll 1$, Eq. (2.6) gives

$$\frac{\nu' - \nu}{\nu} = \frac{v}{c}(\mu' - \mu) + \frac{v^2}{c^2}\mu'^2. \tag{2.7}$$

2.1.2 Scattering Cross Section The differential cross section for Compton scattering is expressed by the formula [see, for example, Akhiezer and Berestetskiĭ (1969)]

$$\frac{d\sigma}{d\Omega'} = \frac{r_e^2}{2\gamma^2} \frac{X}{(1 - \mu v/c)^2} \left(\frac{\nu'}{\nu}\right)^2, \tag{2.8}$$

where the function

$$X = \frac{x}{x'} + \frac{x'}{x} + 4\left(\frac{1}{x} - \frac{1}{x'}\right) + 4\left(\frac{1}{x} - \frac{1}{x'}\right)^2,$$

$$x = \frac{2h\nu}{mc^2}\gamma\left(1 - \mu\frac{v}{c}\right), \qquad x' = \frac{2h\nu'}{mc^2}\gamma\left(1 - \mu'\frac{v}{c}\right);$$

$r_e = e^2/mc^2$ is the classical electron radius. In the nonrelativistic limit,

$$\frac{d\sigma}{d\Omega'} = \frac{r_e^2}{2}(1 + \cos^2\alpha). \tag{2.9}$$

The total scattering cross section is given by the Klein–Nishina formula:

$$\sigma = \frac{2\pi r_e^2}{x} \times \left[\left(1 - \frac{4}{x} - \frac{8}{x^2}\right)\ln(1 + x) + \frac{1}{2} + \frac{8}{x} - \frac{1}{2(1 + x)^2}\right]. \tag{2.10}$$

In particular, in the nonrelativistic limit ($x \ll 1$)

$$\sigma = \frac{8\pi}{3} r_e^2(1 - x) = \sigma_T(1 - x), \tag{2.11}$$

while in the ultrarelativistic case ($x \gg 1$)

$$\sigma = 2\pi r_e^2 x^{-1}(\ln x + \tfrac{1}{2}). \tag{2.12}$$

2.1.3 Photon Free Path The probability that a photon will be scattered within a path of length dl by a directed beam of electrons having a density $N_e(\mathbf{v})$ and moving at velocity $\mathbf{v}$ is expressed by

$$d\pi = \left(1 - \mu\frac{v}{c}\right)\sigma(x)N_e(\mathbf{v})\,dl \tag{2.13}$$

[see, for example, Jauch and Rohrlich (1955), Akhiezer and Berestetskiĭ (1969), Landau and Lifshits (1976)]. In view of the factor $(1 - \mu v/c)$ the effective cross sections

$$\sigma_{\text{eff}} = \left(1 - \mu\frac{v}{c}\right)\sigma(x), \qquad \frac{d\sigma_{\text{eff}}}{d\Omega'} = \left(1 - \mu\frac{v}{c}\right)\frac{d\sigma}{d\Omega'} \tag{2.14}$$

are often introduced, with $\sigma(x)$ given by Eq. (2.10) and $d\sigma/d\Omega'$ by Eq. (2.8).

From the scattering probability one can readily calculate the mean free

path $\bar{\lambda}$ of a photon in plasma whose electrons have any desired isotropic distribution $N_e(\mathbf{v})$ with respect to momentum:

$$\bar{\lambda} = \frac{4\pi \int_0^\infty N_e(p)p^2 dp}{2\pi N_e \int_0^\infty N_e(p)p^2 \int_1^{-1} \sigma(x)(1 - \mu v/c)d\mu\, dp}. \quad (2.15)$$

When we evaluate the expression (2.15) for the simplest case, a Maxwellian electron velocity distribution, we obtain the results presented in Table I and in Figure 7.

Several simple asymptotic relations can be derived (see also the expansions in the Appendix). In the case $h\nu \ll mc^2$, $kT_e \ll mc^2$, if we substitute into Eq. (2.15) the cross section (2.11) and the distribution $N_e(p) = N_e(2\pi mkT_e)^{-3/2} \exp(-p^2/2mkT_e)$ and then integrate, we find that

$$1/\bar{\lambda} = \sigma_T N_e[1 - 2(h\nu/mc^2) - 5(h\nu/mc^2)(kT_e/mc^2)]. \quad (2.16)$$

In the limit where $h\nu kT_e \ll (mc^2)^2$ but $kT_e \gg mc^2$, we again take the cross section (2.11) and adopt a Maxwellian distribution $N_e(p) = BN_e \exp(-\gamma mc^2/kT_e)$ for the ultrarelativistic electrons (so that $\langle \gamma mc^2 \rangle = 3kT_e$), obtaining

$$1/\bar{\lambda} = \sigma_T N_e[1 - 8(h\nu/mc^2)(kT_e/mc^2)]. \quad (2.17)$$

Here B is a normalizing constant, depending only on T_e.

In the ultrarelativistic limit $h\nu \gg mc^2$, $kT_e \gg mc^2$, if we write the cross section in the form (2.12) and assume that the electrons have a Maxwellian distribution, we find that

$$\frac{1}{\bar{\lambda}} = \frac{3}{16}\sigma_T N_e \frac{mc^2}{h\nu}\frac{mc^2}{kT_e}\left[\ln\left(4\frac{h\nu}{mc^2}\frac{kT_e}{mc^2}\right) + 0.077\right]. \quad (2.18)$$

And finally, in the event that $h\nu \gg mc^2$ but $kT_e \ll mc^2$ we will have

$$\frac{1}{\bar{\lambda}} = \frac{3}{8}\sigma_T N_e \frac{mc^2}{h\nu}\left(\ln\frac{2h\nu}{mc^2} + \frac{1}{2} + \frac{kT_e}{mc^2}\right)\left(1 - \frac{3}{2}\frac{kT_e}{mc^2}\right). \quad (2.19)$$

The mean free path will lengthen markedly as the plasma temperature rises.

Table I Photon Mean Free Path for Compton Scattering

The quantity $\log(\bar{\lambda}/\lambda_T)$ is tabulated as a function of the photon energy and the plasma temperature; $\lambda_T = 1/\sigma_T N_e$.

$\log \frac{h\nu}{mc^2}$	kT_e [keV]								
	0	10	50	100	150	200	250	300	400
−2.4	0.00350	0.00368	0.00440	0.00538	0.00642	0.00751	0.00862	0.00975	0.0120
−2.0	.00870	.00913	.0109	.0132	.0157	.0183	.0209	.0235	.0287
−1.6	.0213	.0223	.0264	.0317	.0372	.0428	.0483	.0537	.0644
−1.2	.0503	.0524	.0610	.0718	.0825	.0930	.103	.113	.132
−0.8	.110	.114	.129	.148	.165	.181	.197	.211	.238
−0.4	.216	.221	.242	.266	.289	.311	.331	.350	.385
0.0	.362	.369	.396	.427	.456	.482	.507	.530	.572
0.4	.553	.561	.592	.629	.662	.693	.722	0.749	0.797
0.8	0.783	0.792	0.828	0.869	0.907	0.942	0.974	1.00	1.06
1.2	1.05	1.06	1.10	1.14	1.18	1.22	1.26	1.29	1.35
1.6	1.35	1.36	1.40	1.45	1.49	1.53	1.57	1.60	1.66
2.0	1.67	1.68	1.72	1.77	1.81	1.85	1.89	1.92	1.99
2.4	2.00	2.01	2.05	2.10	2.15	2.19	2.23	2.26	2.33

$\log \frac{h\nu}{mc^2}$	kT_e [MeV]								
	0.5	0.6	0.8	1.0	2.0	3.0	4.0	7.0	10.0
−2.4	0.0144	0.0167	0.0213	0.0259	0.0470	0.0658	0.0828	0.125	0.160
−2.0	.0339	.0390	.0488	.0582	.0992	.132	.161	.226	.275
−1.6	.0747	.0845	.103	.120	.187	.236	.276	.366	.430
−1.2	.149	.164	.193	.218	.313	.379	.431	.544	.622
−0.8	.262	.284	.323	.356	.478	.561	.624	0.759	0.851
−0.4	.416	.443	.492	.533	.681	0.779	0.853	1.01	1.11
0.0	.609	.642	.699	.748	0.920	1.03	1.11	1.29	1.40
0.4	0.839	0.877	0.943	0.998	1.19	1.31	1.40	1.59	1.71
0.8	1.10	1.15	1.22	1.28	1.49	1.62	1.71	1.91	2.04
1.2	1.40	1.44	1.52	1.58	1.80	1.94	2.04	2.24	2.37
1.6	1.71	1.76	1.84	1.90	2.13	2.27	2.38	2.58	2.72
2.0	2.04	2.09	2.17	2.24	2.47	2.62	2.72	2.93	3.07
2.4	2.38	2.43	2.51	2.58	2.82	2.97	3.08	3.29	3.43

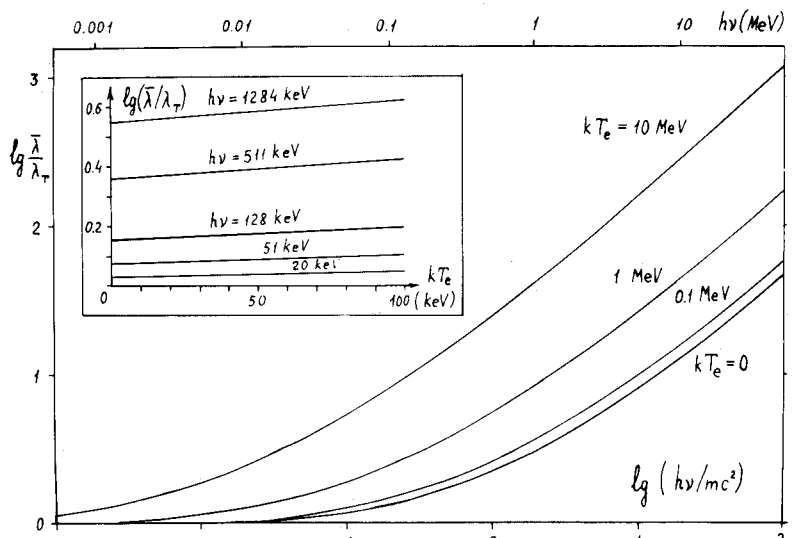

Figure 7 The mean free path $\bar{\lambda}$ with respect to Compton scattering for a photon of energy $h\nu$ in a Maxwellian plasma of temperature kT_e. All the curves are normalized to the free path $\lambda_T = 1/\sigma_T N_e$ computed in the Thomson approximation. The inset demonstrates that the corrections to the Thomson path length depend linearly on the plasma temperature for $kT_e/mc^2 \ll 1$.

2.2 *Energy Exchange between Plasma and Radiation during Scattering*

When photons are scattered by electrons with a Maxwellian momentum distribution, the average relative change in the photon frequency will be

$$\frac{\overline{\Delta\nu}}{\nu} = \bar{\lambda} \int \left(\frac{\nu'}{\nu} - 1\right)\left(1 - \mu\frac{v}{c}\right) \frac{d\sigma}{d\Omega'} N_e(p) p^2 dp \, d\Omega \, d\Omega', \quad (2.20)$$

where ν'/ν is expressed by Eq. (2.8) and the photon mean free path $\bar{\lambda}$ by Eq. (2.15). This frequency shift will be calculated presently for the nonrelativistic limiting case $h\nu \ll mc^2$, but first we give a simpler derivation of the quantity $\overline{\Delta\nu}/\nu$, valid in the event that $h\nu \ll kT_e$.

2.2.1 Braking of Electron by Radiation Field Consider an electron traveling at velocity $\mathbf{v}$ in a field of isotropic radiation with a blackbody spectrum corresponding to temperature T_r. Let the electron interact with the radiation by the Thomson scattering process. Because of the Doppler effect the

electron will perceive that the temperature of the radiation depends on direction:

$$T = \frac{T_r}{\gamma(1 - \mu_0 v/c)}, \tag{2.21}$$

the angle μ_0 being measured in the electron rest frame.

The radiation-pressure force exerted on the electron will be directed opposite to **v** and equal to

$$f = \frac{\sigma_T q}{c} = \frac{\sigma_T}{c} \int I(\mu_0)\mu_0 d\Omega_0 = \frac{2\pi\sigma_T}{c} \int_{-1}^{1} I(\mu_0)\mu_0 d\mu_0, \tag{2.22}$$

where $q = \int I(\mu_0)\mu_0 d\Omega_0$ represents the radiant energy flux incident on the electron; $I \equiv \int_0^\infty I_\nu d\nu$, with I_ν the blackbody radiation intensity.

We now introduce the radiant energy density $\mathcal{E}_r = bT_0^4$, where b is the Stefan–Boltzmann constant. In the electron rest frame

$$I = \frac{bT^4}{4\pi c} = \frac{bT_0^4}{4\pi c\gamma^4(1 - \mu_0 v/c)^4}, \tag{2.23}$$

so that†

$$f = \frac{\sigma_T \mathcal{E}_r}{2\gamma^4} \int_{-1}^{1} \frac{\mu_0 d\mu_0}{(1 - \mu_0 v/c)^4} = \frac{4}{3} \sigma_T \mathcal{E}_r \gamma^2 \frac{v}{c}. \tag{2.24}$$

The force (2.24) acts on the electron not only in its rest frame but also in the laboratory system, in which the radiation field is isotropic.

In the *nonrelativistic* case, $v \ll c$, $\gamma \approx 1$, and $f = -m\, dv/dt$; we will have

$$m \frac{dv}{dt} = -\frac{4}{3} \sigma_T \mathcal{E}_r \frac{v}{c}. \tag{2.25}$$

†This result clearly holds true whatever the spectrum of the radiation field.

Multiplying both sides of Eq. (2.25) by v, we obtain

$$\frac{d}{dt}\left(\frac{mv^2}{2}\right) = -\frac{8}{3}\frac{\sigma_T \mathcal{E}_r}{mc}\left(\frac{mv^2}{2}\right); \tag{2.26}$$

thus the energy of the electron will decay exponentially as

$$E = E_0 \exp\left(-\frac{8}{3}\frac{\sigma_T \mathcal{E}_r}{mc}t\right) \tag{2.27}$$

with a characteristic time scale $t_c = \frac{3}{8}\, mc/\sigma_T E_r$.

Equation (2.26) can readily be averaged over a Maxwellian electron velocity distribution. The averaging is equivalent to replacing $mv^2/2$ by the mean particle energy $\frac{3}{2}kT_e$. Then

$$\frac{dT_e}{dt} = -\frac{8}{3}\sigma_T c \mathcal{E}_r \frac{kT_e}{mc^2},$$

so that the electron temperature will fall off as $T_e = T_0 \exp(-t/t_c)$. But as the electrons cool the radiation energy density will rise:

$$\frac{dE_r}{dt} = -\frac{3}{2}N_e\frac{d(kT_e)}{dt} = \frac{4\sigma_T \mathcal{E}_r N_e kT_e}{mc},$$

and accordingly, provided $T_e(t) \equiv \text{const}$,

$$\mathcal{E}_r = \mathcal{E}_0 \exp\left(\frac{4\sigma_T N_e kT_e}{mc}t\right). \tag{2.28}$$

The photon–electron collision frequency is equal to $\sigma_T N_e c$, and the number of photons will be conserved. Equation (2.28) therefore states that, on the average, the energy of a photon will increase by

$$\frac{\overline{\Delta\nu}}{\nu} = 4\frac{kT_e}{mc^2} \tag{2.29}$$

every time it collides with an electron.

In the *relativistic* case, $f = d(\gamma mv)/dt$,

$$\frac{d}{dt} mc\sqrt{\gamma^2 - 1} = \frac{mc\gamma}{\sqrt{\gamma^2 - 1}} \frac{d\gamma}{dt},$$

and by Eq. (2.24)

$$\frac{d\gamma}{dt} = -\frac{4}{3} \frac{\sigma_T \mathcal{E}_r}{mc} (\gamma^2 - 1). \tag{2.30}$$

Equation (2.30) has a solution of the form $\gamma = [1 + A(t)]/[1 - A(t)]$, where

$$A(t) = \frac{\gamma_0 - 1}{\gamma_0 + 1} \exp\left(- \frac{8}{3} \frac{\sigma_T \mathcal{E}_r}{mc} t \right) = \frac{\gamma_0 - 1}{\gamma_0 + 1} \exp\left(- \frac{t}{t_c} \right) \tag{2.31}$$

(γ_0 denotes the initial γ-factor of the electron).

For the *ultrarelativistic* case $\gamma \gg 1$, Eq. (2.30) reduces to the familiar expression for the rate of energy loss by a relativistic electron in an isotropic radiation field:

$$\frac{d\gamma}{dt} = - \frac{4}{3} \frac{\sigma_T \mathcal{E}_r}{mc} \gamma^2,$$

$$\gamma = \frac{\gamma_0}{1 + (4\sigma_T \mathcal{E}_r \gamma_0 / 3mc)t} = \frac{\gamma_0}{1 + \gamma_0 t / 2t_c}. \tag{2.32}$$

As to the radiation energy density (recall that for monoenergetic electrons $mc^2 N_e d\gamma/dt = - d\mathcal{E}_r/dt$), according to Eq. (2.30) it will grow exponentially:

$$\frac{d\mathcal{E}_r}{dt} = \frac{4}{3} \sigma_T \mathcal{E}_r N_e c(\gamma^2 - 1),$$

so that

$$\mathcal{E}_r = \mathcal{E}_0 \exp[\tfrac{4}{3} \sigma_T N_e c(\gamma^2 - 1)t]. \tag{2.33}$$

In each scattering event the photon energy will increase, on the average, by an amount such that

$$\overline{\nu'} = \nu[1 + \tfrac{4}{3}(\gamma^2 - 1)]. \tag{2.34}$$

Equation (2.34) agrees both with the nonrelativistic law (2.29) and with the familiar ultrarelativistic expression

$$\overline{\nu'} = \tfrac{4}{3}\nu\gamma^2. \tag{2.35}$$

One can easily average Eq. (2.34) over a Maxwellian distribution; the result is expressed by Eq. (2.43) below. Figure 8 demonstrates how the two mean values $\overline{\nu'/\nu}$ and $\overline{\gamma}$ increase with kT_e.

2.2.2 Energy Exchange: the Case $h\nu \ll kT_e \ll mc^2$ Equation (2.29) can also be obtained by calculating the mean value $\langle \nu' - \nu \rangle$ directly. First let us take the case of a beam of low-frequency photons interacting with monoenergetic, isotropically distributed electrons. Then the quantity

$$\langle \nu' - \nu \rangle = \frac{1}{4\pi\sigma_T} \int \left(1 - \mu\frac{v}{c}\right) \frac{d\sigma}{d\Omega'} (\nu' - \nu) d\Omega \, d\Omega' \frac{dv}{v}. \tag{2.36}$$

Using Eq. (2.4), we may rewrite Eq. (2.8) in the form

$$\frac{d\sigma}{d\Omega'} = \frac{r_e^2}{2\gamma^2} \left[1 + \left(1 - \frac{1 - \cos\alpha}{\gamma^2(1 - \mu v/c)(1 - \mu' v/c)} \right)^2 + \frac{h^2\nu^2(1 - \cos\alpha)^2}{\gamma^2(mc^2)^2(1 - \mu' v/c)[1 - \mu' v/c + (h\nu/\gamma mc^2)(1 - \cos\alpha)]} \right] \times \left(\frac{1}{1 - \mu' v/c + (h\nu/\gamma mc^2)(1 - \cos\alpha)} \right)^2. \tag{2.37}$$

In the Thomson limit we may neglect the recoil effect, omitting the $(h\nu/\gamma mc^2)(1 - \cos\alpha)$ terms; then

$$\frac{d\sigma}{d\Omega'} = \frac{r_e^2}{2\gamma^2} \times \left[1 + \left(1 - \frac{1 - \cos\alpha}{\gamma^2(1 - \mu v/c)(1 - \mu' v/c)} \right)^2 \right] \frac{1}{(1 - \mu' v/c)^2}. \tag{2.38}$$

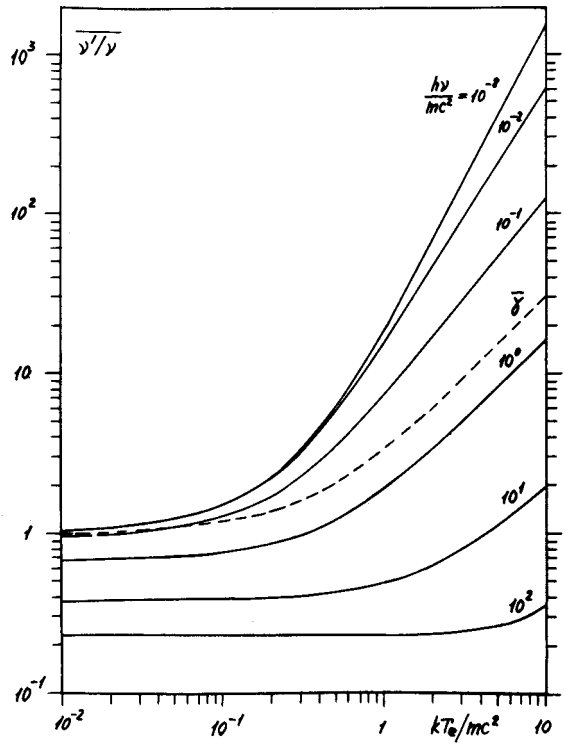

Figure 8 The average change $\overline{\nu'/\nu}$ in the frequency of monochromatic photons scattered by hot Maxwellian electrons and the mean energy $\bar{\gamma}$ of the electrons in the Maxwellian distribution, as functions of the electron temperature. The calculations have been performed for various $h\nu/mc^2$ ratios. When $h\nu \ll kT_e$, the predominant effect is the Doppler increase in frequency. On the contrary, if $h\nu \gg kT_e$ the frequency will decrease, due to the recoil effect. The curves for $h\nu/mc^2 = 10^{-8}$ and 10^{-2} differ: in the first case the calculations agree perfectly with the Thomson approximation [Eq. (2.26)], while in the second case the effects described by the Klein–Nishina formula become significant.

Since the scattering angle α satisfies the relations

$$\cos\alpha = \mu\mu' + \sqrt{1-\mu^2}\sqrt{1-\mu'^2}\cos(\varphi - \varphi'), \quad (2.39a)$$

$$\int_{\varphi}^{\varphi+2\pi} \cos\alpha \, d\varphi' = 2\pi\mu\mu', \quad (2.39b)$$

$$\int_{\varphi}^{\varphi+2\pi} \cos^2\alpha \, d\varphi' = \pi(3\mu^2\mu'^2 + 1 - \mu^2 - \mu'^2), \quad (2.39c)$$

$$\int_{\varphi}^{\varphi+2\pi} \cos^3 \alpha \, d\varphi' = \pi(5\mu^3\mu'^3 - 3\mu^3\mu' - 3\mu\mu'^3 + 3\mu\mu'), \quad (2.39d)$$

we can evaluate the integral (2.36) and several others to follow. It is convenient first to replace the $d\mathbf{\Omega}'$ integration by a $d\mu' d\varphi'$ integration and then to integrate over all directions of the electrons, that is, over $d\mu \, d\varphi$. If in Eq. (2.36) we take ν'/ν as given by Eq. (2.6) and use a differential cross section of the form (2.38), then the answer will have the form

$$\frac{\langle \nu' - \nu \rangle}{\nu} = \frac{4}{3}\left(\frac{v}{c}\right)^2 \gamma^2 = \frac{4}{3}(\gamma^2 - 1), \quad (2.40)$$

which naturally agrees with Eq. (2.34).

We would emphasize that the results given in this paragraph presuppose only that the *electrons* are distributed isotropically with respect to direction; the radiation may be as highly directive as desired. In deriving Eq. (2.34), however, we assumed that the *radiation* was isotropic; that result holds for a single electron traveling at velocity **v**.

It is also worth noting that if we integrate the expression (2.36) for a Rayleigh scattering function

$$\frac{d\sigma}{d\mathbf{\Omega}'} = \frac{r_e^2}{2}(1 + \cos^2 \alpha)$$

[corresponding to Eq. (2.38) when $v = 0$], we will not obtain the correct answer even if $v/c \ll 1$.

Equation (2.30) enables us to find the rate at which energy will be withdrawn from plasma by Comptonization of low-frequency radiation, whatever the electron temperature may be. For this purpose Eq. (2.30) has to be averaged over the relativistic Maxwellian distribution

$$dN_e = \frac{Ac^3p^2e^{-\gamma/\eta}}{(mc^2)^3} dp = A\gamma(\gamma^2 - 1)^{1/2}e^{-\gamma/\eta}d\gamma, \quad (2.41)$$

where A is a normalizing factor and the quantity $\eta = kT_e/mc^2$. In this manner we find that

$$\frac{d\mathcal{E}_r}{dt} = -N_e mc^2 \frac{d\langle\gamma\rangle}{dt} = \frac{4}{3}\sigma_T \mathcal{E}_r c \langle\gamma^2 - 1\rangle. \quad (2.42)$$

Here the mean values

$$\langle \gamma^2 - 1 \rangle = \frac{\int_1^\infty \gamma(\gamma^2 - 1)^{3/2} e^{-\gamma n} d\gamma}{\int_1^\infty \gamma(\gamma^2 - 1)^{1/2} e^{-\gamma n} d\gamma} = 3n(n + \langle \gamma \rangle), \quad (2.43)$$

$$\langle \gamma \rangle = \frac{\int_1^\infty \gamma^2(\gamma^2 - 1)^{1/2} e^{-\gamma n} d\gamma}{\int_1^\infty \gamma(\gamma^2 - 1)^{1/2} e^{-\gamma n} d\gamma} = \frac{3n\mathcal{K}_2(1/n) + \mathcal{K}_1(1/n)}{2n\mathcal{K}_1(1/n) + \mathcal{K}_0(1/n)}, \quad (2.44)$$

where the Macdonald functions $\mathcal{K}_p(1/n)$ are tabulated, for example, in Abramowitz and Stegun's handbook (1964). Equations (2.43), (2.44) reduce to the standard relations $\langle \gamma^2 - 1 \rangle \approx v^2/c^2 \approx 3n$, $\langle \gamma \rangle = \frac{3}{2}n + 1$ in the nonrelativistic case and $\langle \gamma^2 \rangle = 12n^2$ in the ultrarelativistic case, since $\langle \gamma \rangle = 3n$. Table II gives the values of these two quantities computed for a range of n; notice how quickly they approach the ultrarelativistic limit as n increases.

Table II Mean Electron Energy Parameters

$n = \frac{kT_e}{mc^2}$	$\langle \gamma \rangle$	$\langle \gamma^2 - 1 \rangle$	
0.025	1.04	0.08	2.67
0.05	1.08	0.17	2.67
0.1	1.17	0.38	2.67
0.2	1.36	0.94	2.83
0.3	1.58	1.69	2.93
0.4	1.81	2.65	3.02
0.5	2.05	3.83	3.11
0.6	2.30	5.22	3.17
0.7	2.56	6.85	3.23
0.8	2.83	8.71	3.29
1.0	3.37	13.1	3.37
1.2	3.93	18.5	3.45
1.5	4.78	28.2	3.51
2.0	6.22	49.3	3.61
3.0	9.15	109	3.70

2.2.3 The Case $kT_e \ll h\nu \ll mc^2$ Using the Rayleigh scattering function we obtain in this case

$$\frac{\langle \nu' - \nu \rangle}{\nu} = \frac{1}{\sigma_T} \int \left(\frac{\nu'}{\nu} - 1 \right) \frac{d\sigma}{d\Omega'} \, d\Omega' = -\frac{h\nu}{mc^2}, \tag{2.45}$$

since $\nu'/\nu = 1 - (1 - \cos\alpha)h\nu/mc^2$ [see Eq. (2.5)].

2.2.4 The Case $h\nu \ll mc^2$, $kT_e \ll mc^2$ The energy exchange due to the recoil and Doppler effects will be small in this nonrelativistic case: $\Delta\nu/\nu \ll 1$. The two effects are independent and to a first approximation combine linearly, so that

$$\frac{\langle \nu' - \nu \rangle}{\nu} = \frac{4kT_e - h\nu}{mc^2}. \tag{2.46}$$

2.3 Radiation-Pressure Force

2.3.1 Eddington Luminosity Limit Many x-ray sources have a luminosity approaching the critical Eddington value. Suppose that an electron is located at distance R from an object of luminosity L and mass M; then the radiation pressure will exert on it a force

$$\mathbf{f} = \frac{\sigma_T}{c} \mathbf{q} = \frac{\sigma_T L}{4\pi R^2 c} \frac{\mathbf{R}}{R}, \tag{2.47}$$

where $q = L/4\pi R^2$ is the flux density of radiant energy. A proton, on the other hand, will be subject to a gravitational force $f_{grav} = -(GMm_p/R^2)\mathbf{R}/R$. One may neglect the radiation-pressure force on the proton, since its scattering cross section

$$\sigma_p = \frac{8\pi}{3} \left(\frac{e^2}{m_p c^2} \right)^2 = \left(\frac{m}{m_p} \right)^2 \sigma_T$$

is insignificant; and the attractive force exerted on the electron will also be very small, as its mass is small. The electrons and protons in ionized hydrogen plasma are bound together by electrostatic forces, and charge separation is practically impossible. Both the forces mentioned above may be regarded as being applied to electron–proton pairs. Both, remarkably

enough, fall off as R^{-2} and are oppositely directed. They will be comparable to each other if

$$L_{cr} = \frac{4\pi GMm_p c}{\sigma_T} = \frac{2\pi R_g m_p c^3}{\sigma_T} = 1.3 \times 10^{38} \frac{M}{M_\odot} \text{ erg/sec.} \quad (2.48)$$

This is the critical luminosity, the Eddington limit.

If $L > L_{cr}$, no accretion can occur; radiation pressure will overwhelm the gravitational forces and should cause material to flow outward. If $L \ll L_{cr}$ the light pressure may be neglected; material can be accreted, and stars with internal energy sources and stable atmospheres can exist.

In plasma whose chemical elements have the normal cosmic abundance, there will be $(1 + X)/2 \approx 0.85$ electron for each nucleon (X represents the proportion of hydrogen by mass, and we assume here that complete ionization of helium and heavy elements will yield one electron for every two nucleons). The plasma pressure force will accordingly diminish by 15 percent, raising the value of the critical luminosity.

2.3.2 General Equation for All hν *and* kT$_e$ Equation (2.47) for the radiation-pressure force holds in the limit $h\nu \to 0$, $kT_e \to 0$. We shall obtain an expression for this force when $h\nu$, kT_e, and mc^2 have arbitrary ratios to one another. The corresponding values of the force calculated for various ratios $h\nu/mc^2$ and selected kT_e are given in Table III.

When a photon is scattered it will transfer to the scattering electron a momentum

$$\Delta \mathbf{p} = \frac{h\nu}{c} \mathbf{\Omega} - \frac{h\nu'}{c} \mathbf{\Omega}' \quad (2.49)$$

[we neglect certain induced effects; see Levich *et al.* (1972)]. Hence radiation of intensity $I_\nu(\mathbf{\Omega}, \nu)$ will impart to the electrons a force

$$\mathbf{f} = \int \left(\frac{h\nu}{c} \mathbf{\Omega} - \frac{h\nu'}{c} \mathbf{\Omega}' \right) \frac{I_\nu(\mathbf{\Omega}, \nu)}{h\nu} \times \left(1 - \mu \frac{v}{c} \right) \frac{d\sigma}{d\mathbf{\Omega}'} N(\mathbf{v}) d\mathbf{v}\, d\mathbf{\Omega}\, d\mathbf{\Omega}'\, d\nu. \quad (2.50)$$

Table III Radiation-Pressure Force

The quantity tabulated is the ratio of the force exerted by radiation of frequency $h\nu$ in plasma of temperature kT_e to the force from radiation of the same energy flux density in the limiting case $h\nu \to 0$, $kT_e \to 0$.

$\log \frac{h\nu}{mc^2}$	kT_e [keV]								
	0	10	50	100	150	200	250	300	400
−8.0	1.00	1.0	1.2	1.6	2.1	2.7	3.5	4.4	6.6
−2.4	0.981	1.0	1.2	1.6	2.0	2.6	3.3	4.1	5.9
−2.0	.969	1.0	1.2	1.5	1.9	2.4	3.0	3.7	5.1
−1.6	.926	0.96	1.1	1.4	1.7	2.0	2.4	2.9	3.9
−1.2	.833	.86	0.96	1.1	1.3	1.5	1.7	1.9	2.4
−0.8	.670	.68	.72	0.78	0.85	0.92	1.0	1.1	1.2
−0.4	.466	.47	.47	.48	.49	.50	0.51	0.53	0.55
0.0	.297	.29	.29	.28	.27	.27	.26	.26	.25
0.4	.186	.18	.17	.16	.15	.15	.14	.14	.12
0.8	.112	.11	.10	.095	.088	.082	.077	.073	.065
1.2	.0634	.062	.057	.052	.048	.044	.041	.038	.034
1.6	.0335	.033	.030	.027	.025	.023	.021	.019	.017
2.0	.0167	.016	.015	.013	.012	.011	.010	.0095	.0082
2.4	0.0080	0.0078	0.0071	0.0064	0.0058	0.0053	0.0048	0.0045	0.0038

$\log \frac{h\nu}{mc^2}$	kT_e [MeV]								
	0.5	0.6	0.8	1.0	2.0	3.0	4.0	7.0	10.0
−8.0	9.2	13	22	32	120	280	500	1500	3000
−2.4	8.1	11	18	25	78	150	230	470	720
−2.0	6.8	8.9	14	19	49	82	120	210	290
−1.6	4.9	6.1	8.6	11	24	36	47	75	96
−1.2	2.8	3.3	4.3	5.2	9.3	13	15	21	26
−0.8	1.4	1.5	1.8	2.0	3.0	3.7	4.2	5.1	5.7
−0.4	0.58	0.61	0.65	0.69	0.82	0.92	0.98	1.1	1.1
0.0	.25	.25	.24	.24	.23	.23	.22	.22	0.22
0.4	.12	.11	.10	.094	.072	.065	.059	.050	.046
0.8	.059	.055	.048	.043	.029	.023	.020	.015	.012
1.2	.030	.028	.023	.020	.013	.0098	.0080	.0053	.0042
1.6	.015	.014	.011	.0098	.0060	.0044	.0035	.0022	.0017
2.0	.0072	.0065	.0054	.0047	.0028	.0020	.0016	.00097	.00072
2.4	0.0034	0.0030	0.0025	0.0022	0.0013	0.00089	0.00071	0.00043	0.00032

Here $I_\nu(\mathbf{\Omega}, \nu)/h\nu$ represents the spectral number density of photons of frequency ν coming from the direction $\mathbf{\Omega}$, while $N(\mathbf{v})$ gives the distribution of electrons with respect to velocity and direction. Equation (2.37) describes the differential scattering cross section, and Eq. (2.4) relates ν' to ν. The values given in Table III have been calculated from Eq. (2.50) by the Monte Carlo method.

If the radiation is beamed, with $I_\nu(\mathbf{\Omega}, \nu) = I_\nu(\nu)\delta(\mathbf{\Omega} - \mathbf{\Omega}_0)$, and if the electrons are distributed isotropically, the radiation-pressure force will naturally be directed along the vector $\mathbf{\Omega}_0$ and equal in magnitude to

$$f = \frac{1}{c}\int\left(1 - \frac{\nu'}{\nu}\cos\alpha\right) \times \left(1 - \mu\frac{v}{c}\right)\frac{d\sigma}{d\mathbf{\Omega}'} I_\nu(\nu)d\nu\, N(v)d\mathbf{v}\, d\mathbf{\Omega}'. \quad (2.51)$$

The force can easily be calculated analytically from Eq. (2.51) in two limiting cases: *a*) $kT_e = 0$, $h\nu$ arbitrary; *b*) $h\nu \to 0$, kT_e arbitrary, so that the Thomson-scattering approximation applies.

2.3.3 Analytic Expression: $\mathrm{kT_e} = 0$ In the limit $v = 0$, Eq. (2.37) reduces to the standard relation

$$\frac{d\sigma}{d\mathbf{\Omega}'} = \frac{r_e^2}{2}\left(1 + \cos^2\alpha + \frac{h^2\nu^2(1 - \cos\alpha)^2}{m^2c^4[1 + (h\nu/mc^2)(1 - \cos\alpha)]}\right) \times \frac{1}{[1 + (h\nu/mc^2)(1 - \cos\alpha)]^2}. \quad (2.52)$$

With Eq. (2.5), Eq. (2.51) will then become

$$f = \frac{\pi r_e^2}{c}\int\left(1 - \frac{\cos\alpha}{1 + (h\nu/mc^2)(1 - \cos\alpha)}\right) \times \left(\frac{1 + \cos^2\alpha}{[1 + (h\nu/mc^2)(1 - \cos\alpha)]^2} + \frac{(h\nu/mc^2)^2(1 - \cos\alpha)^2}{[1 + (h\nu/mc^2)(1 - \cos\alpha)]^3}\right) \times I_\nu d\nu\, d\cos\alpha. \quad (2.53)$$

The integration over the scattering angle can be carried out; one obtains

$$f = \frac{3\sigma_T}{4c} \int \frac{1 + a}{a^3(1 + 2a)^3} \left(\frac{(1 + 2a)^3}{2a} (a^2 - 2a - 3) \ln (1 + 2a) + 3 + 17a + 31a^2 + 17a^3 - \frac{10}{3} a^4 \right) I_\nu d\nu, \quad (2.54)$$

where $a \equiv h\nu/mc^2$. In the limit $a \to 0$ we find asymptotically

$$\mathbf{f} = \frac{\sigma_T}{c} \int \left(1 - \frac{16}{5} \frac{h\nu}{mc^2} \right) I_\nu(\mathbf{\Omega}, \nu)\mathbf{\Omega}\, d\mathbf{\Omega}\, d\nu, \quad (2.55)$$

while in the Klein–Nishina limit, when $a \gg 1$,

$$\mathbf{f} = \frac{3\sigma_T}{8c} \int \frac{mc^2}{h\nu} \left[\ln \left(1 + \frac{2h\nu}{mc^2} \right) - \frac{5}{6} \right] I_\nu(\mathbf{\Omega}, \nu)\mathbf{\Omega}\, d\mathbf{\Omega}\, d\nu. \quad (2.56)$$

Equation (2.54) has been derived on the premise that the radiation consists of a highly directive beam. Clearly, however, radiation having any desired angular distribution may be regarded as a collection of beams. Partial forces would be directed along the individual beams, and one need only take a vector sum of those forces, as has been done in Eqs. (2.55) and (2.56).

Monte Carlo calculations have been performed for three different radiation beam patterns: *a*) a narrow beam; *b*) a surface on which $I_\nu(\mathbf{\Omega}) = \text{const}$, with $\mu \geq 0$; *c*) a surface on which $I_\nu(\mathbf{\Omega}) = A(\nu)(1 + 2\mu)$. Whatever the ratios between kT_e, $h\nu$, and mc^2, the resultant force depends only on the radiation spectrum, kT_e, and $\int I_\nu(\mathbf{\Omega})\mathbf{\Omega}\, d\mathbf{\Omega}$.

2.3.4 Analytic Expression: hν *Small,* kT$_e$ *Arbitrary* Taking in Eq. (2.50) a differential cross section of the form (2.38) and ν'/ν as given by

Eq. (2.6), we obtain for the case of isotropically distributed, monoenergetic electrons:

$$\mathbf{f} = \frac{r_e^2}{8\pi\gamma^2} \int \left(1 - \frac{1 - \mu v/c}{1 - \mu' v/c} \cos\alpha\right) \times \left[1 + \left(1 - \frac{1 - \cos\alpha}{\gamma^2(1 - \mu v/c)(1 - \mu' v/c)}\right)^2\right] \times \frac{1 - \mu v/c}{(1 - \mu' v/c)^2} I_\nu(\boldsymbol{\Omega})\boldsymbol{\Omega}\, d\boldsymbol{\Omega}\, d\nu\, d\boldsymbol{\Omega}'\, d\frac{\mathbf{v}}{v}. \quad (2.57)$$

This integral can be evaluated with the aid of Eqs. (2.39), and we find that

$$\mathbf{f} = \frac{\sigma_T \mathbf{q}}{c}\left[1 + \frac{2}{3}\left(\frac{v}{c}\right)^2 \gamma^2\right] = \frac{\sigma_T \mathbf{q}}{c}\left[1 + \frac{2}{3}(\gamma^2 - 1)\right], \quad (2.58)$$

where $\mathbf{q}$ again denotes the radiant energy flux.

For thermal plasma with $kT_e \ll mc^2$,

$$\mathbf{f} = \frac{\sigma_T \mathbf{q}}{c}\left(1 + 2\frac{kT_e}{mc^2}\right), \quad (2.59)$$

since $\overline{v^2} = 3kT_e/m$. In the ultrarelativistic case, when $\gamma \gg 1$,

$$\mathbf{f} = \frac{\sigma_T \mathbf{q}}{c}\left[1 + 8\left(\frac{kT_e}{mc^2}\right)^2\right], \quad (2.60)$$

because the mean

$$\overline{\gamma^2} \approx \frac{\int_1^\infty \gamma^4 e^{-\gamma mc^2/kT_e} d\gamma}{\int_1^\infty \gamma^2 e^{-\gamma mc^2/kT_e}\, d\gamma} \approx 12\left(\frac{kT_e}{mc^2}\right)^2. \quad (2.61)$$

After our calculations had been performed and the analytic expressions given above had been derived, we learned that O'Dell (1981) had also

obtained Eq. (2.58); he describes the sharp drop of the Eddington limit in an ultrarelativistic electron plasma.

2.3.5 Discussion The radiation force in ultrarelativistic electron plasma will be enormously strengthened (and the critical Eddington luminosity will correspondingly diminish) because electrons meeting the photon beam will preferentially scatter the photons by an angle θ of order π, greatly raising the frequency of the photons and giving them a large momentum. That is how most of the electron energy losses will be incurred.

Many processes exist, both collisional and plasma processes, that can rapidly restore the isotropy of the electron distribution. What we need to know is how quickly the plasma will be heated up. If electrons with a particular energy spectrum are being injected, they may lose their energy [see Eq. (2.30)] before the radiation pressure is able to sweep them out of the injection zone. Another important question to be faced concerns the ratio of the number of electrons and protons in the radio-emitting clouds observed in radio galaxies and quasars and whether cool, nonrelativistic matter is present in those clouds.

The principal astrophysical application within our purview will be to the plasma in x-ray and γ-ray sources. Such sources as NGC 4151, in which $kT_e > mc^2$ and $\overline{h\nu} > mc^2$, will also have a greatly diminished value for the critical luminosity, a circumstance that naturally has to be recognized when constructing detailed models for the sources. When disk-type accretion is taking place the radiation-pressure force will control the thickness of the disk, so it is indispensable to have accurate knowledge of that force. On the other hand, the problems of Compton cooling of the plasma are not very significant for disk accretion, because the accretion process is quasisteady.

2.3.6 Radiation Force in Thermal Plasma From Eqs. (2.55) and (2.59) we see that when $h\nu \ll mc^2$ and $kT_e \ll mc^2$ the radiation-pressure force

$$\mathbf{f} = \frac{\sigma_T}{c} \int \left(1 + 2\frac{kT_e}{mc^2} - \frac{16}{5}\frac{h\nu}{mc^2}\right) I_\nu(\mathbf{\Omega}, \nu)\mathbf{\Omega}\, d\mathbf{\Omega}\, d\nu. \quad (2.62)$$

For a blackbody radiation spectrum with $T_e = T_r$ we find

$$\mathbf{f} = \frac{\sigma_T \mathbf{q}}{c}\left(1 - 10.26\frac{kT_r}{mc^2}\right), \quad (2.63)$$

while for a Wien spectrum with $T_e = T_r$,

$$\mathbf{f} = \frac{\sigma_T \mathbf{q}}{c}\left(1 - 10.8\,\frac{kT_r}{mc^2}\right). \tag{2.64}$$

For the bremsstrahlung spectrum $I_\nu = A\exp(-h\nu/kT_e)$ of an optically thin plasma layer we will have

$$\mathbf{f} = \frac{\sigma_T \mathbf{q}}{c}\left(1 - \frac{6}{5}\,\frac{kT_e}{mc^2}\right). \tag{2.65}$$

Some other sample spectra are discussed in Secs. 4.1 and 4.3 below.

2.3.7 Radiation Force upon Accreting Plasma Stream Suppose that plasma is streaming at velocity v toward an x-ray source of luminosity L. Assuming in Eq. (2.57) that the radiation flux is directed along a vector $\boldsymbol{\Omega}$ opposite to the electron velocity vector $\mathbf{v}$, we integrate over $\mu' = -\cos\alpha$ to obtain the familiar expression [see, for example, Landau and Lifshits (1976)]

$$\mathbf{f} = \frac{\sigma_T \mathbf{q}}{c}\,\frac{1 + v/c}{1 - v/c}, \tag{2.66}$$

which holds for all velocities v. In deriving Eq. (2.66) we have assumed low-frequency radiation and have neglected the thermal dispersion of the electron velocities.

2.3.8 Electron–Positron Plasma Compared with the case of electron–proton pairs, for electron–positron pairs the radiation force will be twice as great, while the attractive force toward the gravitating center will be smaller by a factor $2m/m_p$. Hence the critical luminosity for electron–positron pairs will be $m_p/m = 1846$ times lower than the original Eddington value (2.48). If $L > (m/m_p)L_{cr}$, the positrons (along with the electrons, so as to conserve electrical neutrality) should be swept out of accretion disks and other high-temperature zones. It therefore appears unlikely that a steady electron–positron plasma could develop (Bisnovatyĭ-Kogan *et al.* 1971).

One of the authors has examined the acceleration and focusing of electron–positron beams by the radiation of accretion disks (Syunyaev 1983). The highest energies that the particles could attain correspond to $\gamma \approx 5$–

6, even if the disk has a near-critical luminosity. If the particles were more energetic than this value, then in their rest frame the radiation would be directed opposite to them and would brake their motion. In the same paper the deceleration of fast particles by the radiation of an accretion disk is calculated.

2.4 *Competing Physical Processes*

2.4.1 Free–Free Absorption and Emission The mean free path of a photon against inverse bremsstrahlung (free–free absorption) in hydrogen plasma is expressed by the relation

$$\frac{1}{\bar{\lambda}_{\mathrm{ff}}} = \frac{16\pi^2}{3}\left(\frac{2\pi}{3}\right)^{1/2}\frac{r_e^5}{\alpha^2}\left(\frac{mc^2}{kT_e}\right)^{7/2}\frac{g(x)}{x^3}(1 - e^{-x})N_e^2, \qquad (2.67)$$

where $x \equiv h\nu/kT_e$, $\alpha \equiv 2\pi e^2/hc \approx 1/137$ is the fine-structure constant, and $g(x)$ is the Gaunt factor. Comparing $\bar{\lambda}_{\mathrm{ff}}$ with the photon mean free path for Thomson scattering, $\lambda_{\mathrm{T}}^{-1} = \sigma_{\mathrm{T}}N_e = (8/3)\pi r_e^2 N_e$, we see that

$$\frac{\lambda_{\mathrm{T}}}{\bar{\lambda}_{\mathrm{ff}}} = 2\pi\left(\frac{2\pi}{3}\right)^{1/2}\frac{r_e^3 N_e}{\alpha^2}\left(\frac{mc^2}{kT_e}\right)^{7/2}\frac{g(x)}{x^3}(1 - e^{-x}), \qquad (2.68)$$

and if the plasma is so rarefied that

$$N_e \ll 2.62 \times 10^{32}\left(\frac{kT_e}{mc^2}\right)^{7/2}\frac{x^3}{g(x)}(1 - e^{-x})^{-1}\ \mathrm{cm}^{-3} \qquad (2.69)$$

the free–free absorption of photons with $h\nu = xkT_e$ may be neglected compared with the scattering.

In this review our interest centers on the energy exchange between plasma and radiation, and the formation of spectra. As an example let us consider the Comptonization of low-frequency radiation. Take a plasma of density and temperature N_e, T_e and low-frequency radiation of energy density $\mathcal{E}_r$, with $\overline{h\nu} \ll kT_e$. According to Eq. (2.28) the plasma will lose energy to Comptonization at a rate

$$\frac{d\mathcal{E}_r}{dt} = 4c\sigma_{\mathrm{T}}\mathcal{E}_r N_e\frac{kT_e}{mc^2}. \qquad (2.70)$$

On the other hand, the bremsstrahlung loss rate is given by

$$\frac{d\mathcal{E}_T}{dt} = \left(\frac{8}{3\pi}\right)^{1/2} \alpha\sigma_T N_e^2 mc^3 \left(\frac{kT_e}{mc^2}\right)^{1/2}. \tag{2.71}$$

Clearly if

$$N_e < \frac{(6\pi)^{1/2}}{\alpha} \frac{\mathcal{E}_T}{mc^2} \left(\frac{kT_e}{mc^2}\right)^{1/2} \tag{2.72}$$

the Comptonization energy losses will surpass the bremsstrahlung losses: they will predominate in rarefied, high-temperature plasma.

2.4.2 Electron–Positron Pair Production by Photons When $h\nu \gg mc^2$, the cross section for pair production by a photon on a proton is expressed (Akhiezer and Berestetskiĭ 1969) by

$$\sigma_{e^+e^-} = \frac{28}{9} \alpha r_e^2 \left(\ln \frac{h\nu}{mc^2} - 1.9\right). \tag{2.73}$$

Comparing with the Klein–Nishina cross section (2.12), we see that

$$\frac{\sigma_{e^+e^-}}{\sigma_{KN}} = 3.6 \times 10^{-3}\, a \frac{\ln a - 1.9}{\ln a + 0.5}, \tag{2.74}$$

where $a \equiv h\nu/mc^2$; hence photoproduction of pairs on protons (and on electrons, as is easily shown) may be neglected so long as $h\nu < 20$ MeV (the two cross sections will be about the same if $a \approx 435$). We would point out that if the relativistic plasma has a small optical depth with respect to Thomson scattering ($\tau \ll 1$), the presence of the even weaker processes of pair photoproduction on nuclei and electrons will not significantly affect the spectrum of the hard ($h\nu \gg mc^2$) radiation formed through Comptonization—the multiple scattering of photons by relativistic electrons (see Sec. 4.2).

If the energetic photons have a high number density $N_\gamma \gg 1/\sigma_T R$, where R is the radius of the plasma cloud within which the Comptonization is taking place, then the process of electron–positron pair production by two photons will become important. Let the photons have momenta $(h\nu_1/c)\mathbf{\Omega}_1$,

$(h\nu_2/c)\mathbf{\Omega}_2$; then the cross section for pair production $\gamma_1 + \gamma_2 \rightarrow e^+ + e^-$ by the two photons will be (Akhiezer and Berestetskiĭ 1969)

$$\sigma_{\gamma\gamma} = \frac{3}{8}\frac{\sigma_T}{y^2}\left[\left(2 + \frac{2}{y^2} - \frac{1}{y^4}\right)\ln\left(y + \sqrt{y^2 - 1}\right) - \left(1 + \frac{1}{y^2}\right)\left(1 - \frac{1}{y^2}\right)^{1/2}\right], \quad (2.75)$$

where $y^2 = \frac{1}{2}h\nu_1 h\nu_2 (mc^2)^{-2}(1 - \cos\kappa)$, with $\cos\kappa = \mathbf{\Omega}_1 \cdot \mathbf{\Omega}_2$. This process is inverse to that of two-photon pair annihilation. Figure 9 shows the

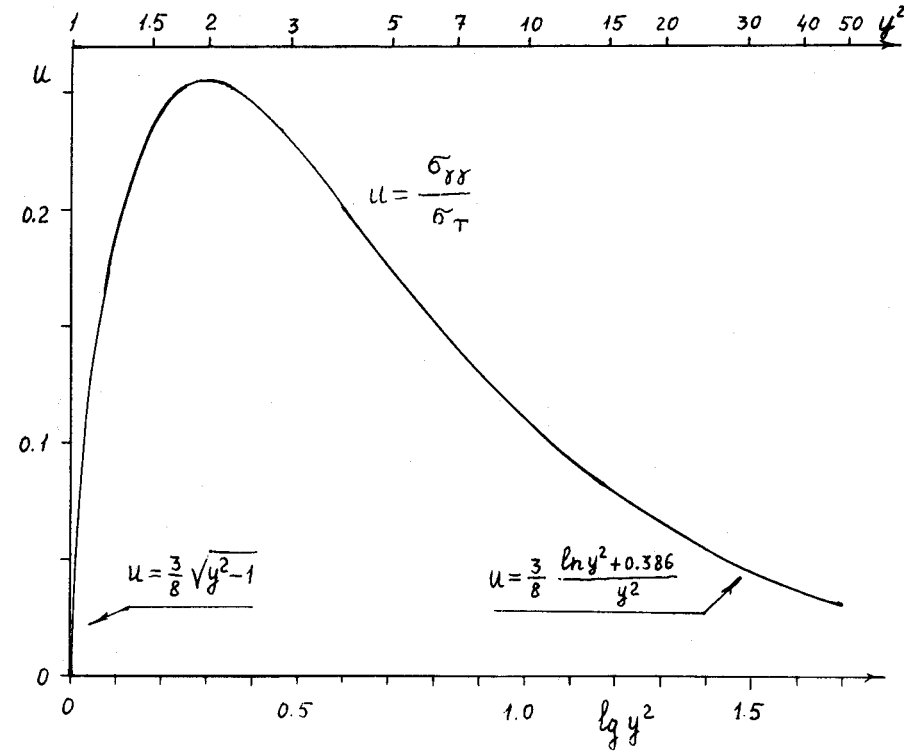

Figure 9 Cross section for the production of electron–positron pairs by two photons [Eq. (2.75)] as a function of the parameter $y^2 = \frac{1}{2}(h\nu_1/mc^2)(h\nu_2/mc^2)(1 - \mathbf{\Omega}_1 \cdot \mathbf{\Omega}_2)$. Asymptotic expressions are given for the limiting cases $y^2 \rightarrow 1$ and $y^2 \gg 1$.

dependence of the normalized cross section (2.75) upon the parameter y^2. The pair production process has a threshold, with $\sigma_{\gamma\gamma} = 0$ for all $y^2 \leqslant 1$. At $y^2 = 2$ the cross section reaches its peak value $\sigma_{\gamma\gamma} = 0.256\sigma_T$.

The mean free path of a photon of momentum $(h\nu_1/c)\mathbf{\Omega}_1$ against the process of two-photon pair production depends on the photon density:

$$\frac{1}{\lambda_{\gamma\gamma}} = \frac{1}{c}\int (1 - \cos\kappa)\sigma_{\gamma\gamma}(y)\frac{I_{\nu_2}(\nu_2, \mathbf{\Omega}_2)}{h\nu_2}\, d\mathbf{\Omega}_2 d\nu_2. \qquad (2.76)$$

If $h\nu_1 \gg mc^2$, photons can be absorbed by interaction with the abundant soft photons having $h\nu \ll mc^2$.

The process of single-photon pair production will become important in the presence of a strong magnetic field. Significant roles will be played by the processes of production, absorption, and scattering of photons at the electron gyrofrequency and its harmonics.

3 Evolution of Line Profiles through Comptonization

X-ray lines of iron have been detected in the spectra of the sources Hercules X-1 (Pravdo *et al.* 1977) and Cygnus X-3 (Kestenbaum *et al.* 1977) as well as several rich clusters of galaxies (Mitchell *et al.* 1976, Serlemitsos *et al.* 1977), heightening interest in the line formation mechanisms in hot plasma and in the processes responsible for shaping the line profiles. In many of the widely accepted models of x-ray sources, radiation is considered to emerge from a region having a substantial optical depth with respect to Thomson scattering. We shall discuss in this section the manner in which iron x-ray–line profiles should evolve due to the frequency shift of photons when they are scattered by electrons.

3.1 Fundamental Processes

3.1.1 Emission of Hot Plasma in Iron X-Ray Lines At the plasma temperatures $kT_e \approx$ 1–100 keV prevailing in compact x-ray sources and in the intergalactic gas in clusters of galaxies, iron will be strongly ionized. Hydrogen- and heliumlike iron ions, comprising a nucleus of charge $Z = 26$ and one or two electrons, respectively, will be abundantly represented.

Ionization by electron collision and photoionization will keep pace with radiative and dielectronic recombination, resulting in ionization equilibrium. The radiative recombination and electron collisions will serve to populate excited levels and produce emission in permitted, forbidden, and intercombination lines (those involving transitions whereby the spin of the ion changes). In dense plasma, however, the forbidden-line emission may be severely suppressed by electron collision, enhancing the transitions of excited ions to states corresponding to intercombination or permitted emission of resonance photons.

In the hydrogenlike iron ion Fe XXVI the $2p \rightarrow 1s$ transition corresponds to the permitted Lyman-α line. The photons in this iron line have an energy $h\nu = 6.97$ keV. The $2s$ level on the contrary undergoes mainly two-photon decay and does not yield a narrow line. The heliumlike Fe XXV ion gives a permitted line with a photon energy $h\nu = 6.70$ keV (the $2\ ^1P_1 \rightarrow 1\ ^1S_0$ transition, analogous to the λ584 Å line in the neutral helium atom), intercombination lines at 6.67 and 6.68 keV (the spin-reversal transitions $2\ ^3P_1 \rightarrow 1\ ^1S_0$ and $2\ ^3P_2 \rightarrow 1\ ^1S_0$, respectively), and the 6.64-keV forbidden line (the $2\ ^3S_1 \rightarrow 1\ ^1S_0$ transition).

In the dielectronic recombination [see, for example, Burgess (1965); Beĭgman *et al.* (1968)]

$$A_Z(\gamma_0) + e^- \rightleftharpoons A_{Z-1}(\gamma, nl) \begin{cases} \searrow A_{Z-1}(\gamma_0, nl) + h\nu \\ \searrow A_{Z-1}(\gamma_0') + \sum h\nu \end{cases}$$

of an ion having the charge Z and the ground state γ_0, excitation of one of the electrons takes place by electron impact (giving the state γ), together with nonradiative recombination of a free electron in the excited state nl. The resulting ion A_{Z-1}, with charge $Z - 1$, will thus have two excited electrons whose combined energy is positive. It will be in an autoionization state and can decay back to the A_Z ion in its ground state together with the free electron. But a radiative transition can also take place, with the emission of a photon and a transition of the A_{Z-1} ion to a bound state $A_{Z-1}(\gamma_0, nl)$ with a single excited electron. That is the dielectronic-recombination process.

The photon which is emitted will have an energy nearly equal to that of the photon emitted in the resonance transition $A_Z(\gamma) \rightarrow A_Z(\gamma_0)$ in an ion

of charge Z rather than $Z - 1$; its energy will differ only because an extra electron is present in the excited state.† Such transitions will cause the permitted lines to be accompanied by satellites. It is worth emphasizing that when a hydrogenlike ion undergoes dielectronic recombination into a heliumlike ion, satellites will develop next to the "Ly-α" line of the hydrogenlike ion, but when a heliumlike ion recombines into a lithiumlike ion, it is the permitted line of the heliumlike ion that will have satellites.

Decay of the bound excited states $A_{Z-1}(\gamma_0, nl)$ may produce additional x-ray lines, not only permitted but also intercombination or forbidden.

In the coronal approximation, the plasma density is so low that one may neglect both collisions that would deactivate the metastable levels and the destruction of resonance photons through photoabsorption by lower-energy ions or Thomson scattering (since the lines will not have a very large depth with respect to resonance scattering; see below). Many authors have invoked the coronal approximation to calculate the intensity of lines emitted by hot astrophysical plasma with the same composition as the solar atmosphere [see, for example, Cox and Tucker (1969), Tucker and Koren (1971), Beĭgman (1974), and Bahcall and Sarazin (1978)]. Syunyaev and Vaĭnshteĭn have evaluated the equivalent width and intensity of hydrogen- and heliumlike iron lines as functions of electron temperature; the results are plotted in Figure 10.

3.1.2 Iron Kα Line Photoionization of the electrons in the lower (K) shell of neutral iron atoms (or weakly ionized ions) by hard ($h\nu > 7.1$ keV) x rays will, with 0.34 probability, be accompanied by emission of a $K\alpha$ photon. The probability of the Auger effect (in which the refilling of the inner, K shell is accompanied by the escape of an electron from an outer shell) is 0.66. The iron $K\alpha$ line comprises a narrow doublet of energy $h\nu = 6.4$ keV; its components are separated by $h\,\Delta\nu = 13$ eV, and each has a natural width of ≈ 3 eV.

3.1.3 Line Profiles The profile of an x-ray line is determined in the coronal approximation by its natural width and by the Doppler broadening associated with the thermal and turbulent velocities of the ions or atoms. For the hydrogenlike Fe XXVI ion the Ly-α line has a radiative width

†The situation resembles the emission of a K_α line by a neutral atom: the energy of the K_α photon similarly differs from the energy of the permitted transition in the corresponding heliumlike ion.

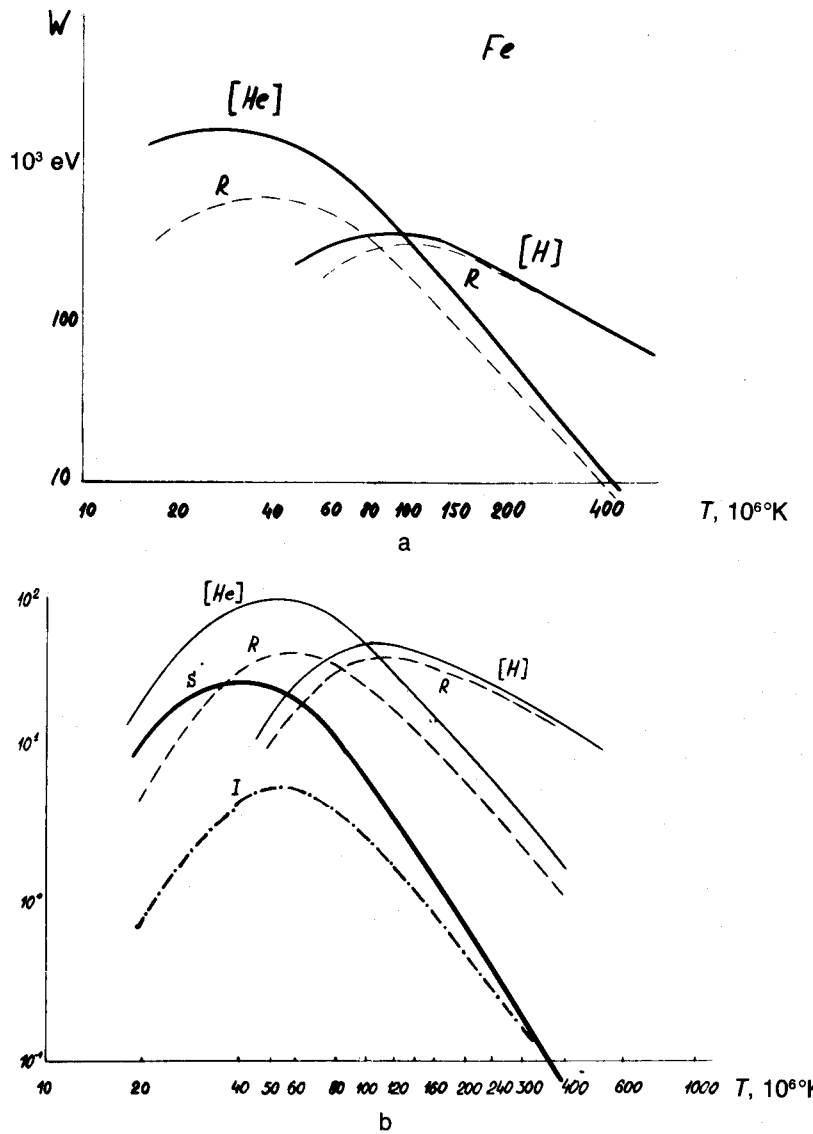

Figure 10 *a*) Equivalent width of x-ray lines of hydrogenlike [H] and heliumlike [He] iron ions as a function of electron temperature. These values have been calculated in the coronal approximation by R. A. Syunyaev and L. A. Vaĭnshteĭn, assuming a normal cosmic abundance of the elements. The dashed curves *R* indicate the contribution of the resonance lines only. *b*) Plasma emissivity in x-ray lines of H- and He-like iron ions as a function of temperature. Curve *S* includes the contribution of the satellites of the He-like ion's resonance lines; curve *I* reflects the contribution of the intercombination lines. Values are expressed in units of $j = 10^{-26}$ erg cm^{-3} sec^{-1}.

$\gamma \approx \gamma_H Z^4 = 1.2$ eV, while its Doppler width

$$h\,\Delta\nu_D = h\nu_0 \left(\frac{2kT_e}{Am_Hc^2}\right)^{1/2} = 4.3 \left(\frac{kT_e}{10\text{ keV}}\right)^{1/2} \text{eV}. \tag{3.1}$$

The ratio of the natural line width to the Doppler width may be expressed by the parameter

$$D = \frac{\gamma}{4\pi h\,\Delta\nu_2} = 0.022 \left(\frac{10\text{ keV}}{kT_e}\right)^{1/2}; \tag{3.2}$$

thus in the temperature range of interest the Doppler width will exceed the natural width. Under the conditions at hand collisional line broadening may practically always be neglected.

The natural line width is much smaller for forbidden and intercombination transitions than for permitted lines, and the probability of resonance scattering is correspondingly low. The probability of absorption by ions of the resonance-line satellites will be almost zero, as such absorption would require a substantial density of excited ions.

All these lines, then, will have near-Doppler profiles whose width is determined by the velocities of thermal and turbulent motion. A further Doppler broadening or shift will result from the velocity dispersion among different line-emission regions that is found in binary star systems (the plasma in the magnetosphere and in the inner zone of the accretion disk will be rotating rapidly, and the normal component as well as the whole system will also be rotating):

$$h\,\Delta\nu = \left(\frac{v}{c}\right) h\nu_c = 23 \left(\frac{v}{1000\text{ km/s}}\right) \text{eV}.$$

But the greatest amount of broadening and distortion of the spectrum will come from scattering by free electrons. When hot electrons scatter radiation the line profile will be Doppler-broadened and on the average will shift toward higher frequencies. The Doppler broadening due to electron scattering is more efficient by a factor $\sqrt{M_i/m}$ ($= 320$ for iron) than that due to resonance scattering (M_i denotes the mass of the nucleus). In

high-temperature gas the first scattering by an electron will produce a Doppler width

$$\Delta\nu/\nu \approx \left(\frac{2kT_e}{mc^2}\right)^{1/2} \approx 0.0626 \left(\frac{kT_e}{1\ \mathrm{keV}}\right)^{1/2},$$

sufficient to remove the resonance lines from resonance. The photons will suffer a large change in frequency even if they are scattered by cool ($kT_e \ll h\nu_0$) electrons: the recoil effect will, on the average, diminish the photon energy by $h\,\Delta\nu \approx (h\nu_0)^2/mc^2 \approx 95$ eV.

3.2 *Emergence of Resonance Lines from Source*

Lyman-α–type resonance lines of the hydrogenlike iron ion Fe XXVI and the heliumlike ion Fe XXV will be intensively emitted by optically thin gas of normal chemical composition over the wide temperature range 1–100 keV. These are the temperatures typical of the plasma in many compact x-ray sources and of the intergalactic gas in galaxy clusters. Angel (1969), Loh and Garmire (1971), Felten *et al.* (1972), and the authors (Pozdnyakov *et al.* 1979*a*) have shown that scattering of radiation by the thermal electrons in the sources will greatly broaden the lines, making them practically unobservable if the source has a large optical depth with respect to scattering.

The optical depth τ_l with respect to resonance scattering in the line also proves to be significant here. Usually it much exceeds the optical depth for Thomson scattering: $\tau_l \gg \tau$ (Felten *et al.* 1972, Vaĭnshteĭn and Syunyaev 1982). The customary expression for the scattering cross section in a resonance line with a Doppler absorption profile is

$$\sigma_l = \frac{e^2\sqrt{\pi}}{mc} f \frac{1}{\Delta\nu_D} \exp\left[-\left(\frac{\Delta\nu}{\Delta\nu_D}\right)^2\right], \tag{3.3}$$

where the oscillator strength $f = 0.416$ for the Ly-α line in hydrogenlike ions; the Doppler width $\Delta\nu_D$ is given by Eq. (3.1). At the center of the Ly-α iron line $\sigma_l = 6 \times 10^{-18}\ [(10\ \mathrm{keV})/kT_e]^{1/2}\ \mathrm{cm}^2$. Even if one accepts an iron abundance [Fe]/[H] $= 3 \times 10^{-5}$, the mean free photon path at the line center will be much shorter {by a factor (σ_l/σ_T)[Fe]/[H] $\approx 2.7 \times 10^2\ [(10\ \mathrm{keV})/kT_e]^{1/2}$} than the mean free path $\lambda_T = (\sigma_T N_e)^{-1}$ against Thomson scattering. Under these circumstances the following process will be likely: excitations of, say, the $2p$ level of the hydrogenlike iron ion by electron

impact will, along with recombinations, produce photons in the Ly-α line. These photons will repeatedly be resonantly scattered by the iron ions (since $\tau_1 \gg \tau$), broadening the line: $\Delta\nu \propto \sqrt{\ln t}$, where t is the time scale for Brownian wander of the photons. Then after a photon has traversed a path ct of the same order as the mean free path λ_T for Thomson scattering, it will be scattered by an electron. Its frequency will change markedly, and it will escape from resonance.

Let us consider now the problem of the emergence of resonance-line photons from a plasma cloud. We shall assume that the source of the resonance photons is located at the center of a spherical cloud and that the surrounding plasma merely scatters the radiation. Although the solution of this problem is well established [see, for example, Ivanov's book (1969)], one can arrive at a simple result by following the approach which R. A. Syunyaev and L. G. Titarchuk have taken.

Calculations by the Monte Carlo method have shown (Osterbrock 1962) that in a situation of this kind a photon will be scattered again and again, diffusing slowly in space, until it reaches the far wing of the line and freely escapes from the plasma cloud. We shall wholly neglect the spatial diffusion of photons, however, regarding them as being multiply scattered at the center of the cloud. For simplicity we further assume that as photons are absorbed and reemitted they undergo a complete frequency redistribution within the Doppler line profile $\alpha(x) = \exp(-x^2)$ [$x \equiv (\nu - \nu_0)/\Delta\nu_D$, ν_0 is the frequency of a photon at the line center, $\Delta\nu_D = \nu_0(2kT_i/M_ic^2)^{1/2}$].

At the line center the cloud will have an optical depth τ_0 against resonance scattering. In view of the complete frequency redistribution a photon of frequency x will have a probability $p_1 = \exp[-\alpha(x)\tau_0]$ of escaping from the cloud without having been scattered even once. This probability will be of order unity only in the far wings of the lines, at frequencies such that $\alpha(x)\tau_0 \lesssim 1$, that is, $|x| \geqslant \sqrt{\ln \tau_0}$. With complete frequency redistribution the probability that a photon will have a frequency x after being scattered is $p_2 = \pi^{-1/2}\alpha(x) = \pi^{-1/2} \exp(-x^2)$. The probability that a scattered photon will escape from the source is therefore

$$P = \int_{-\infty}^{\infty} p_1(x)p_2(x)dx = \frac{2}{\sqrt{\pi}} \int_0^{\infty} \exp\left(-x^2 - \tau_0 e^{-x^2}\right) dx. \quad (3.4)$$

For large τ_0 the integral (3.4) can readily be evaluated (say by the method

of steepest descent), and one finds

$$P \approx \frac{1}{\sqrt{\pi}\tau_0 \sqrt{\ln \tau_0}}. \tag{3.5}$$

On the average a photon will experience

$$N_{sc} = P^{-1} = \sqrt{\pi}\tau_0 \sqrt{\ln \tau_0} \tag{3.6}$$

scatterings in the cloud. This expression agrees with the exact result. For comparison, if photons diffuse through a plasma cloud in which Thomson scattering is the predominant mechanism and if the cloud has a central photon source, then the average number of scatterings experienced by a photon will be $\frac{1}{2}\tau_T^2$ [see, for example, Syunyaev and Titarchuk (1980)], far more than in the diffusion of a resonance line.

The spectrum of the emergent radiation will evidently be described by the function

$$\psi(x) = p_1(x)p_2(x) = \frac{1}{\sqrt{\pi}} \exp\left(-x^2 - \tau_0 e^{-x^2}\right), \tag{3.7}$$

which reaches a maximum for $|x| = \sqrt{\ln \tau_0}$ (Figure 11).

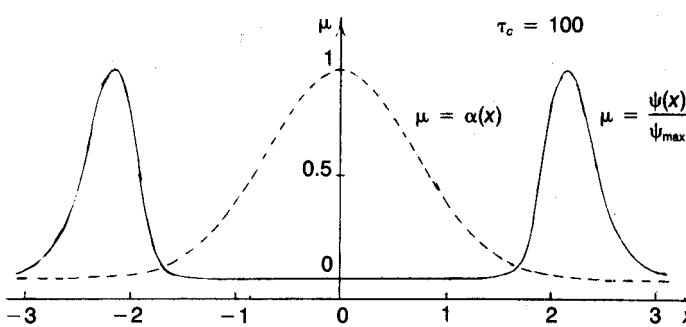

Figure 11 The spectrum of a resonance line emerging from a scattering plasma cloud which has a central photon source. This spectrum has been calculated for an optical depth $\tau_0 = 10^2$ at the line center. For comparison the dashed curve shows the Doppler profile $\alpha(x)$. The curves are normalized to their peak values.

Let λ denote the probability that a photon will survive a single scattering and assume that $1 - \lambda \ll 1$; then one can easily determine the photon destruction probability in the plasma cloud. For if a photon has undergone N_{sc} scatterings [Eq. (3.6)], then the relation $N_{sc}(\tau_{th})(1 - \lambda) = 1$ will yield the cloud thickness τ_{th} such that the photons will "perish" almost totally as they pass through the cloud:

$$\tau_{th} = \frac{1}{(1 - \lambda)\sqrt{-\ln(1 - \lambda)}} \tag{3.8}$$

(this approximate solution can be obtained iteratively from the condition above, provided that $1 - \lambda \ll 1$ and $\tau_{th} \gg 1$).

Here is a simple example. In the resonance absorption of the Ly-β line of a hydrogenlike atom, the Ly-β line will be emitted with 0.87 probability, and two photons, Ly-α and Hα, with 0.13 probability. According to Eq. (3.8), if $\tau_0 > 5.4$ at the line center the Ly-β photons will not be able to escape from the plasma cloud. Such a line is actually observed in the spectrum of the Perseus cluster of galaxies (Pravdo and Mushotzky 1980). We therefore can obtain a further useful bound on the number of hydrogenlike iron ions in the cluster:

$$N_{\text{Fe XXVI}} R < 5 \times 10^{18} \left[\left(\frac{kT_e}{10 \text{ keV}} \right)^{1/2} + \frac{\langle V_{\text{turb}} \rangle}{200 \text{ km/s}} \right] \text{cm}^{-2}$$

($\langle V_{\text{turb}} \rangle$ denotes the rms turbulent velocity), since the transition in question has an oscillator strength $f_{1-3} = 0.079$.

If a photon should be scattered by an electron in between two resonance scatterings, it will leave the line profile and perish (it can no longer be regarded as a photon in the line). Let $\beta = \sigma_c/\sigma_0$ be the ratio of the continuum absorption cross section (in our case $\sigma_c = \sigma_T$) to the scattering cross section at the center of the line. If the survival probability $\lambda = 1$ and the ratio $\beta \neq 0$, the photon will be destroyed along its trajectory. A photon of frequency x will be created with probability $p_1 = \pi^{-1/2}\alpha(x)$, while the probability of destruction en route to the next resonance absorption is $p_3 = \beta/[\beta + \alpha(x)]$. Hence the probability that a photon will be destroyed after a single resonance scattering event is given by

$$P_d = \int_{-\infty}^{\infty} p_1 p_3 dx = \frac{2\beta}{\sqrt{\pi}} \int_0^{\infty} \frac{e^{-x^2}}{\beta + e^{-x^2}} dx \approx \frac{2}{\sqrt{\pi}} \beta \sqrt{\ln \frac{1}{\beta}}, \tag{3.9}$$

provided $\beta \ll 1$. Photons will perish in the plasma cloud if the product $N_{sc}P_d$ of the number of scatterings by the destruction probability is of order unity:

$$2\beta\sqrt{\ln\frac{1}{\beta}}\,\tau_0\sqrt{\ln\tau_0} \sim 1. \tag{3.10}$$

Solving this relation iteratively, we find that

$$\tau_{th} = \frac{1}{-2\beta\ln\beta} \tag{3.11}$$

If the cloud thickness τ_0 exceeds the "thermalization length" τ_{th}, resonance photons will perish in the cloud. The condition for the photons to perish can be written more simply: substituting specific values of β into Eq. (3.11), we see that photons will perish if

$$\tau > \frac{1}{2\ln(\tau_l/\tau)}. \tag{3.12}$$

Compton scattering that removes a line from resonance may be regarded as a form of "continuum absorption," the term generally used in the theory of resonance-line transfer. The simple derivation we have given does not work nearly as well if photon sources are distributed throughout the cloud, but it can readily be modified to the case of a Lorentz line profile. The problem is examined in detail in Ivanov's book (1969). In any event the thermalization length will be described by an expression similar to Eq. (3.11). It is natural to distinguish three cases [compare the condition (3.12)]:

a. $\tau < [2\ln(\tau_l/\tau)]^{-1}$. The plasma may be considered optically thin with respect to electron scattering, even for resonance photons. The line will be broadened only by the Doppler effect from resonance ion scattering; it will remain comparatively narrow (a few tens of electron volts wide at most).

b. $[2\ln(\tau_l/\tau)]^{-1} \approx 0.05\text{–}0.2 < \tau < 1$. Almost all photons will experience one and only one scattering by an electron.

c. $\tau > 1$. Photons will experience multiple scatterings by electrons within the source.

In cases *b* and *c*, photons that do not undergo electron scattering will

be able to escape only from a narrow zone in the outer part of the source where $2\tau \ln(\tau_l/\tau) < 1$. We would also point out that the resonance-scattering cross section is far smaller for intercombination and forbidden iron lines than for the permitted line. A situation can arise in which intercombination and forbidden radiation emerges from the source without having been scattered by electrons, so that the lines are narrow, whereas the permitted line is greatly broadened by electron scattering. That can happen only if the plasma density is so low that collisions do not appreciably weaken those lines.

3.3 Emission Zones for Iron X-Ray Lines

Analytic estimates for the problem outlined above have been obtained in an interesting study by Felten *et al.* (1972), and Monte Carlo calculations for one or two cases have been published by Angel (1969), Loh and Garmire (1971), and Pozdnyakov *et al.* (1979*a*).

We opened this section by mentioning some astronomical objects from which iron x-ray emission has been detected: clusters of galaxies and x-ray sources in binary star systems. In the case of the galaxy clusters, straightforward estimates indicate that electron scattering can have little effect on the intensity of the resonance lines.

McCray and Lamb (1976) as well as Basko and Syunyaev (1976) have suggested that the soft x rays being emitted by Her X-1 (Shulman *et al.* 1975, Beĭgman *et al.* 1976) may come from a plasma cloud which is moving along the neutron-star magnetosphere, absorbing and reprocessing the hard x rays that emanate from the central source. Syunyaev (1976) has remarked that the reprocessing ought to give rise to a number of emission lines, and not only resonance lines [see also Bai (1980)]. In fact, in an x-ray binary system the resonance emission may be accompanied by the $K\alpha$ lines of weakly ionized iron ions. The surface of the normal star will be impacted by a substantial x-ray flux, and the spectrum of the reflected radiation should contain strong lines of various heavy elements (particularly the $K\alpha$ lines) along with distinctive K-jumps (Basko *et al.* 1974). According to an analysis by Shakura and Syunyaev (1973) [see also Lyutyĭ and Syunyaev (1976)], much of the x radiation will be intercepted by the outer zones of the accretion disk, resulting in characteristic line emission, whereas resonance lines will develop in the hot corona vaporized above the disk and the normal component [see Basko (1978) for further details].

Hatchett *et al.* (1976) have calculated the intensity of the x-ray lines

that will form in a homogenous, spherically symmetric plasma cloud surrounding an x-ray source. Emission in the $K\alpha$ lines of weakly ionized iron is typical for this case as well.

Contrary to the situation with the Ly-α resonance lines, the photons of a $K\alpha$ iron line and resonance-line satellites will not be subjected to resonance scattering but will be scattered only by electrons (both free ones and those bound in hydrogen atoms). The recoil energy $h\,\Delta\nu \approx h^2\nu^2/mc^2 \approx$ 80 eV acquired by a scattering electron will exceed the binding energy of the electron in a hydrogen atom, so the scattering process will be accompanied by ionization. Thus only calculations for case *c* (Sec. 3.1), in which the source has a large optical depth for scattering [$\tau = \sigma_T(N_e + N_H)R > 1$], will be applicable to $K\alpha$ photons.

We see, then, that in an x-ray binary system characteristic emission lines and absorption jumps may be produced by weakly ionized heavy elements (on the surface of the normal star, in the outer parts of the accretion disk, in cool stellar wind, in the magnetospheric plasma), while resonance x-ray lines and recombination emission jumps at energies close to the ionization potentials of the corresponding ions may occur (in the plasma near the neutron-star surface, where most of the energy is released, or in the magnetosphere, as well as in the induced stellar wind, in the corona above the disk, and so on). In all these places the plasma in the emission zone will have a substantial Thomson optical depth, as the emission-line spectrum should demonstrate.

3.4 Single Scattering

This is the process represented by case *b* at the end of Sec. 3.2. We first give the results of an analytic treatment, and then describe some Monte Carlo calculations.

3.4.1 Line Profile: Analytic Expression for Case $kT_e = 0$ In the limiting case $kT_e = 0$, the line profile subsequent to a single-scattering event will be determined entirely by the recoil effect, and one can easily obtain an analytic formula. A photon having $h\nu_0 \ll mc^2$ will be scattered by the angle θ with the probability $P(\theta)\,d\cos\theta = \frac{3}{8}(1 + \cos^2\theta)\,d\cos\theta$. Afterward its energy will be [see Eq. (2.5)]

$$h\nu = h\nu_0\left[1 - \frac{h\nu_0}{mc^2}(1 - \cos\theta)\right],$$

so that

$$\cos\theta = 1 - \frac{mc^2}{h\nu_0}\frac{\nu_0 - \nu}{\nu_0}, \qquad d\cos\theta = \frac{mc^2}{h\nu_0^2}\,d\nu.$$

Transforming from $P(\theta)\,d\cos\theta$ to $P(\nu)d\nu$, we find that in the frequency range $\nu_0(1 - 2h\nu_0/mc^2) \leqslant \nu \leqslant \nu_0$ the line profile will be expressed (Pozdnyakov *et al.* 1979*a*) by

$$P(\nu)d\nu = \frac{3}{8}\frac{mc^2}{h\nu_0^2}\left[1 + \left(\frac{mc^2}{h\nu_0^2}\right)^2(\nu - \nu_1)^2\right]d\nu, \tag{3.13}$$

where $\nu_1 = \nu_0(1 - h\nu_0/mc^2)$ is the average frequency of a scattered photon. After scattering the line profile will clearly be symmetric about ν_1, the point of minimum intensity. Profiles calculated numerically for $kT_e = 0$ (see Figure 1) agree closely with the expression (3.13).

3.4.2 Analytic Results for Case $h\nu_0 \ll kT_e$ In this limiting case the line will be broadened by the Doppler effect in the scattering process. Babuel-Peyrissac and Rouvillois (1969) and Zel'dovich *et al.* (1972) have derived the nonrelativistic kernel of the kinetic integral equation

$$\frac{dI_\nu(\nu)}{dt} = -I_\nu(\nu)\int P(\nu \to \nu')d\nu' + \int I_\nu(\nu')\frac{\nu}{\nu'}P(\nu' \to \nu)d\nu', \tag{3.14}$$

describing how the spectrum changes when the photons are scattered by Maxwellian electrons:

$$P(\nu' \to \nu) = 2\pi\int_{-1}^{1}\mathcal{K}(\nu' \to \nu, \mu)d\mu. \tag{3.15}$$

The quantity

$$\mathcal{K}(\nu' \to \nu, \mu) = \frac{3}{16\pi}\left(\frac{mc^2}{2\pi kT_e}\right)^{1/2}\frac{\nu(1 + \mu^2)}{\nu' g} \times \exp\left[-\frac{mc^2}{2kT_e g^2}\left(\nu - \nu' - \frac{hg^2}{mc^2}\right)^2\right]; \tag{3.16}$$

μ is the cosine of the scattering angle, $g^2 = \nu^2 + \nu'^2 - 2\mu\nu\nu'$, and ν, ν' respectively denote the photon frequency before and after scattering.

When in the general case one integrates the kernel over the scattering angle, one does not obtain a simple, convenient analytic expression. But the result does simplify considerably if one neglects the role of the recoil effect—that is, if in the exponent in Eq. (3.16) the term hg^2/mc^2 may be assumed small compared with $\nu - \nu'$. This approximation is valid in the limit of low-frequency ($h\nu' \ll kT_e$) spectral lines. Syunyaev (1980) has determined the following expression for such a profile:

$$P(u) = \frac{1}{160}\left(\frac{mc^2}{2\pi kT_e}\right)^{1/2}\frac{(1+u)^5}{u^3}\left\{\left[3 - Q^2(u) - 10\frac{1+u^2}{(1+u)^2} + 15B(u)\right]\exp\left(-\frac{Q^2(u)}{2}\right) - 15B(u)Q(u)\Phi[Q(u)]\right\}, \quad (3.17)$$

in which $P(u)du \equiv P(\nu' \to \nu)d\nu'$ [Eq. (3.15)] with $u \equiv \nu/\nu'$,

$$Q^2(u) = \frac{mc^2}{kT_e}\left(\frac{1-u}{1+u}\right)^2, \quad (3.18)$$

$$B(u) = \frac{u^4 + 6u^2 + 1}{(u+1)^4} + \frac{2}{3}Q^2(u)\frac{u^2+1}{(u+1)^2} + \frac{1}{15}Q^4(u), \quad (3.19)$$

and

$$\Phi(z) = \int_{|z|}^{\infty}\exp\left(-\frac{z^2}{2}\right)dz$$

is the probability integral. It is easily seen that

$$P(\nu \to \nu') = (\nu'/\nu)^2 P(\nu' \to \nu) = P(u)u^{-2}. \quad (3.20)$$

If we substitute $I_\nu(\nu') = A\delta(\nu' - \nu_0)$ into the kinetic equation (3.14), we find that after a single scattering by Maxwellian electrons with $kT_e \gg h\nu_0$

the photons of a monochromatic line, averaged over all angles of departure, will have a spectrum of the form

$$I_\nu(\nu) = \frac{u^2 P(u)}{\nu_0}. \tag{3.21}$$

This spectrum has a cusp at $\nu = \nu_0$, that is, at $u = 1$ (Zel'dovich *et al.* 1972), and bears no resemblance to the customary Doppler (Gaussian) spectrum $I_\nu = \pi^{-1/2} \exp[-(u^2 - 1)mc^2/2kT_e]$.

The expression $u^2P(u)$ can readily be expanded in series with respect to the quantity $x = (\nu/\nu_0) - 1$ near the maximum of the function:

$$u^2P(u) = 1 + \frac{3}{2}x - \kappa|x| + x^2\left(\frac{35}{88n} - \frac{17}{22}\right) - \kappa x|x| + \ldots, \tag{3.22}$$

where

$$\kappa = \frac{15}{22}\sqrt{\frac{\pi}{2n}}, \qquad n = \frac{kT_e}{mc^2}.$$

In its right-hand branch ($x > 0$),

$$u^2P(u) = 1 + \left(\frac{3}{2} - \kappa\right)x + \left(\frac{35}{88n} - \frac{17}{22} - \kappa\right)x^2 + \ldots,$$

so that on the right the spectral index $\alpha^+ = -(d \ln I_\nu / d \ln x)_{x=+0} = \kappa - \frac{3}{2}$. In the left-hand branch

$$u^2P(u) = 1 + \left(\frac{3}{2} + \kappa\right)x + \left(\frac{35}{88n} - \frac{17}{22} + \kappa\right)x^2 + \ldots,$$

so that $\alpha^- = (d \ln I_\nu / d \ln x)_{x=-0} = \kappa + \frac{3}{2}$. Accordingly $\alpha^- - \alpha^+ = 3$.

3.4.3 Numerical Calculations; Comparison with Analytic Expressions Figure 12 compares the analytic spectrum (3.21) for a monochromatic line after a single scattering by Maxwellian electrons with

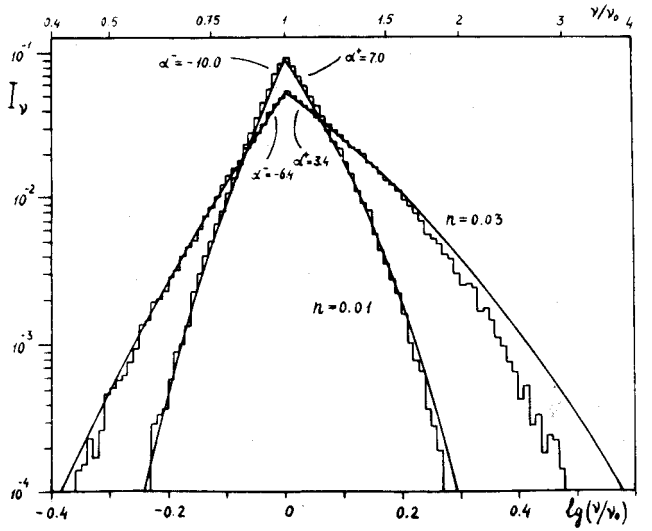

Figure 12 Profiles calculated by the Monte Carlo method for a monochromatic line with $h\nu_0 \ll kT_e$ whose photons have experienced single scattering by Maxwellian electrons for which $kT_e = 0.01mc^2$ and $0.03mc^2$. *Smooth curves*, profiles given by the analytic expression (3.21).

$kT_e \gg h\nu_0$ against calculations by the Monte Carlo method. A spectrum emitted at a given angle to the original direction of the radiation beam will have a Gaussian profile and be described by the kernel (3.16), but the spectra shown in this diagram have been integrated over the scattering angle; that is, they correspond to an isotropic angular distribution of the radiation prior to scattering. The curves are normalized to equal numbers of photons. In both cases, $kT_e = 5.11$ keV and $kT_e = 15.33$ keV, the Monte Carlo calculations give an excellent fit to the analytic formula, the deviation becoming significant only when $\nu/\nu_0 > 1.8$ or $\nu/\nu_0 < 0.4$. The spectral indices to the right and left of the cusp differ by 3, as the analytic formula requires. Thus Eq. (3.21) very adequately describes the pedestal of the line profile, formed by photons that have been scattered only once in the source. On the other hand, for $n = 0.01$ the comparison represents a further test of the calculation technique, and the good agreement with the analytic expression indicates that the results are likely to be correct.

In the Introduction (Figure 1) we have shown profiles of an iron $K\alpha$ x-ray line after a single scattering by electrons that have a Maxwellian

spectrum for various temperatures. These curves demonstrate how the relative roles of the recoil and Doppler effects change as the electron temperature and the ratio $kT_e/h\nu_0$ increase.

For comparison with the analytic expression (3.13), Figure 1 also displays a profile calculated for a temperature $kT_e = 1$ eV $\approx 10^4$ °K. Even when the temperature is this low, the presence of thermal electron velocities clearly will have a decisive effect on the line profile: it will become asymmetric, and its low-frequency wing will be much spread out while the high-frequency side remains practically unaltered. The reason is that when a photon undergoes forward scattering ($1 - \cos\theta \ll 1$) its frequency will experience only a small Doppler shift $\Delta\nu = \Delta\nu_D\sqrt{1 - \cos\theta}$. Note that the calculation for $kT_e = 1$ eV satisfies the formal condition that the influence of the Doppler effect upon the line profile be small: $v/c = (2kT_e/mc^2)^{1/2} \ll h\nu_0/mc^2$, that is, $kT_e \ll (h\nu_0)^2/2mc^2 = 40[h\nu_0/(6.4\text{ keV})]^2$ eV.

Finally, Figure 13 exhibits profiles computed for an iron x-ray line after single scattering by weakly relativistic or relativistic electrons. The curves illustrate the transition from the kernel of the nonrelativistic kinetic equation given above to the standard asymptotic expression for the kernel of the kinetic equation which describes the scattering of low-frequency photons by ultrarelativistic electrons—the inverse Compton effect [see, for example, Ginzburg and Syrovatskiĭ (1964); Blumenthal and Gould (1970)]. If $\gamma = (1 - v^2/c^2)^{-1/2} \gg 1$, if the electrons are monoenergetic and isotropically distributed, and if the Thomson approximation holds, then after they are scattered the photons will have an energy between $h\nu_0/4\gamma^2$ and $4\gamma^2 h\nu_0$, where $h\nu_0$ is the pre-scattering energy [these values follow from Eq. (2.6) for $\mu = 1$, $\mu' = -1$ and $\mu = -1$, $\mu' = 1$, respectively]. Maximum intensity will, however, be reached at energies $h\nu \gg h\nu_0$.

3.5 *The Kompaneets Equation and its Properties*

A Fokker–Planck expansion of the kinetic equation (3.14) with the kernel (3.16) and with induced-scattering terms yields the kinetic differential equation of Kompaneets (1956):

$$\frac{\partial n}{\partial t} = \frac{\sigma_T N_e}{mc}\frac{1}{\nu^2}\frac{\partial}{\partial \nu}\nu^4\left(n + n^2 + \frac{kT_e}{h}\frac{\partial n}{\partial \nu}\right), \tag{3.23}$$

describing the Compton interaction between isotropic radiation having a photon occupation number $n = \mathcal{E}_\nu c^3/8\pi h\nu^3$ in phase space and Maxwellian

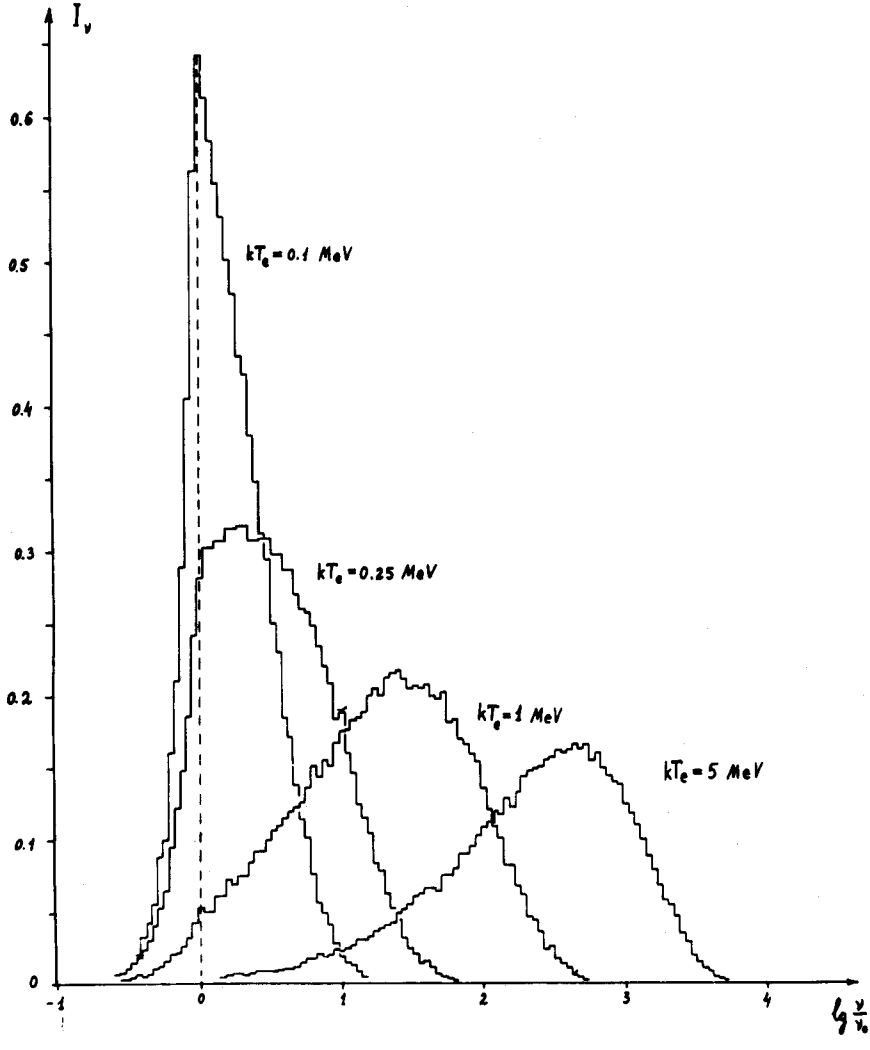

Figure 13 Profiles of the 6.4-keV iron line after single scattering by Maxwellian electrons (weakly relativistic and relativistic plasma).

electrons having $kT_e \ll mc^2$. The derivation of the kernel (3.16) assumes that $h\nu \ll mc^2$. From the differential equation (3.23) one can determine the spectra that will result from multiple scattering (here and below $\mathcal{E}_\nu$ denotes the spectral energy density of the radiation).

It is convenient to introduce a dimensionless frequency $x = h\nu/kT_e$ and time $y = \int [kT_e(t)/mc^2]\sigma_T N_e c\, dt$. The Kompaneets equation then becomes

$$\frac{\partial n}{\partial y} = \frac{1}{x^2}\frac{\partial}{\partial x} x^4 \left(n + n^2 + \frac{\partial n}{\partial x} \right). \tag{3.24}$$

The last parenthesized term on the right describes the diffusion of photons along the frequency axis and the cooling which the electrons undergo as they repeatedly scatter the photons and change their frequencies by the Doppler effect. The first term in parentheses describes the downward motion of the photons along the frequency axis and the heating of the electrons by recoil; the second term allows for induced effects, and it too is associated with the action of recoil and the electron heating [see the discussions by Syunyaev (1971) and Levich and Syunyaev (1971)]. In Compton scattering the number of photons is conserved, and indeed the Kompaneets equation implies that

$$\frac{d}{dt} N_\gamma = \frac{d}{dt} \int n\nu^2 d\nu = 0. \tag{3.25}$$

In plasma of specified temperature the processes accompanying the production and absorption of photons (such as free–free processes) will leave the frequency distribution function of the photons unaltered only if the radiation has a Planck spectrum $n = (e^x - 1)^{-1}$ corresponding to $T_r = T_e$. But Compton scattering will no longer affect the frequency distribution for any spectrum of the form $n = (e^{x+\mu} - 1)^{-1}$ with $\mu > 0$, that is, in the more general case of a Bose–Einstein equilibrium distribution, as one can easily see by substituting the B–E spectrum into the right-hand member of the Kompaneets equation. The chemical potential μ measures the deficiency in the number of B–E photons compared with a blackbody photon frequency distribution at the same temperature. In the limit $\mu \gg 1$ the B–E distribution reduces to the special case of a Wien spectrum $n = e^{-(x+\mu)}$, or $\mathcal{E}_\nu = 8\pi e^{-\mu}(h\nu^3/c^3) \exp(-h\nu/kT_e)$, a law which clearly

satisfies the Kompaneets equation without the n^2 term responsible for induced processes. In the Wien distribution the mean photon energy

$$\overline{h\nu} = kT_e \frac{\int_0^\infty x^3 e^{-x} dx}{\int_0^\infty x^2 e^{-x} dx} = 3kT_e. \tag{3.26}$$

We shall often find in this review that, for a given photon number, Compton scatterings will tend to establish a Wien spectrum with $\overline{h\nu} = 3kT_e$.

Following Levich and Syunyaev (1971), let us multiply the Kompaneets equation by $8\pi h\nu^3/c^3$ and integrate it with respect to frequency. On integrating by parts from zero to infinity we obtain the equation

$$\frac{d\mathcal{E}_r}{dt} = 4\frac{kT_e}{mc^2}\sigma_T N_e c\mathcal{E}_r - \frac{\sigma_T N_e h}{mc}\int_0^\infty \nu\mathcal{E}_\nu d\nu - \frac{\sigma_T N_e c^2}{8\pi m}\int_0^\infty \frac{\mathcal{E}_\nu^2}{\nu^2} d\nu. \tag{3.27}$$

Since $d\mathcal{E}_r/dt = -\frac{3}{2} N_e d(kT_e)/dt$, the first term on the right evidently describes the cooling, and the other two terms the heating, of the electrons. If $\mathcal{E}_\nu = A\delta(\nu - \nu_0)$ we arrive at the result obtained in Sec. 2.2.4: every time a photon is scattered its energy will change, on the average, by $\Delta\nu/\nu = (4kT_e - h\nu)/mc^2$. Setting $d\mathcal{E}_r/dt = 0$ in Eq. (3.27), we obtain an expression, derived in a different way by Peyraud (1968) and Zel'dovich and Levich (1970), for the stationary electron temperature in a radiation field with a given spectrum:

$$kT_e = \frac{1}{4\mathcal{E}_r}\left(\int_0^\infty h\nu\mathcal{E}_\nu d\nu + \frac{c^3}{8\pi}\int_0^\infty \frac{\mathcal{E}_\nu^2}{\nu^2} d\nu\right). \tag{3.28}$$

3.6 Analytic Results for Homogeneous Problem

The modification of spectral lines due to electron scattering can easily be illustrated by taking the homogeneous problem. Consider an unbounded homogeneous medium filled with electrons at some temperature T_e. Let us represent the initial line profile by a δ-function and see how it will evolve with time. Problems of this kind are of interest for cosmology.

3.6.1 Doppler Broadening If in the Kompaneets equation (3.24) we neglect the first two terms in parentheses, then it will describe only the

Doppler frequency shift caused by the scattering. In 1969 Zel'dovich and Syunyaev solved the resulting diffusion equation:

$$n(x, y) = \frac{1}{\sqrt{4\pi y}} \int_0^\infty n(z) \exp\left[- \frac{(\ln x + 3y - \ln z)^2}{4y} \right] \frac{dz}{z}, \quad (3.29)$$

which indicates how an arbitrary initial spectrum $n(\nu, 0)$ will have evolved at arbitrary time y, for $\tau = \sigma_T N_e ct \gg 1$.

In the case of an infinitely narrow line profile $\mathcal{E}_\nu(x, t = 0) = A\delta(x - x_0)$, or equivalently $n(x, t = 0) = Bx_0^{-3}\,\delta(x - x_0)$, we will have the solution

$$\mathcal{E}_\nu(x, y) = \frac{A}{\sqrt{4\pi y}\, x_0} \exp\left[- \frac{(\ln x_0 - \ln x + 3y)^2}{4y} \right]. \quad (3.30)$$

The line clearly will broaden with time, its center of gravity meanwhile shifting toward higher frequencies (Pozdnyakov *et al.* 1979*a*). The frequency of peak intensity will increase with y as

$$x_{\max} = x_0 e^{3y}, \quad (3.31)$$

and at the level of half peak intensity the line halfwidth will be given by

$$x_{1/2} = x_0 \exp(3y \pm 2\sqrt{y \ln 2}). \quad (3.32)$$

So long as $y \ll 1$ (and $\tau \gg 1$), Doppler broadening will play the main role:

$$\frac{\Delta x}{x_0} = \pm 2\sqrt{y \ln 2} = \pm 2\sqrt{\ln 2} \left(\tau \frac{kT_e}{mc^2} \right)^{1/2}. \quad (3.33)$$

3.6.2 Recoil Effect If $h\nu > 4kT_e$, the time evolution of the line will be determined not by the Doppler effect but by the recoil that results from electron scattering:

$$\frac{\Delta\nu}{\nu} = -\frac{h\nu}{mc^2}(1 - \cos\alpha), \quad (3.34)$$

where α is the scattering angle. The recoil effect should clearly have a substantial influence on the evolution of the x-ray line spectrum. If in the Kompaneets equation we now neglect the last two parenthesized terms (the induced scattering and the Doppler frequency shift due to the scattering), then the equation will describe how the spectrum should evolve in the homogeneous case because of the scattering recoil effect:

$$\frac{\partial n}{\partial t} = x^{-2} \frac{\partial (x^4 n)}{\partial x}. \tag{3.35}$$

Illarionov and Syunyaev (1972) and Arons (1971) have solved this equation: the quantity $n\nu^4$ will be conserved as motion takes place along the trajectory $d\nu/du = -\nu^2$, where $du = (h/mc)\sigma_T N_e dt$. The trajectory may also be written as $d\lambda/dt = \sigma_T N_e h/m$, or $d\lambda/d\tau = h/mc$. To this approximation the line will evidently remain monochromatic as it evolves, and it can only shift downward along the frequency axis. Actually, however, the amplitude of the recoil effect will depend on the scattering angle ($0 < \Delta\nu/\nu < 2h\nu/mc^2$), so the line should in fact broaden somewhat (Illarionov and Syunyaev 1972, Illarionov *et al.* 1979).

3.7 *Multiple Electron Scattering: Computed Line Profiles*

We turn now to case *c* among those listed at the end of Sec. 3.2. Resonance-line photons are considered to undergo numerous scatterings by electrons within a plasma cloud, and as a result their spectrum will change. Photons will naturally differ in the number of times they are scattered in the cloud; this circumstance as well as the dispersion in the frequency shift when a photon is scattered will give rise to a complicated emission spectrum. Thus far analytic expressions describing these spectra have been obtained only for the two limiting cases $kT_e = 0$ and $kT_e \gg h\nu_0$, with a large Thomson-scattering depth $\tau \gg 1$ (Syunyaev and Titarchuk 1980).

In our calculations a spherical plasma cloud has been assumed, with a uniform electron density and an optical depth $\tau = \sigma_T N_e R$. We have taken the cases $\tau = 1, 2, 3, 5, 10$, and electron temperatures $kT_e = 0, 0.102, 1.02, 10.2$ keV. Initial energies $h\nu_0 = 6.9$ keV and $h\nu_0 = 6.4$ keV (the iron $K\alpha$ line) have been adopted for the photons, whose source is placed

at the center of the cloud. A case has also been considered in which the source is distributed uniformly throughout the cloud. The initial line profile is taken to be a δ-function.

The results of the calculations are here presented in several graphs. Figure 14 illustrates the evolution of the $K\alpha$ line profile when the cloud is cold ($kT_e = 0$); thus the Doppler effect will be vanishingly weak and instead the recoil effect will predominate in altering the photon frequencies. Accordingly the profile is broadened only on the low-frequency side.

When $kT_e = 1.02$ keV the line profile evolves as shown in Figure 15. Both the Doppler and the recoil effect now contribute to the broadening. Figures 14, 15, and 16a clearly demonstrate how the role of the Doppler effect strengthens with rising plasma temperature: the line width increases and the shift toward low frequencies diminishes.

Since there is a finite probability of direct photon escape, a narrow peak develops at frequency ν_0 (see Figure 16b). The photon flux in this narrow line can easily be calculated analytically. The direct-escape probability will evidently be

$$\exp[-\tau(1 - 2h_0/mc^2)] = \exp(-0.975\tau).$$

For a 50-eV spectral resolution the photon flux in the original line (prior to scattering) corresponded to 200 units along the vertical axis; hence direct escape corresponds, for the same resolution, to a flux of $200\exp(-0.975\tau)$, or 75.4, 28.45, 10.73, 1.53, 0.0117 for $\tau = 1, 2, 3, 5, 10$, respectively. The profiles plotted in Figures 14 and 15 take into account only photons that have been scattered in the source, but their total number corresponds to normalization by $200[1 - \exp(-0.975\tau)]$. In Figure 14 ($kT_e = 0$) the intensity corresponding to direct escape is shown separately for $\tau = 3$ and 5; for the other cases it can easily be computed from the expression given above.

Thus a narrow line will emerge from the cloud, a core representing unscattered photons; at the same time there will be a broad pedestal consisting of photons which have experienced Compton scattering in the cloud.

As the energies of the $K\alpha$ photons of neutral iron and the Ly-α photons of hydrogen- and heliumlike iron ions differ by less than 10 percent, the profiles computed for the different lines should naturally be quite similar. Figure 16b illustrates this resemblance. The curves in Figure 16c compare the intensities calculated for lines emerging from the plasma cloud when the photons have a central source and when the source is distributed uni-

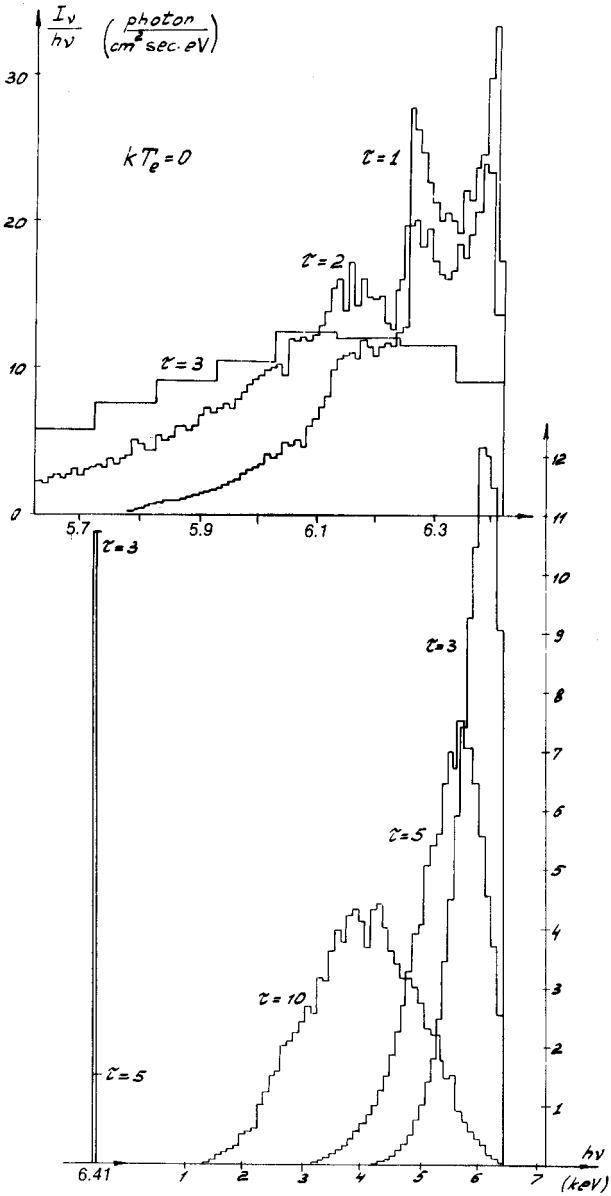

Figure 14 Profiles computed for the iron x-ray line at $h\nu_0 = 6.4$ keV emerging from a plasma cloud of temperature $kT_e = 0$ and various optical depths τ. The photon source is located at the center of the cloud. The flux corresponding to direct photon escape is not represented in the spectra themselves but is plotted separately at the lower left for the cases $\tau = 3$ and $\tau = 5$; these photons have not been scattered, so their frequency remains unchanged.

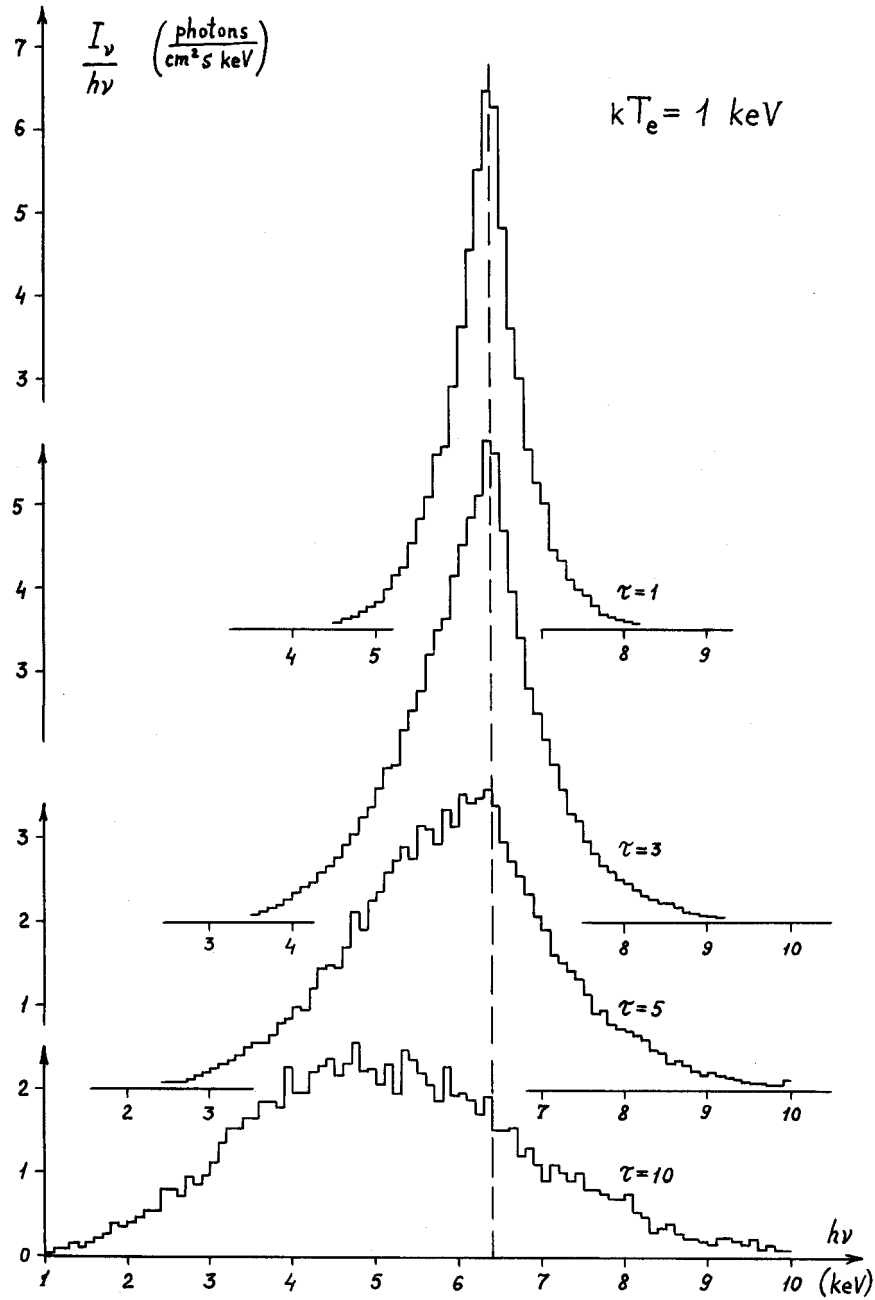

Figure 15 Profiles of the 6.4-keV x-ray line emerging from a spherical cloud having $kT_e = 1$ keV and various optical depths. The spectra do not include direct-escape photons. The photon source is at the center of the cloud.

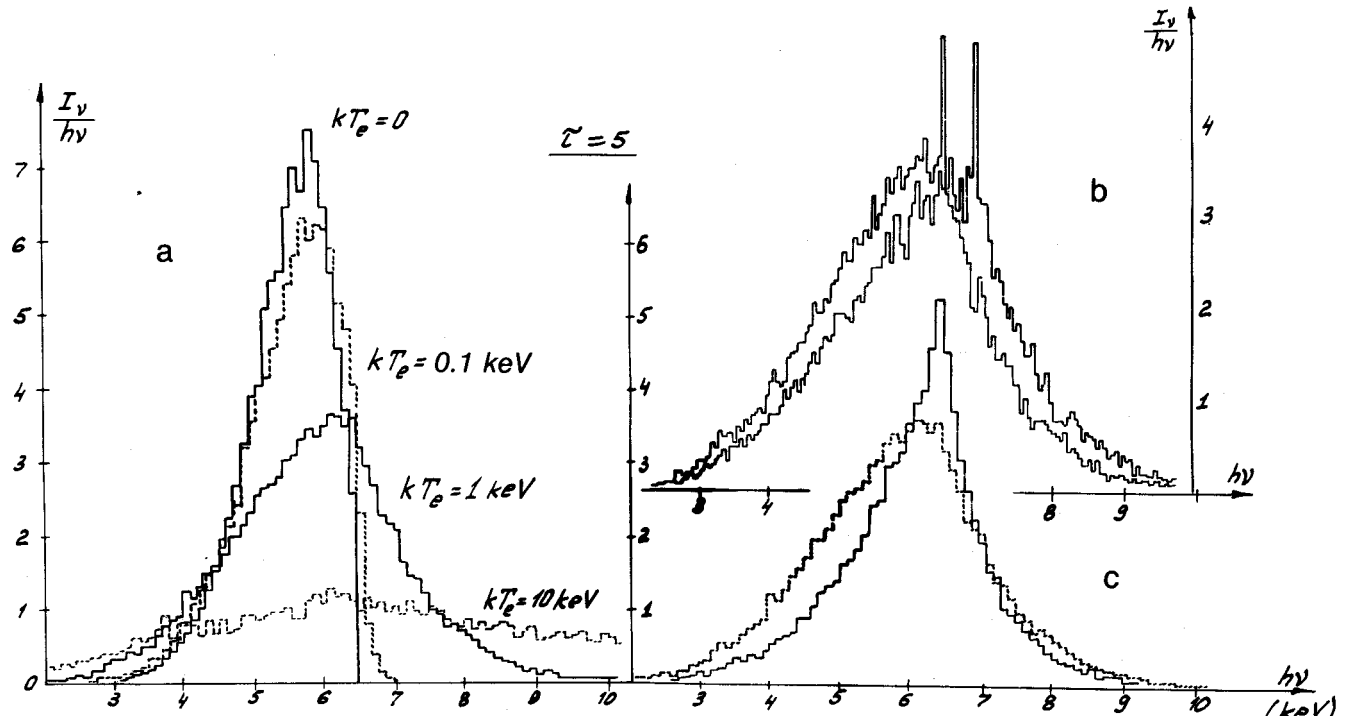

Figure 16 *a*) Plasma temperature dependence of the profile of the 6.4-keV line emerging from a spherical plasma cloud with $\tau = 5$, for a central photon source; *b*) profiles computed for two lines ($h\nu_0 = 6.4$ keV, $h\nu_0 = 6.9$ keV) emerging from a spherical cloud with $kT_e = 1$ keV and $\tau = 5$, for a central photon source; *c*) dependence of the line profile ($kT_e = 1$ keV, $\tau = 5$) on the placement of the photon source (dotted curve, source at center of spherical cloud; solid curve, source distributed uniformly over the cloud). Direct-escape photons are included only in profiles *b*.

formly over the cloud. In the latter case the shift and broadening of the line are substantially smaller: $\Delta_{1/2}\nu/\nu_0 = 0.09$, compared with $\Delta_{1/2}\nu/\nu_0 = 0.19$ for a central source (if $\tau = 5$ and $kT_e = 1$ keV). This behavior reflects the higher escape probability for photons which have been scattered only a few times within the source.

The profiles in Figure 17 represent lines of a hydrogenlike silicon ion, emerging from a plasma cloud with a large Thomson-scattering depth. These results agree closely with the analytic expressions given below in Sec. 4.1. Notice that strong power-law wings of the line are formed even when $\tau = 3$, and when τ is as large as 20 the emergent photons approach a Wien spectrum.

3.8 Continuum Photoabsorption

As pointed out above, not only emission lines but also other features can develop in x-ray spectra. In particular, the characteristic absorption of x rays by weakly ionized iron ions could give rise to a spectrum of the form depicted in Figure 18. The photoabsorption cross section has here been taken as $\sigma_{Fe} = \sigma_0(\nu_c/\nu)^3$ for $\nu \geq \nu_c$, where $h\nu_c = 7.1$ keV for weakly ionized iron; the quantity $\sigma_0 = 3.5 \times 10^{-20}$ cm^2. The ratio of the photo-

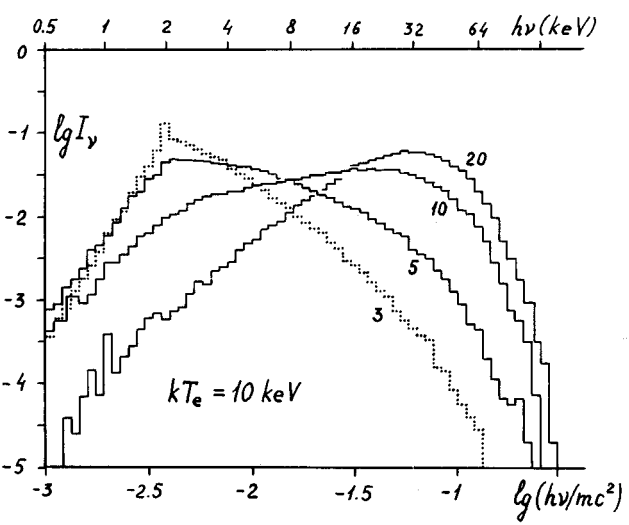

Figure 17 Profiles computed for the hydrogenlike silicon-ion line at $h\nu_0 = 2$ keV emerging from a spherical plasma cloud having $kT_e = 10$ keV and various Thomson-scattering depths τ. The photon source is central.

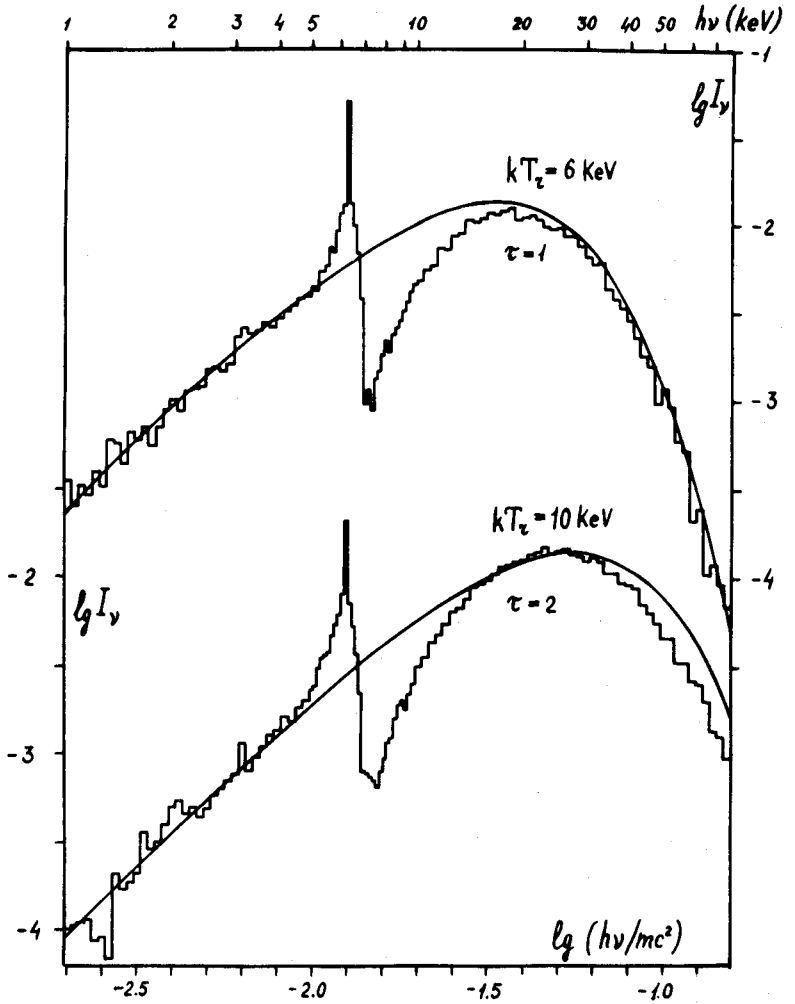

Figure 18 Spectra derived from blackbody radiation passing through a spherical cloud of low-temperature ($kT_e = 0.5$ keV) plasma. The processes included in the calculation are: the characteristic photoabsorption by weakly ionized iron ions, fluorescence in the iron $K\alpha$ line, and Thomson scattering. Central radiation source. Upper spectrum calculated for $\tau_{Fe}/\tau = 2$; lower spectrum, for $\tau_{Fe}/\tau = 0.8$.

absorption depth to the Thomson-scattering depth depends on the iron and hydrogen abundances:

$$\frac{\tau_{Fe}}{\tau} = \frac{\sigma_{Fe}}{\sigma_T} \frac{[Fe]}{[H]} \frac{2}{1 + X}, \tag{3.36}$$

where X denotes the proportion of hydrogen by mass. Our calculations assume that either $\tau_{Fe} = 2\tau$ (upper curve in Figure 18) or $\tau_{Fe} = 0.8\tau$ (lower curve); that is, $[Fe]/[H] = 3.2 \times 10^{-5}$ or 1.3×10^{-5}, with $X = 0.7$. Photoabsorption by elements other than iron has been neglected. Each event of photoabsorption of a hard x-ray photon will, with 0.34 probability, be accompanied by fluorescence emission of a 6.4-keV photon in the iron $K\alpha$ line.

In these calculations the central source is assumed to have a Planck primary spectrum with $kT_r = 6$ or 10 keV. The cloud surrounding the source has $kT_e = 0.001\ mc^2$ and a Thomson-scattering depth $\tau = 1$ or 2 for the two respective cases. Figure 18 shows that the radiation emanating from the cloud will exhibit a strong, broad absorption band for $\nu > \nu_c$ together with a prominent, narrow $K\alpha$ line. When $\tau = 2$, even though a lower iron abundance is assumed ($\tau_{Fe} = 0.8\tau$) the photoabsorption strengthens, since Compton scatterings will further entangle the photon trajectories [see also Ross *et al.* (1978) and Pozdnyakov *et al.* (1979*b*)]. In the neighborhood of the $K\alpha$ line the spectral resolution of the calculations is 0.2 keV.

The spectrum plotted as a solid curve in Figure 19 has been computed by the method discussed above for comparison with observations (Becker *et al.* 1978) of the x-ray pulsar Vela X-1 (4U 0900 − 40). The following parameters have been adopted in the calculation: $[Fe]/[H] = 1.3 \times 10^{-5}$ (corresponding to $\tau_{Fe} = 0.8\tau$), $X = 0.7$, cloud optical depth $\tau = 1$, $kT_e = 0.5$ keV; the spectral resolution is 0.3 keV near the $K\alpha$ line. The central source is assumed to have a Planck spectrum with $kT_r = 10$ keV. The fit to the x-ray measurements is quite satisfactory. Most likely the strong absorption observed at $h\nu < 5$ keV represents photoabsorption by elements lighter than iron (these are neglected in our calculations).

Spectra of the kind shown in Figure 19 might arise when the radiation of an x-ray pulsar interacts with magnetospheric plasma, with stellar-wind plasma, or with the gas streams in the binary system. Such spectra could not, however, result from interaction of the x rays with material in the

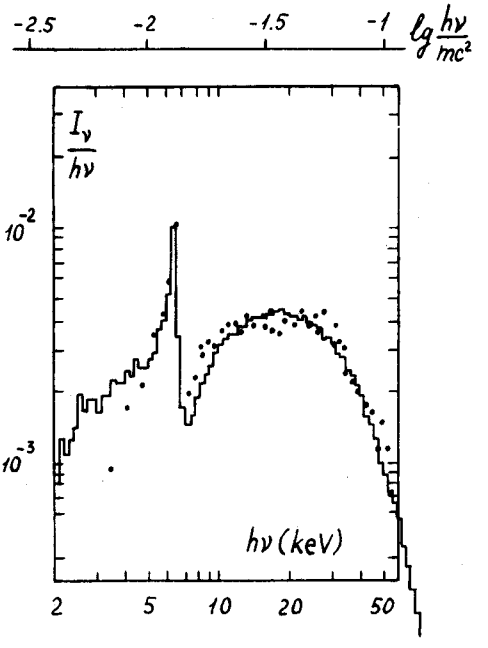

Figure 19 A simulation of the spectrum of the x-ray pulsar Vela X-1. Model geometry as in Figure 18; $\tau = 1$, $\tau_{Fe}/\tau = 0.8$, $kT_r = 10$ keV, $kT_e = 0.5$ keV. Experimental points from Becker *et al.* (1978).

accretion disk or from the x rays being reflected by the atmosphere of the visible star: those effects would be of far smaller amplitude.

4 Comptonization of Low-Frequency Radiation in a Hot Cloud of Nonrelativistic Plasma

4.1 Spatial Problem: Formulation and Analytic Solution

In early attempts to calculate the spectra of x-ray sources, the results of the homogeneous problem, which are pertinent to cosmology, were naively carried over to the situation prevailing in a spatially bounded plasma cloud, where the distribution of photons with respect to the time when they escape from the source plays the dominant role. Different photons will undergo a differing number of collisions there, decisively affecting the radiation

spectrum formed through Comptonization and issuing from the plasma cloud.

The importance of solving the spatially limited problem was recognized simultaneously and independently by Katz (1976), Shapiro *et al.* (1976), and the authors of this review (Pozdnyakov *et al.* 1976). In the first two papers the analysis relied on a solution of the stationary Kompaneets equation (Katz adopted a numerical approach while Shapiro *et al.* solved it analytically for a single value of the parameters), whereas our calculations for a cloud of weakly relativistic plasma were performed by the Monte Carlo method. Naturally identical results were obtained: in the case of a low-frequency ($h\nu \ll kT_e$) photon source the radiation emerging from the cloud was found to have a power-law spectrum at low frequencies ($h\nu < kT_e$) but an exponential cutoff in the range $h\nu > 3kT_e$.

The next step was taken by Syunyaev and Titarchuk (1980), who solved analytically the problem of the Comptonization of low-frequency ($h\nu \ll kT_e$) radiation in an isothermal, nonrelativistic ($kT_e \ll mc^2$) plasma cloud having a substantial optical depth with respect to Thomson scattering ($\tau \gg 1$). In this case the diffusion approximation will correctly describe how the photons are distributed over their escape time, or equivalently, over the number of scatterings u they experience within the source. The average value of u is of order τ^2, and one finds that in a spherical plasma cloud the probability of a photon being scattered many more times than average should fall off as

$$P(u) \propto \exp\left[-\frac{u\pi^2}{3(\tau + \frac{2}{3})^2}\right], \tag{4.1}$$

almost independently of the manner in which the photon sources are distributed over the plasma cloud or of the cloud geometry† (see Figure 2 in the Introduction). For such a probability distribution $P(u)$, and with the photon frequencies being shifted mainly by the Doppler effect, a power-law spectrum should be observed.

The behavior here is rather similar to the familiar Fermi statistical acceleration mechanism, which gives rise to a power-law spectrum for the same reason (Eardley 1976). From the curves presented in Figure 20 one can see how a unified power-law spectrum will develop from the ensemble

†It is interesting to find that the law of photon escape from a plasma cloud closely describes the time evolution of the radiation of x-ray bursters during their flare events (Grindlay and Gursky 1976, Canizares 1976, Syunyaev and Titarchuk 1980).

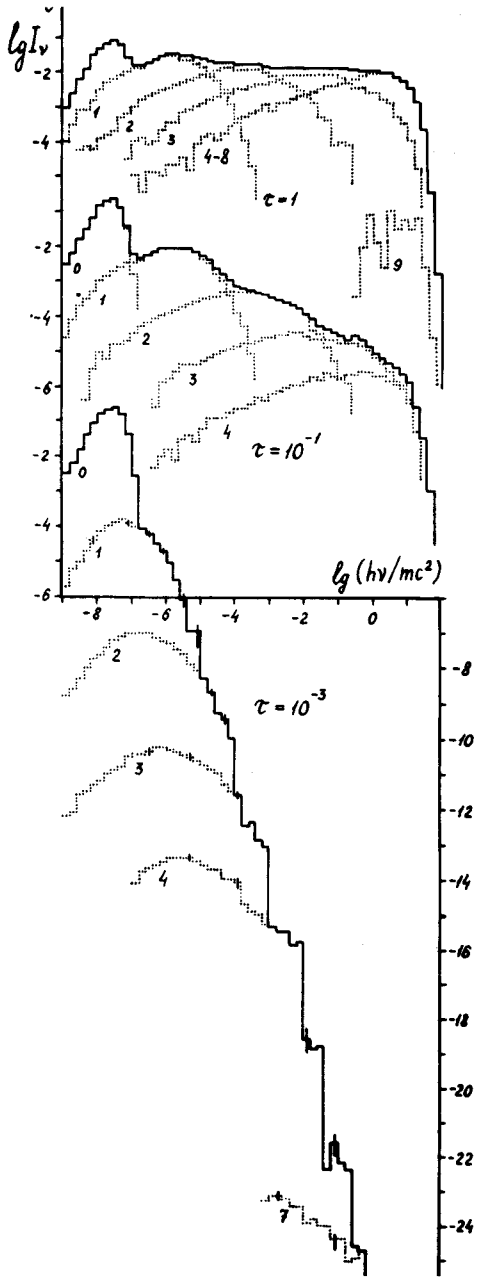

Figure 20 Comptonization of low-frequency radiation in a cloud of weakly relativistic plasma for three values of the optical depth τ. *Dashed curves* represent the contributions of the separate scattering events. The successive scatterings by Maxwellian electrons combine to form a power-law spectrum for the hard radiation.

of spectra produced by photons scattered a differing number of times in the plasma cloud. Notice that as the optical depth of the cloud increases, multiple scatterings become more probable and the radiation spectrum flattens out.

Syunyaev and Titarchuk (1980) have solved the stationary Kompaneets equation

$$\frac{1}{x^2}\frac{d}{dx}\,x^4\left(\frac{dN}{dx}+N\right)=\gamma N-\frac{\gamma f(x)}{x^3}, \tag{4.2}$$

where the quantity on the left represents the differential Kompaneets operator (Sec. 3.4), including both the Doppler diffusion of the photons along the frequency axis (first parenthesized term) and their downward motion along that axis due to the recoil effect (second term). The role of induced processes is neglected. On the right-hand side the first term describes the diffusion of photons out of the source; the second allows for the presence of photon sources with a spectrum $f(x)$ in the cloud. The quantity $N = I_\nu c^2/2h\nu^3$ is the occupation number in photon phase space, $x = h\nu/kT_e$ is a dimensionless frequency, and

$$\gamma=\frac{\pi^2}{3}\frac{mc^2}{(\tau+\frac{2}{3})^2kT_e} \tag{4.3}$$

if the geometry is spherical (a cloud of radial optical depth τ), while

$$\gamma=\frac{\pi^2}{12}\frac{mc^2}{(\tau_0+\frac{2}{3})^2kT_e} \tag{4.4}$$

in the case of a disk (Figure 6a).

Equation (4.2) reduces to Whittaker's equation, and if $\nu \gg \nu_0$ ($h\nu_0 \ll kT_e$ is the characteristic energy of the radiation from the low-frequency photon source) it yields the following solution for the flux:

$$F_\nu(x)=Ax^{-\alpha}e^{-x}\int_0^\infty t^{\alpha-1}e^{-t}(x+t)^{\alpha+3}dt$$

$$=Ax^3e^{-x}\int_0^\infty t^{\alpha-1}e^{-t}\left(1+\frac{t}{x}\right)^{\alpha+3}dt. \tag{4.5}$$

In both the limits $x \ll 1$ and $x \gg 1$ the integrals in the expression for the spectrum reduce to gamma functions, much simplifying it. For $x \ll 1$ we find the power-law radiation spectrum

$$F_\nu(x) = Bx^{-\alpha}; \tag{4.6}$$

for $x \gg 1$, the Wien spectrum

$$F_\nu(x) = Cx^3 e^{-x}. \tag{4.7}$$

When $x \ll 1$ the spectral index

$$\alpha = -\tfrac{3}{2} + \sqrt{\tfrac{9}{4} + \gamma} \tag{4.8}$$

depends only on the electron temperature and optical depth of the plasma cloud, not on its internal distribution of photon sources. That is quite natural, because after having been scattered $u \approx \tau_0^2$ times the photons will completely forget where they were born. A hard radiation spectrum, on the other hand, will produce photons that undergo far more scatterings than the average value $\bar{u} \approx \tau_0^2$.

The solution (4.5) describes the spectrum at all frequencies. Its significance was recognized once this comparatively simple expression proved to fit perfectly the spectrum of the source Cygnus X-1 (Figure 4), the renowned black hole candidate [see, for example, Eardley *et al.* (1978)]. High-altitude balloon measurements obtained by the Max-Planck-Institut für Extraterrestrische Physik have been compared against the values given by Eqs. (4.5) and (4.8) (Syunyaev and Trümper 1979); the results indicate that the Cyg X-1 accretion disk has an electron temperature $kT_e = 26.5$ keV and a scattering optical depth $\tau_0 = 2$. For spherical geometry, by Eq. (4.3), $\tau = 5$. These observations furthermore imply that the part of the accretion disk responsible for the x rays ought to be fairly homogeneous and isothermal.

Remarkably enough, a detailed analysis of the structure of accretion disks on the basis of standard disk-accretion theory (Shakura and Syunyaev 1976) unexpectedly disclosed that the inner disk zone should contain just such a region, with a scattering optical depth τ_0 across the disk and an energy release Q^+ per unit surface area that are practically independent of

the distance from the black hole. For a Schwarzschild black hole this zone would extend from 3.2 R_g to 7–8 R_g, and about 30–40% of the energy emitted by the accretion disk would be released there (Syunyaev 1983). At large distances from the black hole τ_0 will grow rapidly and there will be a sharp decline in Q^+ (here $R_g = 2GM/c^2 = 3M/M_\odot$ km is the gravitational radius of the black hole).

4.2 *Relation between Number of Scatterings and Photon Frequency*

According to Eq. (3.31), when low-frequency photons are Comptonized in an unbounded, homogeneous medium filled with hot electrons their frequency will, on the average, increase with time as

$$\nu = \nu_0 \exp\left(3 \frac{kT_e}{mc^2} u\right),$$

where ν_0 is the initial frequency of a photon and $u = \int \sigma_T N_e c \, dt$ represents the number of times it is scattered. Taking logarithms, we see that the photon frequency will shift from ν_0 to ν after an average number of about

$$u = \frac{1}{3} \frac{mc^2}{kT_e} \ln \frac{\nu}{\nu_0}$$

scatterings.

A relationship of the same kind can easily be derived for the spatially limited problem—for a sphere or a disk. Following the approach of Syunyaev and Titarchuk (1980), we represent the spectrum of the radiation escaping from a disk as a convolution:

$$F_\nu(x) = \int_0^\infty I_\nu(x,u) P(u) du,$$

where $P(u)$ specifies how the photons are distributed with respect to the time when they emerged from the plasma cloud, and $I_\nu(x, u)$ describes the emission spectrum that would have developed after time $t = u/\sigma_T N_e c$ through Comptonization of low-frequency photons in an unbounded, homogeneous medium filled with hot electrons. So long as $h\nu_0 \ll h\nu \ll 3kT_e$, the frequency will change solely because of the Doppler effect, and $I_\nu(x, u)$ will be completely determined by Eq. (3.30); one merely needs to

remember that the variable $y = (kT_e/mc^2)u$. By substituting into the integral for $F_\nu(x)$ the solution (3.30) and an eigenfunction $P(u) = Be^{-\beta u}$, and then integrating over u by the method of steepest descent, Syunyaev and Titarchuk found that

$$F_\nu(x) = D(\bar{u}) \left(\frac{x}{x_0}\right)^{-\alpha},$$

where $\alpha = -\frac{3}{2} + \sqrt{\frac{9}{4} + \gamma}$, with $\gamma = (mc^2/kT_e)\beta$. The constants $D(\bar{u})$ and $B(\bar{u})$ both depend upon the distribution of soft-photon sources over the plasma cloud.

In carrying through the integration,

$$F_\nu(x) = AB \int_0^\infty \frac{1}{\sqrt{4\pi y}} \exp\left\{ - \frac{[\ln (x/x_0) + 3y]^2}{4y} - \gamma y \right\} dy$$

$$= \frac{AB}{\sqrt{4\pi}} \int_0^\infty e^{-\varphi(y)} dy,$$

we automatically arrive at a relation between the number of scatterings u and the frequency ν which defines Eq. (3.31). The function $\varphi(y)$ reaches a minimum when

$$\ln^2 \frac{x}{x_0} = 4y^2 \left(\frac{9}{4} + \gamma + \frac{1}{2y}\right).$$

If $y_{\text{eff}} \gg 1$ (the only case in which the photons can drift significantly upward along the frequency axis), we will have the simple expression $y_{\text{eff}} = (9 + 4\gamma)^{-1/2} \ln (x/x_0)$; in other words, in order for $\nu \gg \nu_0$ the number of scatterings should be

$$u_{\text{eff}} = \frac{\ln (\nu/\nu_0)}{\sqrt{9 + 4\gamma}} \frac{mc^2}{kT_e} = \frac{\ln (\nu/\nu_0)}{2\alpha + 3} \frac{mc^2}{kT_e},$$

where α, as before, denotes the spectral index of the x rays observed. This equation was published by Payne in 1980. It will be valid provided $h\nu \ll 3kT_e$, that is, in the zone where the recoil effect may be neglected. Clearly the

photons in the Wien tail of the spectrum formed through Comptonization will have undergone even more scatterings.

In the case of the Cygnus X-1 source, where $\alpha \approx 0.57$, $kT_e = 27$ keV, and $\tau_0 = 2$, the number $\bar{u} \approx 2$–4; a photon will need 20 scatterings to build up from $h\nu_0 \approx 1$ keV to $h\nu \approx 3kT_e \approx 81$ keV. The expression given above is useful for estimating the time scale on which the x-ray emission will vary in different energy ranges.

4.3 Monte Carlo Calculations of the Radiation Spectrum

It is natural to inquire how pertinent Syunyaev and Titarchuk's diffusion approximation is to the state of affairs in the Cyg X-1 disk, where the optical depth is small ($\tau_0 = 2$) and the radiation temperature is comparatively high. To clarify this point, numerical calculations have been performed by the Monte Carlo method for $kT_e = 25$ keV and two geometries: spherical and disk (Figures 21 and 22). In Figure 21 we compare the spectra (solid curves) computed from Eqs. (4.5), (4.8), and (4.3) against the Monte Carlo results for the corresponding τ and the same kT_e. The analytic expression systematically diminishes the intensity for high $h\nu$; in other words, it overestimates the spectral index α. But as the Thomson-scattering optical depth of the disk increases, the departure of the analytic approximation from the Monte Carlo results becomes smaller. This circumstance suggests that the disparity reflects an inaccurate estimate of the parameter γ: Eqs. (4.3) and (4.4) are based on the diffusion (in space) approximation, and when τ is small they would not be expected to describe properly how the number of scatterings in the cloud depends on optical depth. From the Monte Carlo calculations one can determine the spectral index α in the low-frequency region and substitute it into Eq. (4.5) to obtain an analytic fit to the spectrum for all $h\nu$.

Syunyaev and Titarchuk (1983) have developed methods for estimating the parameter γ in the diffusion approximation for intermediate optical depths ($\tau \geqslant 2$), and have also obtained exact values of γ by solving the equation of transfer. The resulting spectral indices α are in good agreement with the Monte Carlo calculations described below.

In the disk case, Figure 22 (computed to higher precision than Figure 21) shows that for small depths ($\tau_0 < 2$) the high-energy tail of the spectrum runs below the analytic approximation. This behavior results from the Klein–Nishina decrease in the scattering cross section and the concomitant lengthening of the photon mean free path at $h\nu \approx 100$ keV by some tens of percent [see Eq. (2.16) and Table I]. The spectrum is here formed by

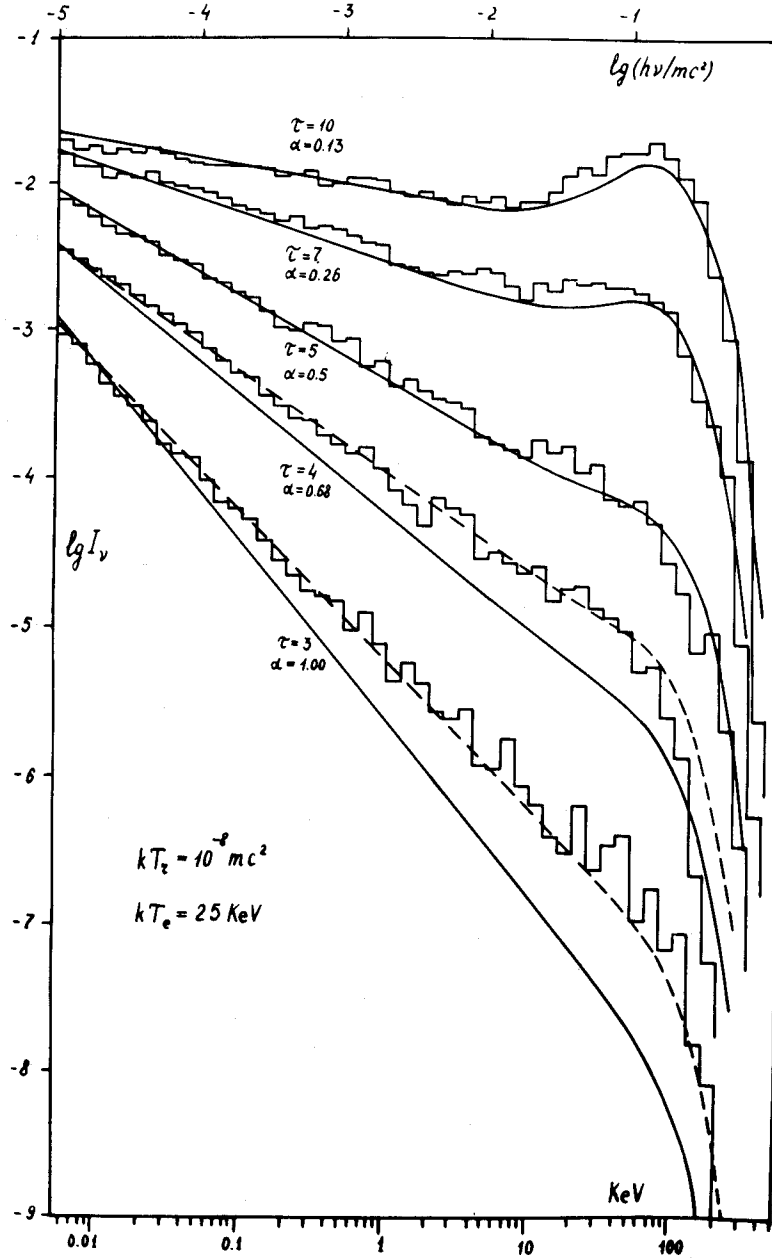

Figure 21 Comptonization of low-frequency photons in a spherical plasma cloud having $kT_e = 25$ keV. *Solid curves*, the analytic expression (4.5) with spectral index α given by Eq. (4.8); *dashed curves*, the analytic solution with α taken to agree with the low-frequency portion of the corresponding Monte Carlo spectrum. Central photon source.

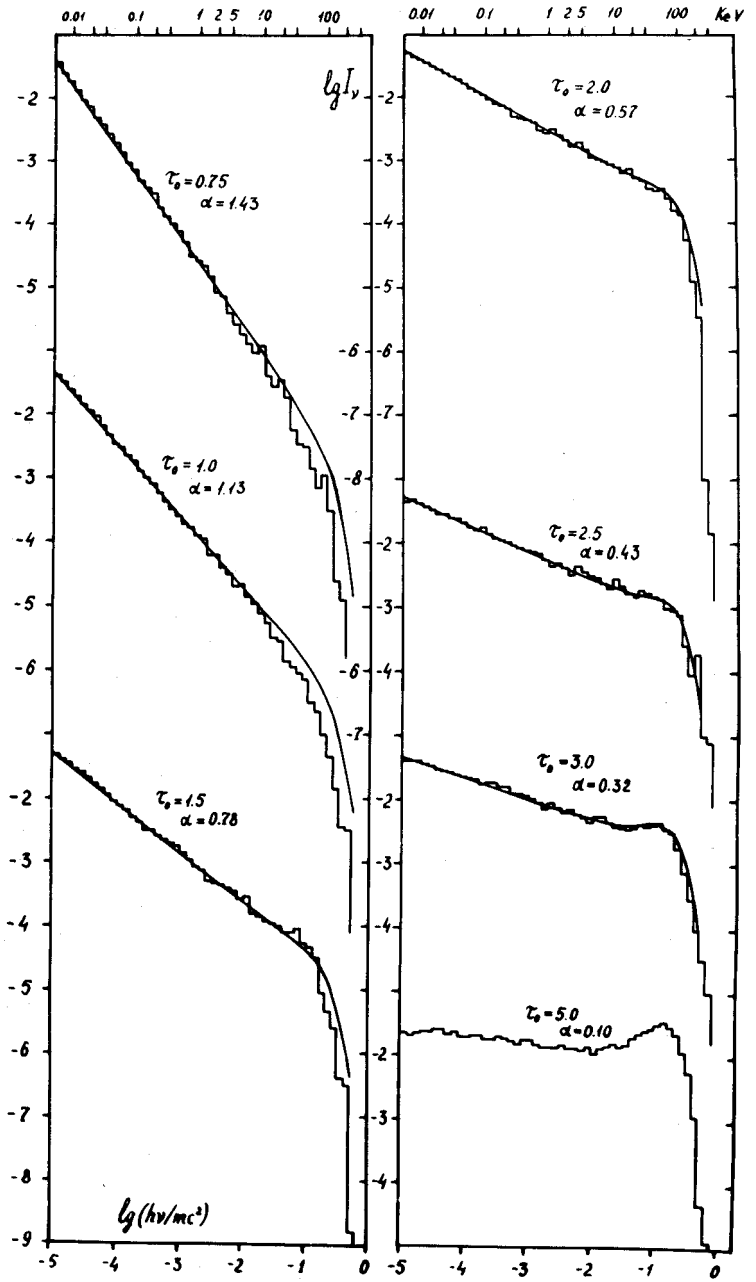

Figure 22 Comptonization of low-frequency photons in a disk having $kT_e = 25$ keV. The spectral indices α have been estimated from the low-frequency branch of the Monte Carlo spectrum and then used to construct analytic curves from Eq. (4.5).

multiple scattering and the modest change in the free path is reflected in the radiant intensity, diminishing it. For large depths ($\tau_0 > 2$) the distribution manages to develop a stable Wien tail and the lengthening of the path is much less apparent. Lorentz (1981) has arrived at a similar conclusion.

Table IV summarizes the values obtained in this way for the spectral index. In Figure 21 the approximating spectra are shown by dashed curves; they clearly fit the Monte Carlo calculations very well. The tabular values are closely satisfied by Eq. (4.8) with

$$\gamma \approx \frac{\pi^2}{4}\frac{mc^2}{(\tau + 0.5)kT_e}, \quad \gamma \approx \frac{\pi^2}{12}\frac{mc^2}{(\tau_0 + 0.9)kT_e}$$

for the spherical and disk configurations, respectively.

The form of the hard x-ray spectrum will depend on many factors: the temperature distribution over the disk (along both the radial and the vertical coordinate), its variability with time, electron temperature irregularities, the presence of an even hotter corona, and so on. If the local plasma radiation spectrum were accurately known, it still would be far from obvious that the integrated disk spectrum ought simply to represent the sum of the local spectra.

Two processes should act to distort the disk radiation spectrum. First, the material in the disk zone where most of the energy is being released will revolve in Keplerian orbits at speeds of order $(0.25–0.3)c$. We will view zones both approaching and receding from us. The spectrum will be

Table IV Computed X-Ray Spectral Indices

Spherical geometry		Disk geometry	
τ	α	τ_0	α
3	1.00	0.75	1.43
4	0.68	1.0	1.13
5	0.50	1.5	0.78
7	0.26	2.0	0.57
10	0.13	2.5	0.43
		3.0	0.32
		5.0	0.10

Doppler-distorted, the amplitude of the effect depending on the site of the emission point and the inclination angle of the system. Second, general-relativity effects should redshift the photons on their way to the observer and curve their trajectories.

A recent analysis (Kolykhalov and Syunyaev 1983) has shown that the Cyg X-1 spectrum can be reconciled with Eq. (4.5) and the Monte Carlo results if the inclination of the system is in the range $45° < i < 60°$. We have here a unique opportunity to measure the inclinations of accretion disks. Furthermore, one can infer that the black hole has a small angular momentum (it should have more nearly a Schwarzschild than a limiting Kerr metric), as one would expect for a source such as Cyg X-1, with its decidedly subcritical disk accretion ($L \ll L_{cr}$). Over the lifetime of the optical component the contribution of the accreting material would be unable appreciably to raise the mass and angular momentum of the black hole.

There has been much discussion of models wherein the x-ray emission of *quasars* similarly would be attributable to the Comptonization of low-frequency photons in an accretion disk. Figure 23 illustrates a simulation of the observed spectrum of the quasar 3C 273 (see also Figure 3). Notice that as the temperature rises the Monte Carlo results begin to depart significantly from the curve based on Eq. (4.5). Moreover, the spectrum flattens out somewhat in the 20–50 keV interval, as photons accumulate at the Wien maximum.

4.4 Angular Distribution of Photons Emerging from Disk

Monte Carlo calculations can also demonstrate how the intensity of the radiation emanating from the disk will depend on the cosine μ of the angle between the ray trajectory and the normal to the disk plane. Figures 24–26 illustrate the results of such a calculation for a disk having $kT_e = 25$ keV, $\tau_0 = 2$, and low-frequency photon sources with a blackbody spectrum corresponding to temperature $kT_r = 0.25$ keV. If all the photon sources are confined to the central plane of the disk (Figure 24), then at low energies ($h\nu < 3$ keV) only photons which have undergone comparatively few scatterings in the disk should escape from it. The situation here resembles the classical problem of radiation emerging from a semi-infinite atmosphere (for a flux independent of τ), wherein the main contribution to the opacity comes from electron scattering (Chandrasekhar 1950, Sobolev 1967). To the accuracy of our calculations we can merely say that the result is

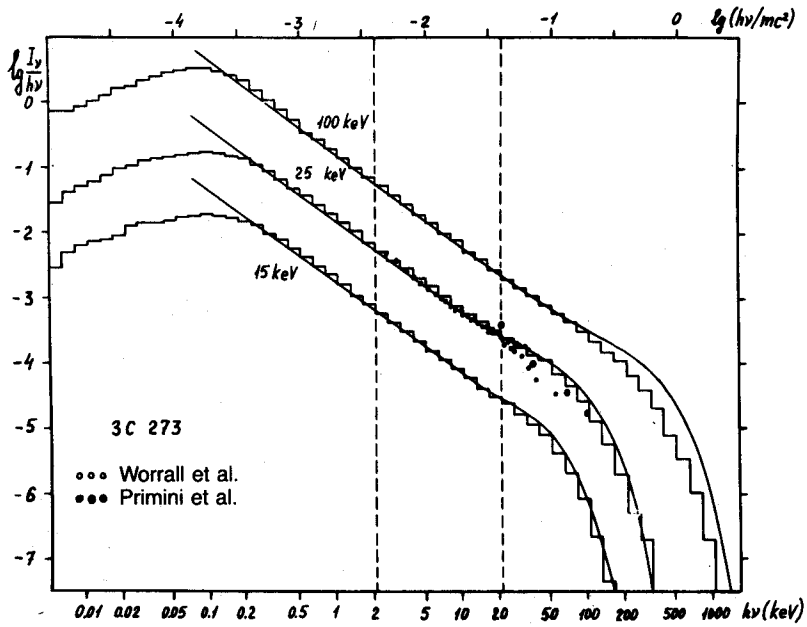

Figure 23 A Monte Carlo simulation of the spectrum of the quasar 3C 273. The disk optical depth $\tau = 3.08$ for the lower curve; $\tau = 2.36$ for the upper curve. The continuous curves represent the solution obtained by Syunyaev and Titarchuk (1980). Experimental data are from the *HEAO A2* detectors. Vertical lines bound the standard 2–20 keV x-ray region.

adequately described by the law $I_\nu(\mu) = \frac{6}{7}F_\nu\ (1 + 2\mu)$, where $F_\nu = \int_0^1 I_\nu(\mu)\mu\, d\mu$ represents the flux at a given frequency emitted by unit surface area of the disk.

For hard photons ($h\nu > 5$ keV), matters are far more interesting. These photons will have acquired their energy through Comptonization in the course of numerous scatterings (the spectrum corresponding to the problem at hand is shown by curve *A* in Figure 26), and they will have entirely forgotten where the low-frequency sources were located. From the three right panels of Figure 24 we see that the radiant intensity is virtually independent of μ: $I_\nu(\mu) = 2F_\nu/\mu$. This is a notable and by no means obvious result. Even though the two problems have similar geometry, the angular intensity distribution that will develop from Comptonization evidently differs sharply from the classical distribution.

In Figure 25 we present calculations for the case where isotropically

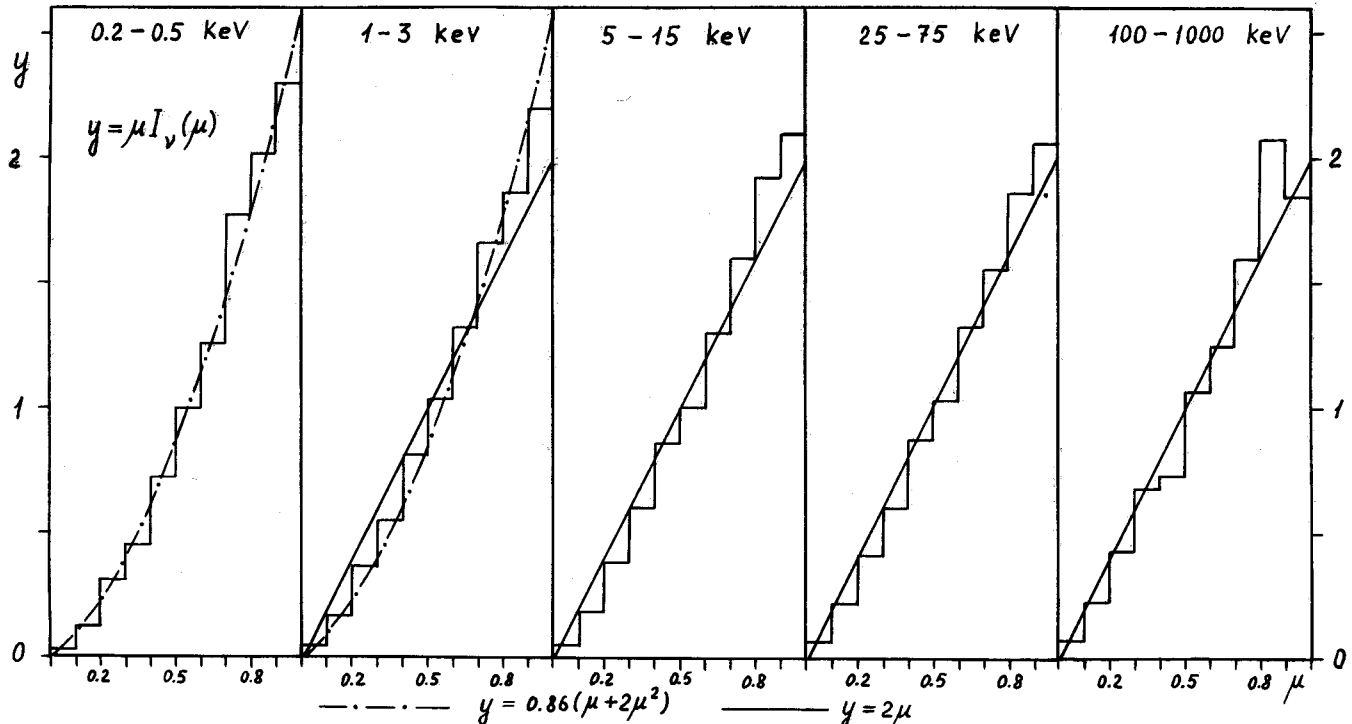

Figure 24 Angular distribution of the radiation emerging in various spectral intervals from an accretion disk having $kT_e = 25$ keV, $\tau_0 = 2$, and low-frequency blackbody photon sources ($kT_r = 0.25$ keV) confined to the central plane of the disk. Abscissa, cosine μ of the angle θ between the photon direction of travel and the normal to the disk plane; ordinate, the product $y = \mu I_\nu(\mu)$ of μ by the radiant intensity in the corresponding direction. Soft photons ($h\nu \approx 0.2$–1.3 keV) undergo few scatterings and have an angular distribution of approximately $I_\nu \propto 1 + 2\mu$, whereas hard photons ($h\nu > 5$ keV) are much scattered in the disk and have an isotropic intensity for all μ.

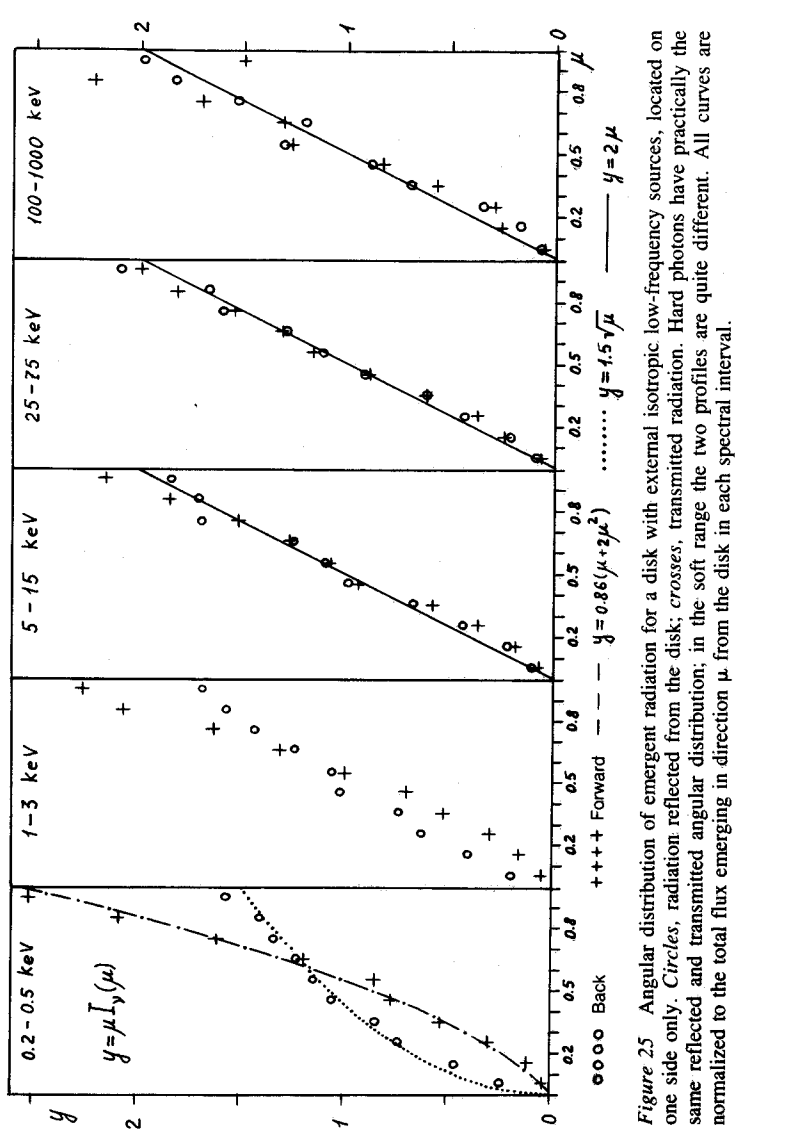

Figure 25 Angular distribution of emergent radiation for a disk with external isotropic low-frequency sources, located on one side only. *Circles*, radiation reflected from the disk; *crosses*, transmitted radiation. Hard photons have practically the same reflected and transmitted angular distribution; in the soft range the two profiles are quite different. All curves are normalized to the total flux emerging in direction μ from the disk in each spectral interval.

radiating low-frequency photon sources are located outside the disk, on one side of it. We now have to distinguish between the reflected radiation and the radiation passing through the disk. Table V indicates the ratio of the reflected to the transmitted flux, integrated over μ, for five regions of the energy spectrum. Hard photons scattered many times naturally will no longer remember the directivity of the soft photons. It is apparent from Figure 25 that, to within the accuracy of the calculations, the hard photons will have the same angular distribution on either side of the disk, in agreement with the results for photon sources confined to the central disk plane (Figure 24).

The spectrum of the radiation emerging from a disk with $kT_e = 25$ keV and $\tau_0 = 2$ is shown in Figure 26 for three different spatial configurations of the low-frequency $kT_r = 250$ eV photon sources: in the central disk plane, uniformly distributed throughout the slab, and on one side of the disk (the sum of the reflected and transmitted radiation).

As expected, the difference between the angular intensity distributions of the reflected flux and that transmitted through the disk is greatest in the soft energy interval, 0.2–0.5 keV (left panel of Figure 25). The transmitted radiation does have a distribution $I_\nu(\mu) \approx \frac{6}{7}F_\nu(1 + 2\mu)$, while the reflected radiation conforms fairly closely to the law $I_\nu(\mu) = 1.5F_\nu\mu^{-1/2}$.

Results similar to these calculations can also be obtained analytically, by applying the standard theory of light scattering in planetary atmospheres [see, for example, Sobolev (1967)]. Such an atmosphere is illuminated by a parallel beam of sunlight whose rays are incident at an angle with cosine μ_0, producing an illuminance πF on a surface normal to the beam. In the simplest case, a semi-infinite atmosphere in which the scattering function is purely isotropic, the emergent intensity will be expressed by

$$I_\nu(\tau = 0; \mu, \mu_0) = F\rho(\mu, \mu_0)\mu_0, \tag{4.9}$$

Table V Reflected/Transmitted Flux Ratio for Exterior Sources

Photon energies keV	F^-/F^+
0.2–0.5	6.8
1–3	4.1
5–15	1.4
25–75	1.1
10^2–10^3	1.1

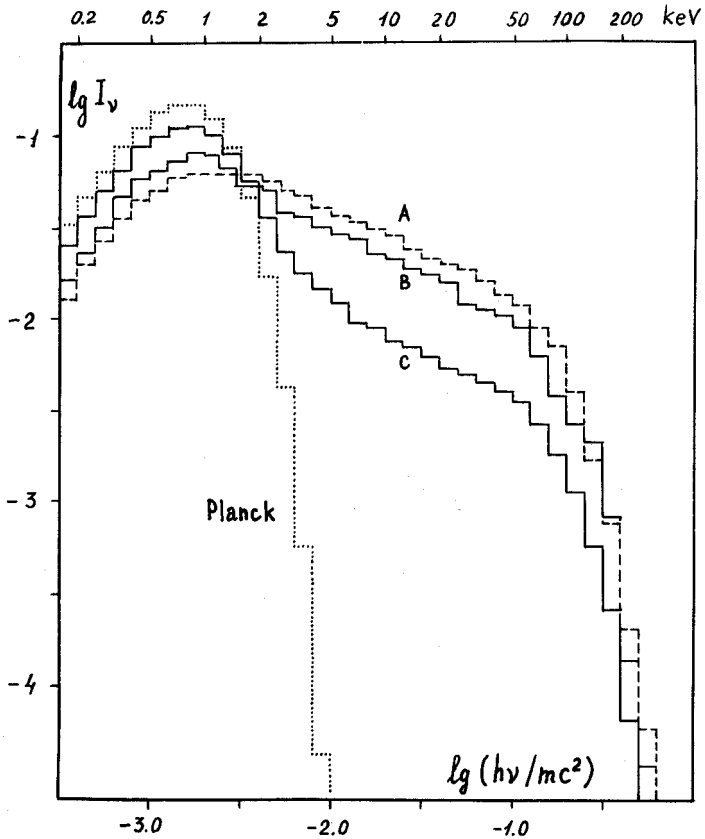

Figure 26 Spectrum of the radiation emerging from a disk whose low-frequency photon sources are: *A*) confined to the central plane (Figure 24); *B*) distributed uniformly throughout the disk; *C*) located on one side of the disk (Figure 25). The curves represent the sum of the reflected and transmitted intensities.

where the atmosphere has a brightness coefficient

$$\rho(\mu, \mu_0) = \frac{\varphi(\mu)\varphi(\mu_0)}{4(\mu + \mu_0)}. \tag{4.10}$$

A table of the standard function

$$\varphi(\mu) = 1 + \mu\varphi(\mu) \int_0^1 \frac{\varphi(\mu')\, d\mu'}{\mu + \mu'} \tag{4.11}$$

will be found in any textbook on radiative transfer theory; to adequate accuracy for our purposes it can be approximated by the simple expression $\varphi(\mu) = 1 + 2\mu$. Our calculations regard the low-frequency photon sources as isotropic emitters, located on one boundary surface of the disk. In this event,

$$I_\nu(\tau = 0; \mu) = A \int_0^1 \rho(\mu, \mu_0) d\mu_0 = A \left[(1 - 4\mu_0^2) \ln \frac{1 + \mu}{\mu} + 1 + 2\mu \right]. \quad (4.12)$$

From the condition $F_\nu = \int_0^1 I_\nu(\tau = 0; \mu)\mu d\mu \equiv 1$ we can readily evaluate the constant: $A = 1.25$. A rather good fit to the intensity (4.12) is given by the simple formula $I_\nu(\tau = 0; \mu) = 1.5\mu^{-1/2}$, and in fact this approximation agrees somewhat better with the calculations than does the analytic expression (4.12).

The angular distribution of the emergent photons will depend strongly on the disk optical thickness and on the energy range and temperature of the electrons in the disk. These relationships are graphically demonstrated by calculations we have performed for the angular distribution of the radiation in the alternative 3C 273 models whose spectra are shown in Figure 3. To illustrate, Figure 27 plots the angular distribution of the photons that would be emitted by a disk with $\tau_0 = 0.32$ and $kT_e = 250$ keV. We see that as the photons become more energetic, the radiation intensifies for $\mu \ll 1$, but in the vicinity of the normal to the disk plane the intensity diminishes. Peak intensity no longer occurs along the normal direction $\mu = 1$. Syunyaev and Titarchuk (1983) have obtained the same result by a different method. Furthermore, for high photon energies effects come into play due to the change in the scattering function and the diminished cross section given by the Klein–Nishina formula.

Because of this energy dependence of the angular distribution of the emergent photons, the emission spectrum of the disk ought to depend on the angle at which we view it. According to Figure 27, the hardest spectrum should be observed when $\mu \ll 1$; the softest, when $\mu \approx 1$. Calculations of the type depicted here and in Figure 28, which corresponds to another of the model disks, will be needed to establish the total luminosity of the object, since the radiation flux we receive turns out to be sensitive to the angle by which the disk is inclined to the line of sight.

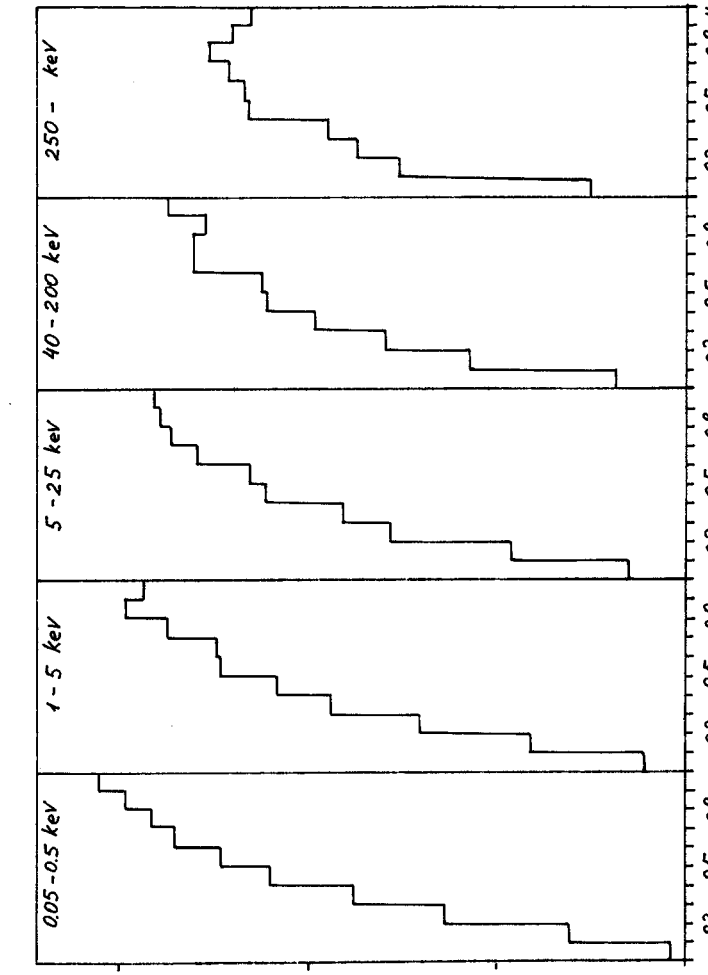

Figure 27 Angular distribution of emergent radiation resulting from Comptonization of low-frequency photons (kT_r = 0.05 keV) in a disk with τ_0 = 0.32 and kT_e = 250 keV, for several photon energy intervals. The quantity $F_\mu = \mu J(\mu)$, where $J(\mu)$ is the radiant intensity.

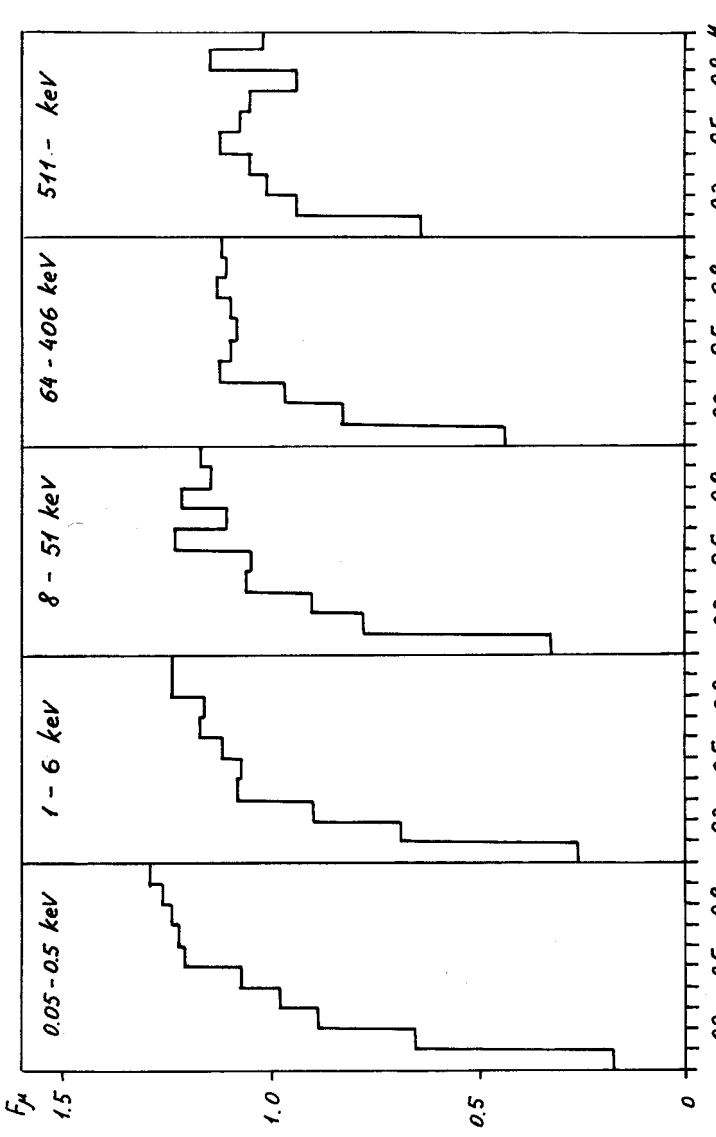

Figure 28 Angular distribution of emergent radiation resulting from Comptonization of low-frequency photons ($kT_r = 0.05$ keV) in a disk with $\tau_0 = 0.12$ and $kT_e = 500$ keV.

4.5 Polarization of Hard Radiation Generated by Comptonization in Accretion Disk

Syunyaev and Titarchuk (1983) have proposed a straightforward method of finding both the angular distribution and the polarization of the radiation produced by Comptonization in an accretion disk. For hard radiation (with $h\nu \gg h\nu_0$, where $h\nu_0$ is the characteristic energy of the low-frequency photon sources), these both prove to be independent of the photon energy and of the manner in which the low-frequency sources are distributed over the disk. The only quantity governing the polarization and the angular distribution is the disk optical depth (Figures 29 and 30).

In particular, it is interesting to see (Figure 29) that if $\tau_0 = 1$ the peak intensity will occur at $\mu = 0.43$, or in a direction about 65° from the normal to the disk. For large optical depths, $\tau_0 \geqslant 10$, the computed values nearly coincide with the classical result $I(\mu = 1)/I(\mu = 0) = 3.06$ which Chandrasekhar (1950) and Sobolev (1967) obtained for an electron-scattering atmosphere. Note that the quantity plotted in Figure 29 is $I(\mu)$, unlike Figures 27 and 28, for example, which show $F_\mu = \mu I(\mu)$.

Figure 30 presents polarization curves for the radiation emerging from an accretion disk with various optical depths τ_0. For $\tau_0 > 10$ the polarization approaches the classical Chandrasekhar–Sobolev curve, reaching 11.7 percent at $\mu = 0$ if $\tau_0 = 10$. As τ_0 diminishes the polarization reverses sign, with maximum $|p|$ being reached for small τ_0 in the range $\mu = 0.2$–0.4. This result, we would emphasize, holds only for photons which have been Comptonized in the disk, that is, which have undergone far more than the average number of scatterings there. The Syunyaev–Titarchuk method has the shortcoming that it assumes a Thomson scattering cross section and a Rayleigh scattering function. Monte Carlo calculations of the type illustrated in Figure 27 will be necessary to calculate the polarization and angular distribution of the hard ($h\nu > 100$ keV) radiation formed in a high-temperature ($kT_e > 100$ keV), optically thin ($\tau_0 < 1$) accretion disk.

4.5.1 Radiation Pressure within Disk In the inner zone of an accretion disk the thickness will be determined by the balance between the tangential component of the attractive force toward the central body and the pressure of the radiation upon the electrons (Shakura and Syunyaev 1973, 1976). By applying the discussion of Sec. 2.3.6 one can determine the pressure that would be exerted on the electrons by radiation having the spectrum observed for the source Cyg X-1 (Figure 4), the prime black hole candidate. Exact equations yield a radiation pressure 25 percent lower than the value

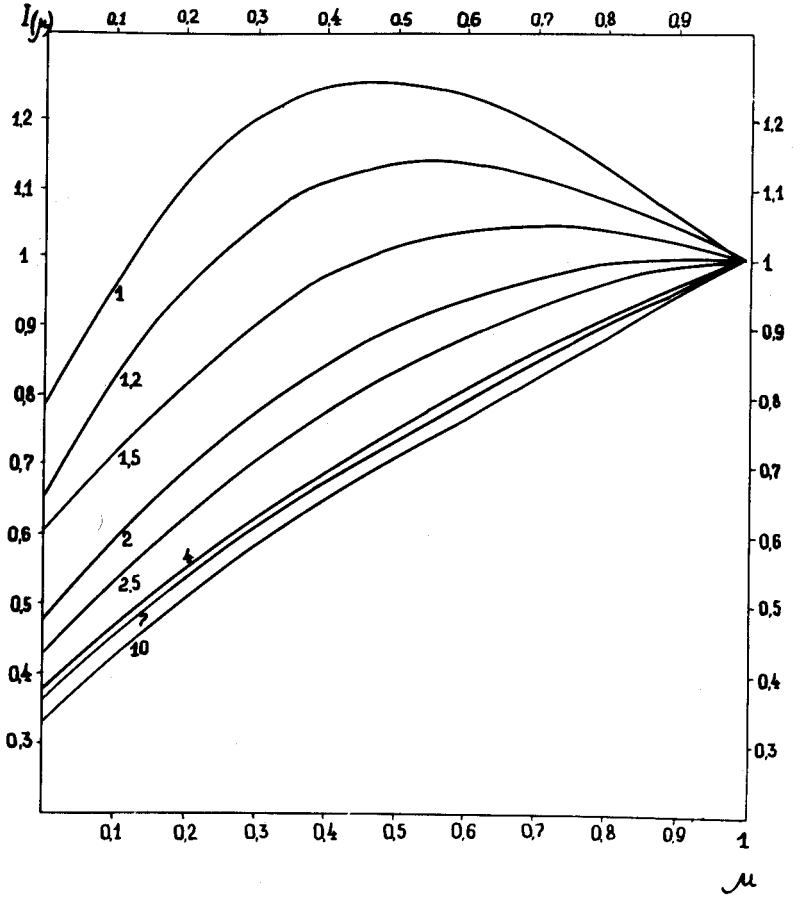

Figure 29 Angular intensity distribution of the hard radition generated by Comptonization of low-frequency photons in disks having various optical depths τ_0 (Syunyaev and Titarchuk 1983).

$\mathbf{f} = (\sigma_T/c)\mathbf{q}$ obtained in the Thomson limit. Models of specific sources should take this correction into account.

4.6 *Double Compton Emission as Source of Low-Frequency Photons*

4.6.1 Low-Frequency Photon Sources In the problem of the Comptonization of low-frequency radiation one postulates that sources of low-frequency photons are present. If spherically symmetric accretion is taking

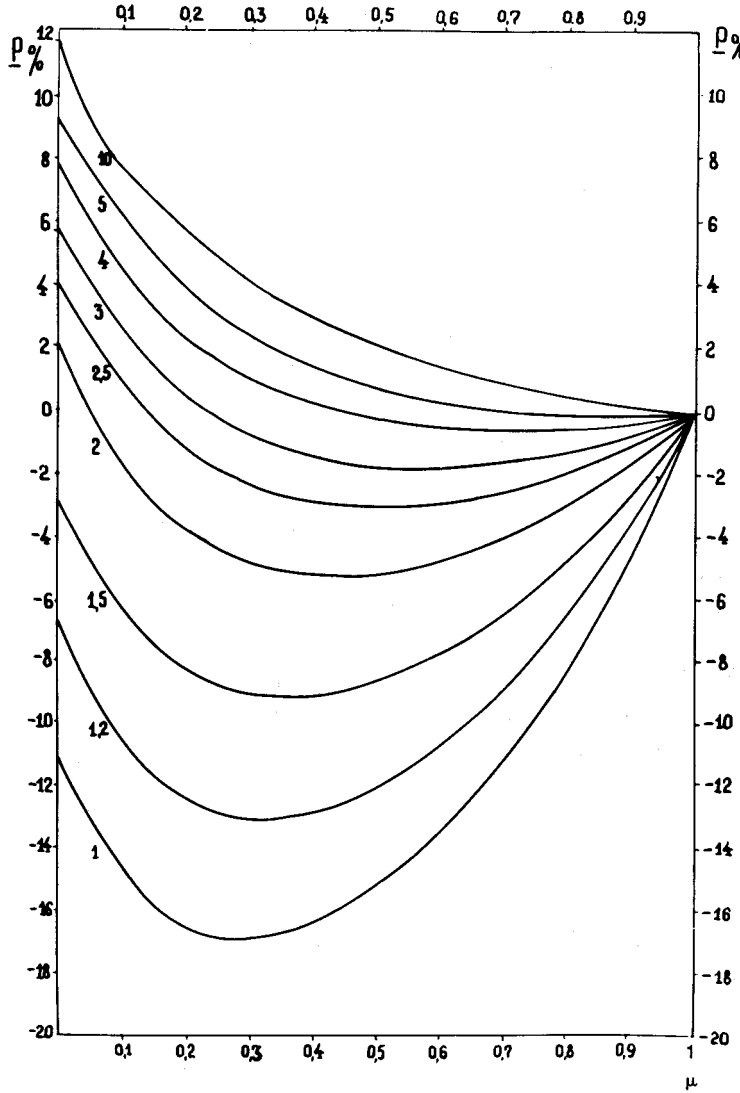

Figure 30 Percentage polarization of the hard radiation generated by Comptonization of low-frequency photons in disks having various optical depths τ_0, as a function of $\mu = \cos\theta$ (Syunyaev and Titarchuk 1983).

place onto a neutron star (or white dwarf) with a weak magnetic field, matters will be straightforward: low-frequency photons will arrive from a stellar atmosphere heated by the hard x rays of the zone where the bulk of the accretion energy is being released. For disk-type accretion onto a weak-field neutron star, such a soft-photon source will again operate—in the boundary layer indicated in panel 2 of Figure 1. In the case of a strongly magnetized neutron star, accretion will proceed in a magnetic column, but even here the neutron-star atmosphere will necessarily act as a soft-photon source: not only is it being externally heated by hard radiation, but energy is being liberated in the lower atmospheric layers due to combustion of thermonuclear fuel there as well as adiabatic heating of the contracting material.

Several years ago Shakura and Syunyaev (1973, 1976) pointed out that certain difficulties will arise with low-frequency photon sources in accretion disks around neutron stars and black holes if the luminosity is close to the Eddington limit and the turbulence parameter $\alpha \approx 1$. They remarked that thermal instability might cause the disk material to break up into cool dense clouds (optically thick with respect to true absorption, and accordingly natural sources of low-frequency photons) and a hot, energetic component in which turbulent motions would be dissipated, releasing most of the energy and resulting in Comptonization. There has also been considerable discussion of the impact on a disk of low-frequency radiation from an external source (Lightman and Rybicki 1979).

Under suitable conditions, major sources of low-frequency photons could include electrons radiating in the magnetic field at the gyrofrequency $\nu_H = (e/2\pi mc)H$ (Shakura and Syunyaev 1973), bremsstrahlung (Kompaneets 1956, Illarionov and Syunyaev 1972), and the double Compton effect, whose astrophysical role has often been considered (Weymann 1965, Gould 1972, Syunyaev and Zel'dovich 1980), with specific applications to the universe (Danese and De Zotti 1982, Syunyaev 1983), stellar interiors (Thorne 1981), and high-temperature astrophysical plasma (Lightman 1981). We will show in this section, however, that the double Compton effect cannot make any significant contribution in the case of x-ray sources. This negative result was first obtained by one of us (Syunyaev) in 1974.

4.6.2 Double Compton Effect When a photon is Compton scattered,

$$\gamma_1 + e \rightarrow \gamma_1' + e',$$

there is a small but finite probability that an additional, soft photon γ_2 will be emitted:

$$\gamma_1 + e \rightarrow \gamma_1' + \gamma_2 + e',$$

just as in the elastic scattering of an electron by a proton,

$$e + p \rightarrow e' + p',$$

there is a small but finite probability of photon emission:

$$e + p \rightarrow e' + p' + \gamma.$$

This last is the familiar bremsstrahlung process.

First of all, in bremsstrahlung the photon production probability is proportional to the square of the plasma density, but in the case of double Compton emission it is proportional to the product of the electron density N_e by the photon density N_γ. Hence if $N_\gamma \gg N_e$ the double Compton effect could become an important source of photons.

In the nonrelativistic case ($h\nu_1 \ll mc^2$, $v \ll c$), the cross section for emission of a photon of frequency $\nu_2 \ll \nu_1$ is given (Jauch and Rohrlich 1955, Akhiezer and Berestetskiĭ 1969) by

$$d\sigma_D = \frac{4}{3}\frac{\alpha}{\pi}\left(\frac{h\nu_1}{mc^2}\right)^2 (1 - \cos\theta_1)\frac{d\nu_2}{\nu_2}\, d\sigma_C, \tag{4.13}$$

where θ_1 is the scattering angle for the first photon,

$$d\sigma_C = \tfrac{3}{8}\sigma_T(1 + \cos^2\theta_1)d\cos\theta_1 \tag{4.14}$$

represents the differential Thomson scattering cross section, and $\alpha = 2\pi e^2/hc \approx 1/137$ is the fine-structure constant. On the other hand, the bremsstrahlung cross section in the nonrelativistic limit is (Jauch and Rohrlich 1955)

$$d\sigma_B = \frac{2\alpha}{\pi}\sigma_T\frac{dv}{v}\frac{1}{\beta}\ln\frac{\beta + \beta'}{\beta - \beta'}, \tag{4.15}$$

where $\beta = v/c$ specifies the velocity of the electron before it is scattered by the proton.

The spectral emissivity of Maxwellian, fully ionized hydrogen plasma due to bremsstrahlung is expressed (Allen 1973) by

$$j_\nu^{\mathrm{B}} = N_e^2 \int h\nu \frac{d\sigma_{\mathrm{B}}}{d\nu} vf(v)dv$$

$$= \sqrt{\frac{8}{3\pi}} \alpha\sigma_{\mathrm{T}} hc \left(\frac{mc^2}{kT_e}\right)^{1/2} \exp\left(-\frac{h\nu}{kT_e}\right) g(\nu, T_e)N_e^2, \quad (4.16)$$

where $g(\nu, T_e)$ is the Gaunt factor and $f(v)$ denotes the electron velocity distribution function. We can define an analogous emissivity for the double Compton effect:

$$j_\nu^{\mathrm{D}} = N_e \iint h\nu_2 \frac{d\sigma_{\mathrm{D}}}{d\nu_2} c\, d\cos\theta_1 \frac{\mathcal{E}_\nu(\nu_1)}{h\nu_1} d\nu_1$$

$$= \frac{4}{3}\frac{\alpha}{\pi} \sigma_{\mathrm{T}} \frac{h^2}{m^2c^3} N_e \int_{\nu_2}^{\infty} \mathcal{E}_\nu(\nu_1)\nu_1 d\nu_1, \quad (4.17)$$

in which $\mathcal{E}_\nu$ [erg cm^{-3} Hz^{-1}] denotes the spectral energy density of the radiation. For classical laws $\mathcal{E}_\nu(\nu_1)$ the expression (4.17) can easily be integrated. In the case of a Planck spectrum $\mathcal{E}_\nu = B_\nu = 8\pi h\nu^3 c^{-3}(e^{h\nu/kT} - 1)^{-1}$, we readily find that

$$j_\nu^{\mathrm{D}} = 1.037 \times 2^8\alpha \left(\frac{kT}{hc}\right)^3 \left(\frac{kT}{mc^2}\right)^2 hc\sigma_{\mathrm{T}} N_e$$

$$= 4.39\alpha hc\sigma_{\mathrm{T}} \left(\frac{kT}{mc^2}\right)^2 N_\gamma^0 N_e \quad (4.18)$$

in the range $h\nu_2 \ll kT$, for which the lower limit of integration in Eq. (4.17) may be set equal to zero. Here $N_\gamma^0 = 8\pi^3 \times 0.244(kT/hc)^3$ is the blackbody photon density. Since $\mathcal{E}_\nu(\nu_1)$ falls off exponentially when $h\nu_1 > kT$, the form of the expression (4.17) indicates that $j_\nu^{\mathrm{D}}(\nu_2)$ similarly should

decline exponentially for $h\nu_2 > kT$. On comparing now the expressions (4.17), (4.16), we see that for $h\nu_2 \ll kT$

$$\frac{j_\nu^D}{j_\nu^B} = \frac{4.76}{g(\nu, T)} \left(\frac{kT}{mc^2}\right)^{5/2} \frac{N_\gamma^0}{N_e}. \tag{4.19}$$

Highly simplified models for x-ray sources of the Scorpius X-1 type posit a homogeneous, isothermal plasma cloud optically thin to free–free scattering but with a large Thomson-scattering depth $\tau = \sigma_T N_e R \gg 1$ (Shklovskiĭ 1967, Neugebauer *et al.* 1969, Matsuda *et al.* 1971, Illarionov and Syunyaev 1972, Chapline and Stevens 1973, Miyamoto 1978). Two simple limiting cases may be considered (Illarionov and Syunyaev 1972): *a*) if the parameter $y = (kT_e/mc^2)\tau^2 \ll 1$, Comptonization will have little influence on the radiation spectrum; *b*) if $y \gg 1$, the spectrum inside the cloud will be practically independent of the photon source spectrum and will approximate a Wien law $\mathfrak{S}_\nu = A\nu^3 \exp(-h\nu/kT_e)$, where the constant A depends solely on the number of photons emitted by the cloud during the mean photon escape time.

4.6.3 Photon Density at Center of Cloud In a homogeneous spherical cloud let the photon sources be distributed uniformly with a volume emissivity j_γ [cm^{-3} sec^{-1}]. Then the photon density N_γ in the source will be determined by the diffusion equation

$$D\Delta N_\gamma + j_\gamma = 0 \tag{4.20}$$

with the boundary condition $[N_\gamma + \frac{2}{3} dN_\gamma/d\tau]_R = 0$. Moreover, N_γ should remain finite at every point of the cloud. Substituting the diffusion coefficient $D = c/3\sigma_T N_e$ and the expression for the Laplace operator Δ into the spherically symmetric problem, we obtain the equation

$$\frac{1}{r^2}\frac{d}{dr} r^2 \frac{dN_\gamma}{dr} + \frac{3\sigma_T N_e}{c} j_\gamma = 0, \tag{4.21}$$

whence we find

$$N_\gamma = \frac{j_\gamma R\tau}{2c}\left(1 - \frac{r^2}{R^2}\right) + \frac{2}{3}\frac{j_\gamma R}{c}. \tag{4.22}$$

Thus at the center of the cloud

$$N_\gamma = \frac{j_\gamma R}{2c}\left(\tau + \frac{4}{3}\right), \tag{4.23}$$

and photons will escape from it on a time scale $R\tau/2c$.

4.6.4 Case $y \ll 1$ If we replace j_γ by the quantity $j_\nu^B/h\nu$, we can easily find the spectrum and density of free–free photons at the center of the cloud: $\mathcal{E}_\nu^B = R(\tau + \frac{4}{3})j_\nu^B/2c$. Then for $h\nu/kT \gtrsim 1$ it follows from Eqs. (4.17), (4.16) that at the center of the cloud

$$\frac{j_\nu^D}{j_\nu^B} = \frac{2}{3}\frac{\alpha}{\pi}\left(\frac{kT_e}{mc^2}\right)^2 \tau^2\left(1 + \frac{h\nu}{kT}\right) = \frac{2}{3}\frac{\alpha}{\pi}\frac{kT_e}{mc^2}\, y\left(1 + \frac{h\nu}{kT}\right). \tag{4.24}$$

Clearly $j_\nu^D \ll j_\nu^B$ if $y < 1$. Exactly the same result is obtained in the time-dependent problem of an infinite, homogeneous medium whose photon population grows with time.

4.6.5 Case $y \gg 1$ At the center of the cloud the photons will have a Wien frequency distribution $\mathcal{E}_\nu = Ax^3e^{-x}$, where $x = h\nu/kT$. The radiant energy density $\mathcal{E}_r = \int_0^\infty \mathcal{E}_\nu d\nu = 6AkT/h$, while the photon density $N_\gamma = \mathcal{E}_r/3kT_e = 2A/h$.

According to Eq. (4.17), the double Compton emission of soft photons will have the value

$$j_\nu^D = \frac{4}{3}\frac{\alpha}{\pi}\sigma_T N_e c\left(\frac{kT}{mc^2}\right)^2 AI(x_2), \tag{4.25}$$

where $I(x) = \int_x^\infty z^4e^{-z}dz = e^{-x}(24 + 24x + 12x^2 + 4x^3 + x^4)$, so that at the center of the cloud

$$\frac{dN_\gamma}{dt} = \int_{x_0}^\infty \frac{j_\nu^D}{h\nu}\,d\nu \approx \frac{2}{9}\frac{\alpha}{\pi}\sigma_T N_e c\,\frac{\mathcal{E}_r}{mc^2}\frac{kT_e}{mc^2}\left(24\ln\frac{1}{x_0} + 50\right); \tag{4.26}$$

$x_0 \ll 1$ corresponds to the frequency at which the photon absorption rate through the double Compton effect or by free–free absorption is comparable with the rate at which the photons Comptonize upward along the frequency axis (Kompaneets 1956).

Photon production by the double Compton effect will play a significant role if Compton scatterings can yield a single photon during the mean time scale for a photon to emerge from the cloud. From the estimate $(dN_\gamma/dt)\langle t\rangle = N_\gamma$, where $\langle t\rangle = R\tau/2c$, we have the condition

$$\frac{8\alpha}{\pi}\left(\frac{kT_e}{mc^2}\right)^2 \tau^2 \ln\left(\frac{8}{x_0}\right) = 1. \tag{4.27}$$

If $x_0 \approx 10^{-4}$–10^{-2} the quantity $(kT_e/mc^2)^2\tau^2 = 5$–10, while in order for a Wien spectrum to develop we must have $y = (kT_e/mc^2)\tau^2 > 1$. The process will operate provided $kT_e/mc^2 = (5\text{–}10)y^{-1}$, that is, at very high temperatures (very large y).

On the other hand, double-Compton photon production will surpass the contribution of bremsstrahlung processes only if the source is particularly luminous and compact. Indeed, the cloud will have a luminosity $L \approx (4\pi/3)R^3\mathcal{E}_\nu/\langle t\rangle = (8\pi/3)R^2c\mathcal{E}_\nu/\tau$. Comparing j_ν^{D} with j_ν^{B}, and replacing the $\mathcal{E}_\nu$ in j_ν^{D} by L, we find that the double Compton effect will predominate if

$$\frac{L}{L_{\mathrm{cr}}} \gg 0.7\,\frac{m}{m_p}\,\frac{R}{R_{\mathrm{g}}}\left(\frac{mc^2}{kT_e}\right)^{3/2} g(x_0), \tag{4.28}$$

where L_{cr} is the critical Eddington luminosity and $g(x_0) \approx 10$ is the bremsstrahlung Gaunt factor.

The estimates above demonstrate that in a cloud with $kT_e \approx 25$ keV the double Compton effect can be of consequence only if the cloud luminosity is near-critical and the plasma has great optical depth, $\tau > 9$. In Cyg X-1 the radiation spectrum might be formed in a spherical plasma cloud with $\tau \approx 5$, not large enough for double Compton emission to play any appreciable role. We would emphasize that all our estimates are based on a Wien spectrum, so that they provide upper limits on the double Compton effect for the Cyg X-1 system, whose spectrum is much softer (Figure 4).

5 Comptonization in Weakly Relativistic Plasma

Astrophysicists encounter weakly relativistic (semirelativistic) plasma in the nuclei of galaxies and in γ-ray burst sources (Klebesadel *et al.* 1973, Mazets and Golenetskiĭ 1981). The Comptonization of low-frequency pho-

tons naturally represents one of the chief mechanisms generating the emission spectra of these objects.

For high temperatures and small optical depths the analytic treatment of the problem becomes rather crude. We have performed several calculations, assuming spherical geometry; Figure 31 shows the results for $kT_e = 50$ and 100 keV and selected τ.

Observers may be interested in our efforts to simulate the x-ray spectrum of the nucleus of the radio galaxy Centaurus A (Baity *et al.* 1981), whose spectral index $\alpha \approx 0.6$. These attempts are illustrated in Figure 32. In one case the low-frequency blackbody photon source has a temperature $kT_r = 10^{-8}\, mc^2$; in the other case, $kT_r = 1.4$ keV. Note that at low energies ($h\nu < 10$ keV) the second model fits the observations much less adequately—even if a correction is applied for photoabsorption. In the first case $kT_e = 100$ keV, $\tau = 1.5$; in the second, $kT_e = 256$ keV, $\tau = 0.55$. The geometry again is spherical. Most of our information on the plasma temperature comes from measurements in the high-energy range, $h\nu = 300$–1000 keV.

6 Comptonization in Ultrarelativistic Maxwellian Plasma

From the curves plotted in Figure 8 it is clear that plasma will become ultrarelativistic as soon as temperatures $kT_e \geqslant (1\text{–}2)mc^2$ are reached: recall that $\bar{\gamma} = 3kT_e/mc^2$ in the ultrarelativistic limit. Interest in studying the Comptonization process in ultrarelativistic plasma has been accentuated by the detection of a powerful flux of hard γ rays ($h\nu \approx 1$–6 MeV) coming from the nucleus of the Seyfert galaxy NGC 4151. We have sought to model the observed spectrum (Perotti *et al.* 1979, White *et al.* 1980), and the results are presented in Figure 33. A good fit is obtained if $kT_e = 4mc^2$ and $\tau = 0.4$. The low-frequency photon source is assumed to have a blackbody spectrum with $kT_r = 10^{-6}\, mc^2$.

It is enigmatic that the spectral region 1 MeV $< h\nu <$ 10 MeV, which dominates the radiant energy flux, makes hardly any contribution to the radiation-pressure force. The radiation pressure derives almost entirely from the 1–20 keV interval (according to Table III, if $kT_e = 2$ MeV the contribution of energies $h\nu \approx 2$ keV will be 78 times the estimate given by the Thomson approximation).

This section describes calculations of the radiation spectrum that will result when low-frequency radiation undergoes multiple scattering by weakly

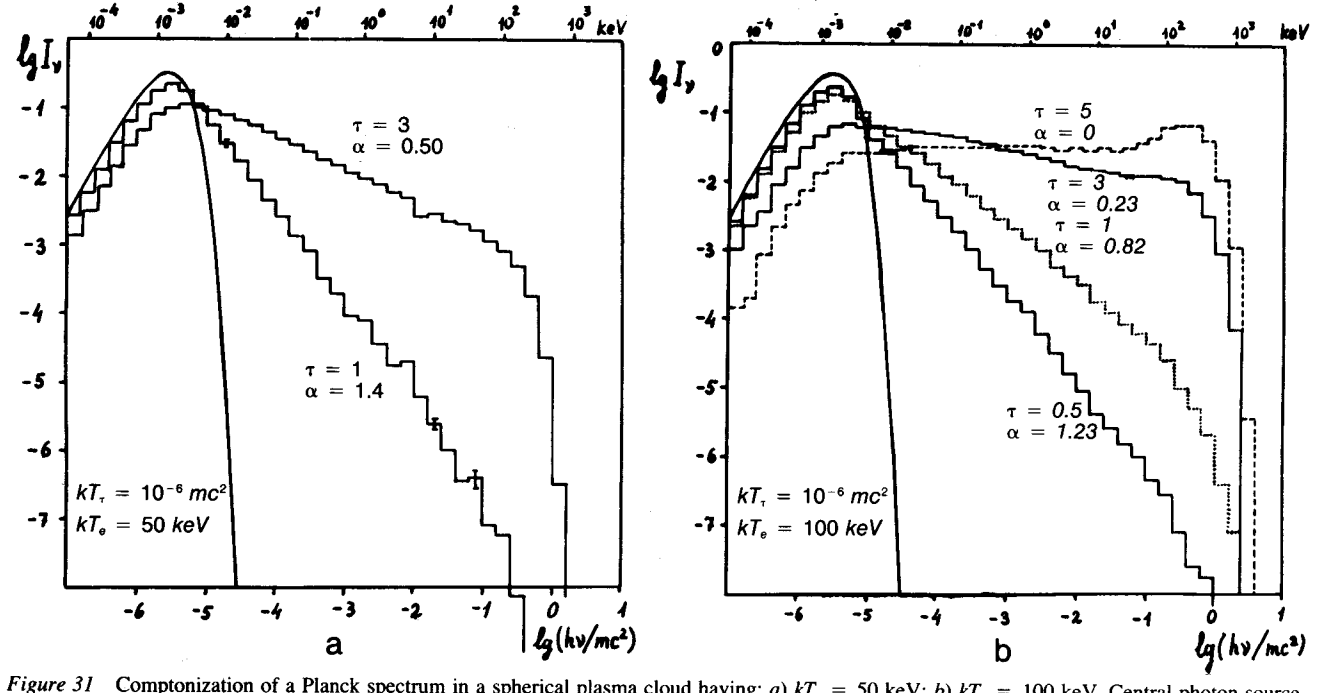

Figure 31 Comptonization of a Planck spectrum in a spherical plasma cloud having: *a*) $kT_e = 50$ keV; *b*) $kT_e = 100$ keV. Central photon source.

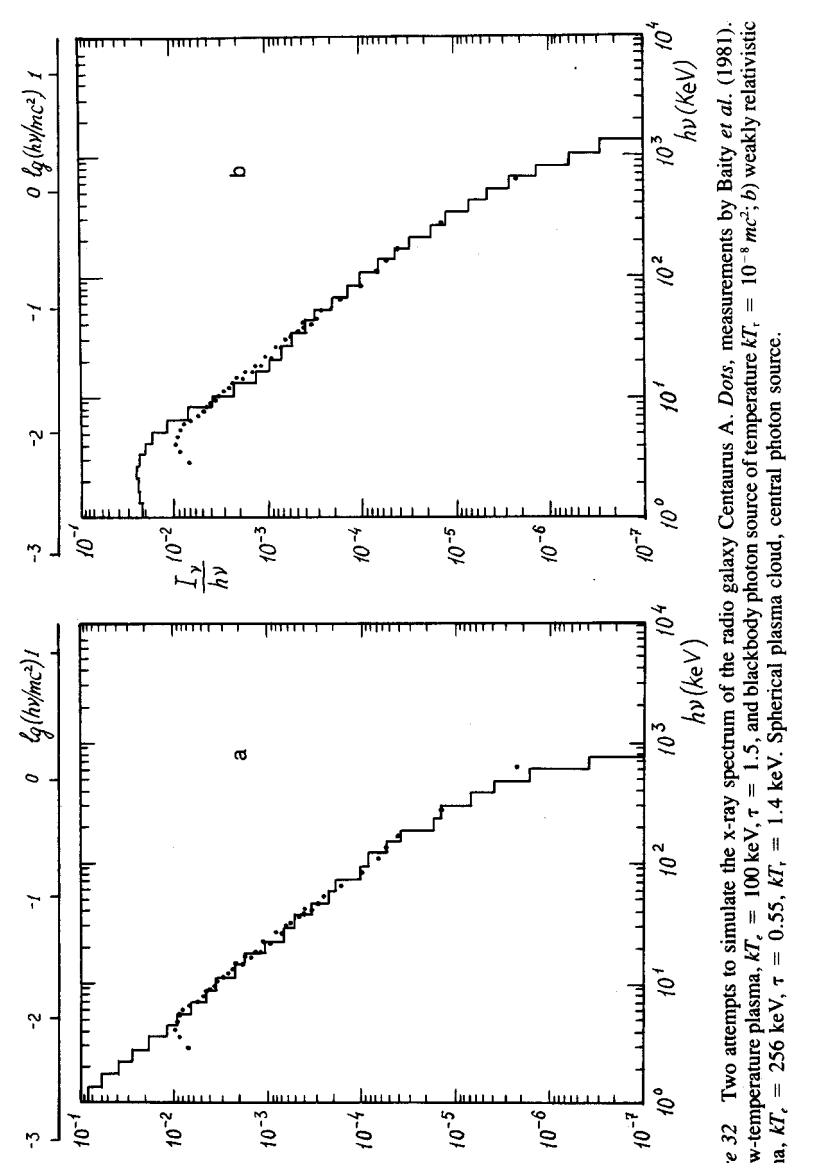

Figure 32 Two attempts to simulate the x-ray spectrum of the radio galaxy Centaurus A. *Dots*, measurements by Baity *et al.* (1981). *a*) Low-temperature plasma, $kT_e = 100$ keV, $\tau = 1.5$, and blackbody photon source of temperature $kT_r = 10^{-8}\ mc^2$; *b*) weakly relativistic plasma, $kT_e = 256$ keV, $\tau = 0.55$, $kT_r = 1.4$ keV. Spherical plasma cloud, central photon source.

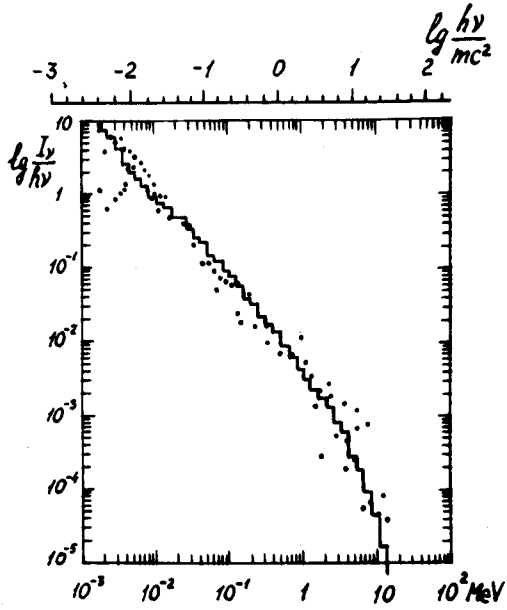

Figure 33 Simulation of the x- and γ-ray spectrum of the nucleus of the Seyfert galaxy NGC 4151 for $kT_e = 4mc^2$, $\tau = 0.4$, $kT_\gamma = 10^{-6}mc^2$. Dots, experimental data (Perotti *et al.* 1979, White *et al.* 1980); error bars omitted. Spherical plasma cloud, central photon source.

relativistic and relativistic electrons in plasma clouds whose Thomson-scattering optical depth ranges between 10^{-4} and 10. All the calculations have been performed by the Monte Carlo method.

6.1 *Statement of Problem*

Let a spherical cloud of radius R contain a uniform density N_e of Maxwellian electrons at temperature $kT_e = nmc^2$, where m denotes the electron mass. The basic parameters of the cloud will be its optical depth $\tau = \sigma_T N_e R$ to Thomson scattering and the dimensionless temperature n, which may be either greater or less than unity. At the center of the sphere place either a low-frequency blackbody source having a temperature $T_\gamma \ll T_e$, or a hard-radiation source with a power-law spectrum $I_\nu \propto \nu^{-\alpha}$ (Sec. 7). Compact low-frequency sources, whatever their actual nature, will usually experience heavy self-absorption at low frequencies, while their intensity will drop steeply in the high-frequency range; a Planck distribution should

provide a reasonably good model for simulating such spectra. A Maxwellian electron energy distribution is evidently more typical than a power law for problems of accretion onto black holes and neutron stars.† Takahara (1980, 1981) and Lorentz (1981) have lately carried out calculations of this kind for the case of a disk geometry.

6.2 *Results of Calculations*

Figures 34–37 display the spectra calculated for the radiant intensity I_ν [erg cm^{-2} sec^{-1} Hz^{-1}] emerging from a cloud with an optical depth in the range $10^{-4} \leqslant \tau \leqslant 10$ and a temperature $n = kT_e/mc^2 = 4, 2, 1, 0.5$, respectively. The radiation temperature of the central source is taken to be $kT_r = 10^{-8}\, mc^2$.

6.2.1 Basic Properties of Spectrum The frequency of a photon will increase in proportion to γ^2 each time it is scattered. As Figures 20 and 34–37 demonstrate, the main contribution to the integrated spectrum (all scattering events combined) comes from scatterings by electrons whose energy is well above average ($\gamma > 3n$, in the ultrarelativistic case). Even if the optical depth is very small, multiple scatterings will determine the form of the integrated spectrum at high frequencies. For very small τ the intensity drops exponentially in each segment of the spectrum—a consequence of the Maxwellian electron distribution. As τ increases the spectrum begins to flatten out, and when $\tau > 3$ it approaches the Wien law $I_\nu \propto \exp(-h\nu/kT_e)$, weakened on the high-frequency side by the shrinkage of the scattering cross section and the rise in the photon escape probability, according to the Klein–Nishina formula. If $\tau \leqslant 1$ and $n > 0.2$, a good fit to the integrated radiation spectrum over a wide frequency range is given by the power law $I_\nu \propto \nu^{-\alpha}$ with a single spectral index α, which can be expressed as a linear function of $\log \tau$:

$$\alpha = -\frac{\log \tau}{\log (12n^2 + 26n)} + \frac{0.2}{n}. \tag{6.1}$$

6.2.2 Removal of Energy from Electrons by Radiation The luminosity $L = 4\pi D^2 \int_0^\infty I_\nu d\nu$ of a source (D is the distance of the source) characterizes

†If τ is small, the computed curves are insensitive to the distribution law of the radiation sources over the sphere.

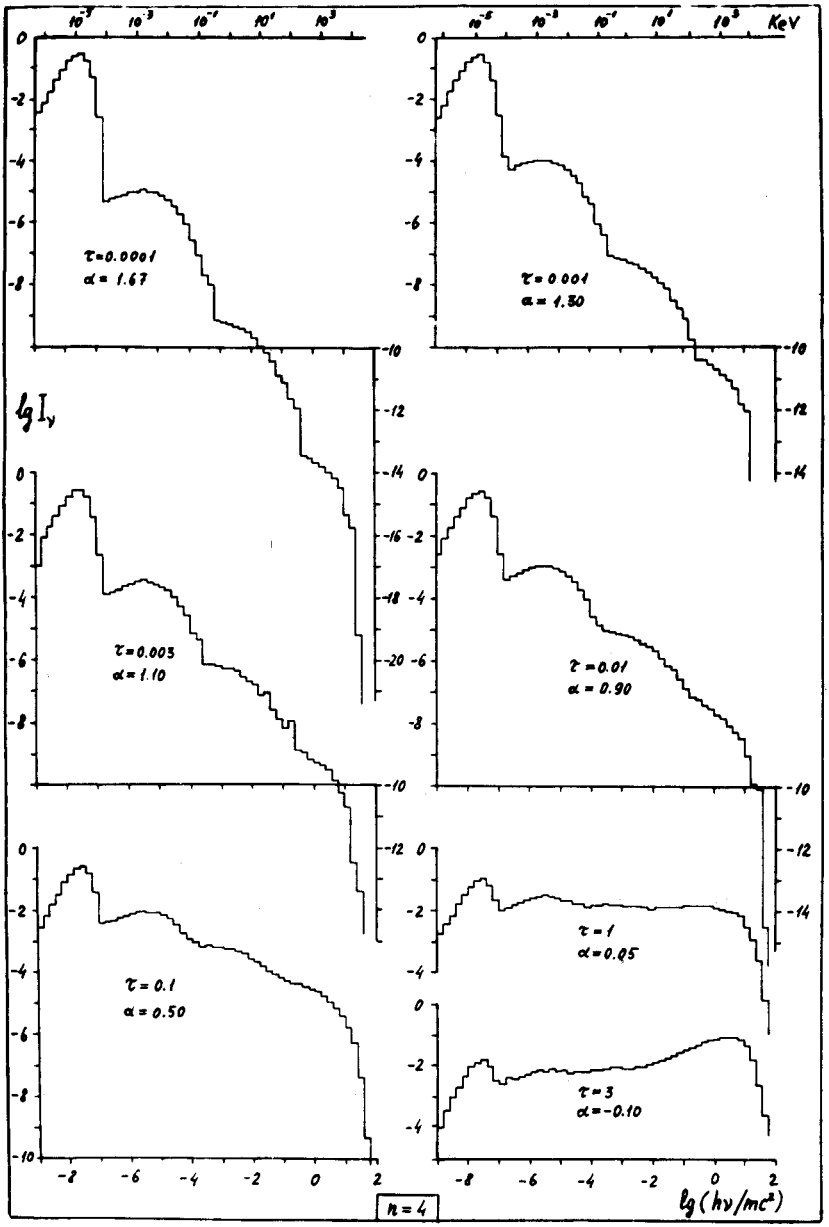

Figure 34 Comptonization of low-frequency radiation ($kT_r = 10^{-8}mc^2$) in a spherical cloud of relativistic plasma at a temperature $n = kT_e/mc^2 = 4$.

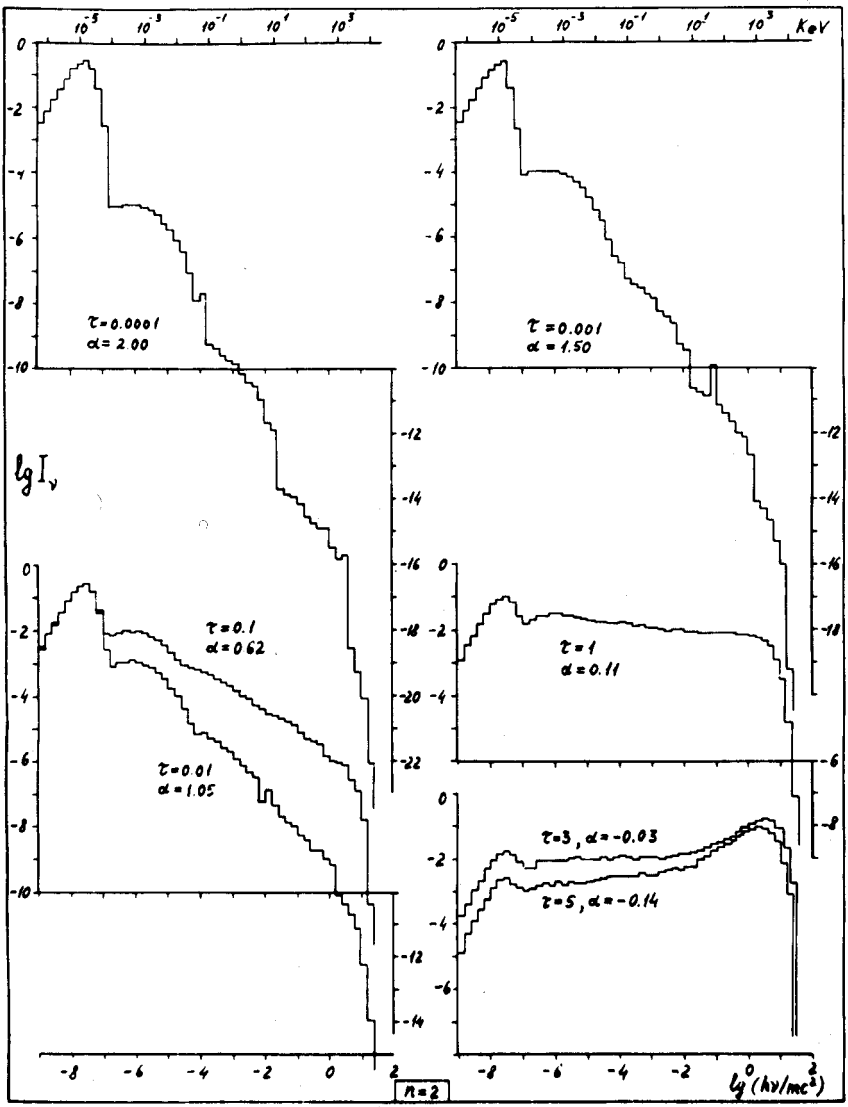

Figure 35 Comptonization of low-frequency radiation in a plasma cloud with $n = kT_e/mc^2 = 2$.

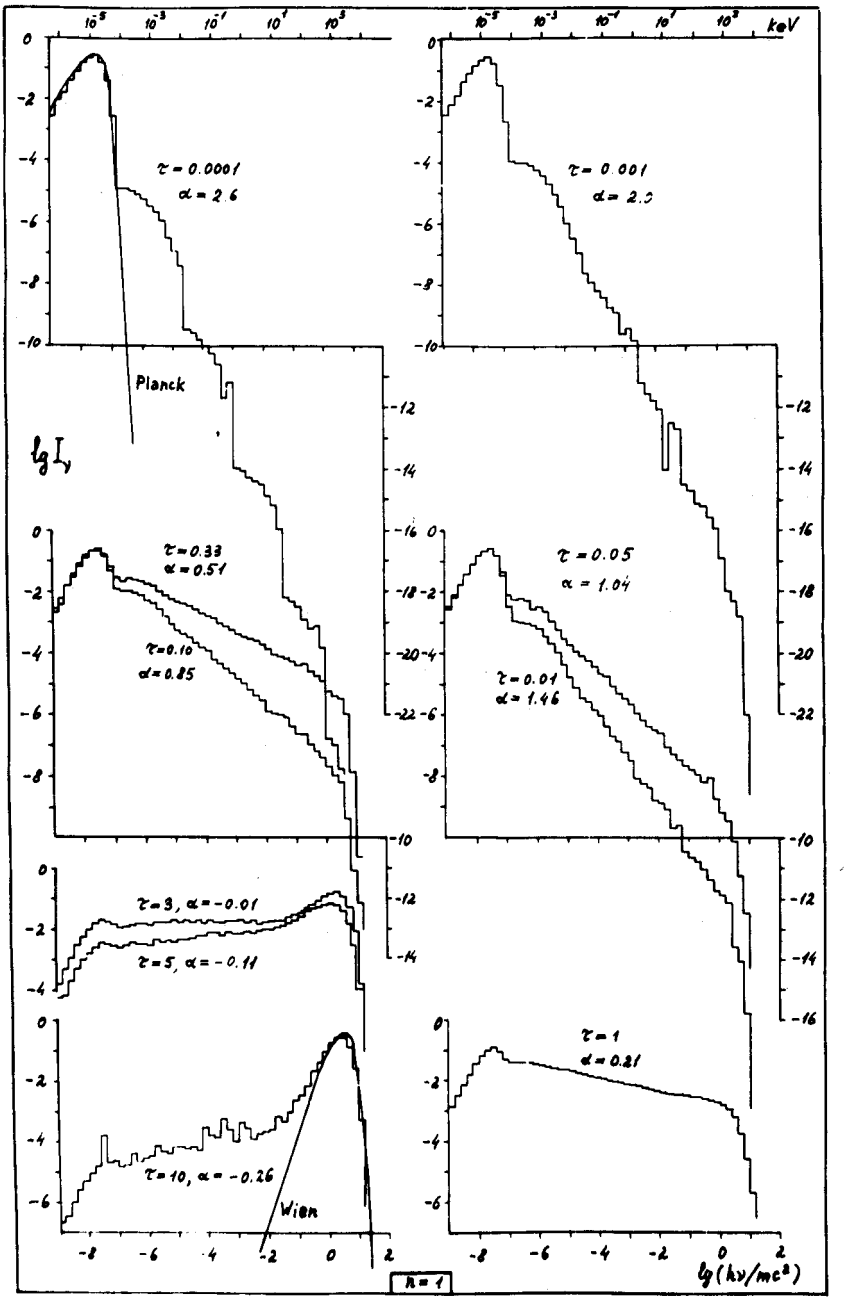

Figure 36 Comptonization of low-frequency radiation in a plasma cloud with $n = kT_e/mc^2 = 1$.

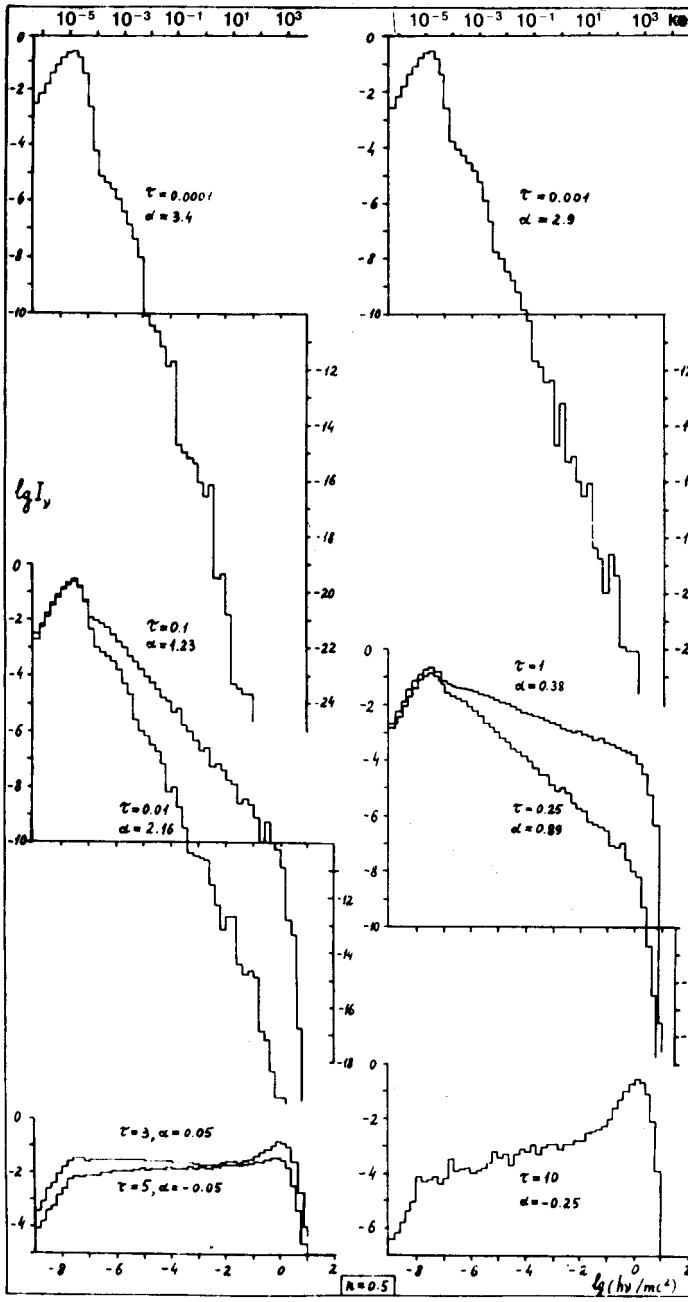

Figure 37 Comptonization of low-frequency radiation in a plasma cloud with $n = kT_e/mc^2 = 0.5$.

the rate at which the photons are withdrawing energy from the electron gas:

$$L - L_0 = L - 4\pi D^2 \int_0^\infty I_\nu(\tau = 0)\, d\nu. \tag{6.2}$$

During scattering the number of photons will be conserved. If the photons initially have a Planck spectrum, then $L_0 = 2.7\ kT_r N_\gamma$, where $N = 4\pi D^2 \int_0^\infty (I_\nu/h\nu)d\nu$ represents the number of photons emerging from the source per unit time; $2.7\ kT_r$ is the average energy of a low-frequency photon. For large optical depths ($\tau \to \infty$) a Wien emergent spectrum will develop; the mean photon energy will be $3kT_e$, so that $L_\infty \approx 3N_\gamma kT_e$. Figure 38b shows the $L(\tau)$ relation calculated for several values of $n = kT_e/mc^2$.

6.3 Spectral Index α: Analytic Estimate

When scattered by ultrarelativistic electrons of energy γmc^2, a photon will increase its frequency by a factor γ^2, on the average. For a Maxwellian electron energy distribution suppose that the mean relative increase in photon frequency is $\nu'/\nu = an^2$, where the coefficient a depends weakly on τ and n. After k scatterings the effective rise in frequency will be $\nu_k/\nu_0 = a^k n^{2k}$, so that $k = \log(\nu_k/\nu_0)/\log(an^2)$. On the other hand, if the cloud has a small optical depth then the probability of a photon experiencing a single scattering will be $1 - e^{-\tau} \approx \tau$, while the probability of k scatterings will be of order τ^k. The radiant intensity at frequency ν_k will naturally be proportional to the probability of k scatterings:

$$I(\nu_k) = I(\nu_0)\tau^k = I(\nu_0)(\nu_k/\nu_0)^{-\alpha}, \tag{6.3}$$

where $\alpha = -\log \tau/\log(an^2)$. In Figure 38a, the slope of the line for $n = 4$ is approximately $1/\log \gamma^2$, where the quantity $\gamma^2 = 12n^2$ if the relativistic electrons have a Maxwellian spectrum. This opportunity for obtaining an analytic estimate of α, first published several years ago (Pozdnyakov *et al.* 1977), was pointed out to us by Ya. B. Zel'dovich.

7 Traversal of Plasma Cloud by Hard X Rays

At the center of a plasma cloud having $\tau = 10$ and $kT_e = 0.006mc^2$, place a source of hard x rays with the power-law spectrum $I_\nu = \nu^{-\alpha}$. Many of the photons will have an energy exceeding that of the electrons, and on

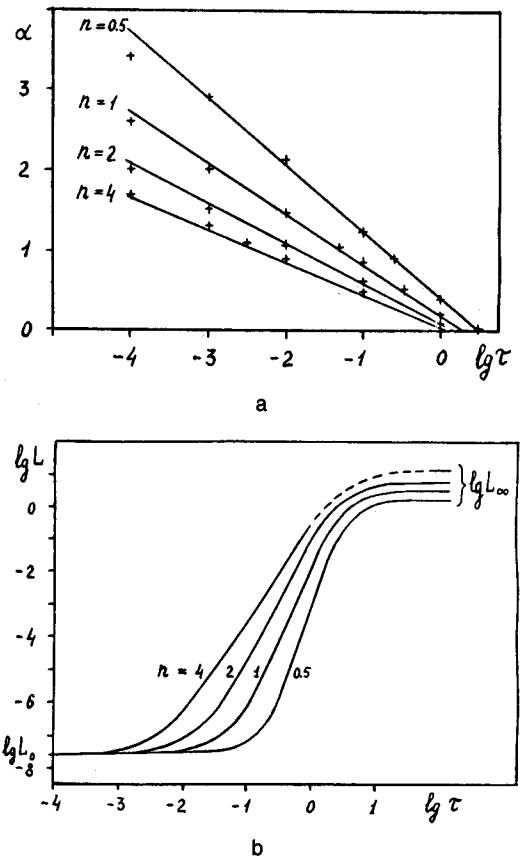

Figure 38 Comptonization of low-frequency radiation in a spherical cloud of relativistic plasma. *a*) Spectral index α as a function of log τ and n; *b*) luminosity L as a function of log τ and n.

being scattered they will deliver some of their energy to the electrons: $\Delta\nu/\nu \approx -h\nu/mc^2$. By applying the Kompaneets differential equation one can solve a problem of this kind for the case of a homogeneous, infinite medium filled with plasma. According to the solutions obtained by Illarionov and Syunyaev (1972) and Arons (1971), after the time interval t corresponding to the average number of scatterings $\tau = \sigma_T N_e ct$ the intensity of the radiation at frequencies $h\nu > mc^2/\tau$ should fall off sharply.

The authors have employed the Monte Carlo method to calculate the

emergence of hard radiation from a plasma cloud, taking into account both the downward motion of the photons along the frequency axis and their displacement in space. On the average, a photon will be scattered approximately τ^2 times in the cloud. One might think that photons more energetic than mc^2/τ^2 would not escape from the source, in view of the recoil effect as well as the solution of the kinetic equation for a homogeneous medium. Nevertheless, there is a finite probability, $e^{-\tau}$, for direct escape of a photon from the cloud. When the photon escapes it will, of course, maintain its same frequency. Thus the escape of photons scattered fewer than the average number of times ($\sim \tau^2$) in the cloud will determine the form of the spectrum at high frequencies ($h\nu > mc^2/\tau^2$).

For high-energy photons the Klein–Nishina decrease in the scattering cross section will serve to lengthen the photon free path and to increase the relative intensity of the emergent radiation. As a matter of fact, the hard-x-ray tail observed in such sources as Scorpius X-1 is sometimes attributed to passage of a portion of the hard photons emitted by the neutron-star surface through a hot, rarefied plasma cloud near the Alfvén surface of the star.

Figure 39 demonstrates how an initial power-law radiation spectrum with a sharp low-frequency cutoff will be affected in the low-frequency

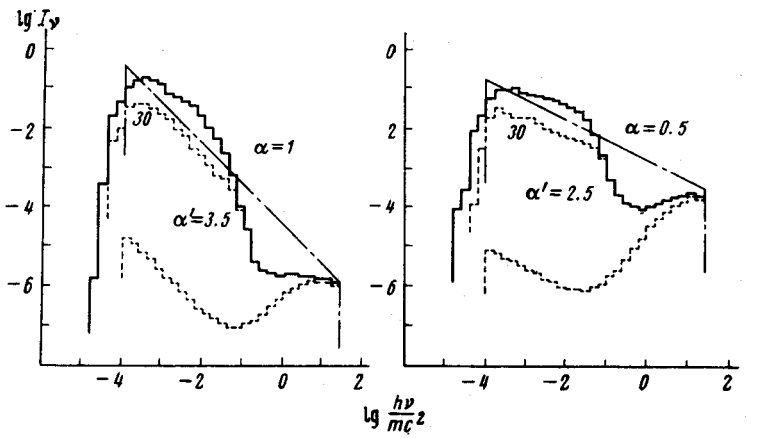

Figure 39 The transformation experienced by a power-law spectrum (straight dot–dash lines) of hard radiation as it passes through a spherical plasma cloud with $kT_e = 0.006mc^2$ and a Thomson-scattering optical depth $\tau = 10$. The dashed curves correspond to direct photon escape and to the contribution of photons scattered no more than 30 times. Central photon source.

region by Comptonization and by blurring of the boundary due to Doppler shifting as the photons are scattered by the hot electrons. In a cool plasma cloud with a large optical depth for scattering, hard radiation will be thermalized, forming a Wien spectrum (Figure 40). One other problem of much interest concerns the angular distribution and polarization of hard radiation that is reflected by a cool plasma layer (Bai and Ramaty 1978).

8 Multiple Electron Scattering in Non-Maxwellian, Ultra-relativistic Plasma Cloud

8.1 Power-Law Electron Energy Distribution

The possibility of multiple scattering also has to be considered in connection with the inverse Compton effect in clouds of relativistic electrons with a power-law energy spectrum that may occur in radio galaxies and quasars. If the electrons have a power-law spectrum $dN/dE \propto E^{-\beta}$ with a low-energy cutoff $E > E_{\min}$, then either of two mechanisms can produce a power-law radiation spectrum $I_\nu \propto \nu^{-\alpha}$.

It is well recognized that single scattering of isotropic, low-frequency photons will yield a spectral index $\alpha = \frac{1}{2}(\beta - 1)$. In fact, when scattered by a relativistic electron a low-frequency photon will, on the average, rise in frequency to $\nu' = a\gamma^2\nu$, where $\gamma = (1 - v^2/c^2)^{-1/2}$. The probability of the photon being scattered by an electron whose energy lies between γ and $\gamma + d\gamma$ is approximately $\sigma_T K\gamma^{-\beta} R\, d\gamma$, since $N_e d\gamma = K\gamma^{-\beta}\, d\gamma$. Naturally this formula also expresses the probability that a photon of initial frequency ν will reach a frequency between ν' and $\nu' + d\nu'$. To find how

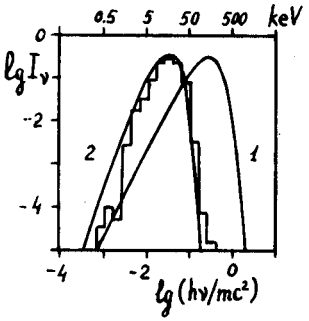

Figure 40 A test calculation illustrating the downward shift of photons along the frequency axis in plasma with $T_e < T_r$. An initial photon distribution *1* was specified as a Planck spectrum with $kT_r = 0.1mc^2$. Comptonization in a cloud with $\tau = 20$ and $kT_e = 0.01mc^2$ then produced the near-Wien spectrum *2*, with $T_r = T_e$.

the intensity depends on frequency one need only express ν' in terms of γ. Since $\gamma = (\nu'/a\nu)^{1/2}$ and $d\gamma = \frac{1}{2}(a\nu\nu')^{-1/2}d\nu'$, we can determine the frequency dependence of the number of hard photons in the interval $(\nu', \nu' + d\nu')$ emerging from a cloud with a negligible optical depth for scattering: $N(\nu') \propto \gamma^{-\beta}\, d\gamma/d\nu \propto \nu^{-(\beta+1)/2}$. Hence the intensity of the hard radiation will be $I_\nu(\nu') = h\nu' N(\nu') \propto \nu^{-(\beta-1)/2}$. In this case the power-law frequency dependence of the radiant intensity reflects the power-law energy distribution of the electrons. The problem was first solved rigorously by Ginzburg and Syrovatskiĭ (1964).

On the other hand, as shown in Sec. 6.3, if photons are multiply scattered in a cloud with $\tau \ll 1$ by the most abundant electrons, those with $E \approx E_{\min} = \gamma_{\min} mc^2$, then the spectral index will become $\alpha = -\log \tau / \log \gamma_{\min}^2$. Clearly multiple scattering will play the dominant role if $\beta > 1 - \log \tau / \log \gamma_{\min}$. For example, in a cloud with $\tau \approx 10^{-3}$ and $\gamma_{\min} \approx 30$, multiple scattering will control the form of the spectrum if $\beta > 3$; for $\tau \approx 0.1$ and $\gamma_{\min} \approx 10$, that will be the case if $\beta > 2$. In these instances, calculations will give results not much different from the case of a Maxwellian spectrum.

Figures 41 and 42 show sample cases computed numerically to illustrate the effects discussed above. The spectrum in Figure 41 is formed as each photon of blackbody radiation with $kT_r \ll mc^2$ undergoes single scattering in a cloud by ultrarelativistic electrons having the distribution $dN(p)/dp \propto$

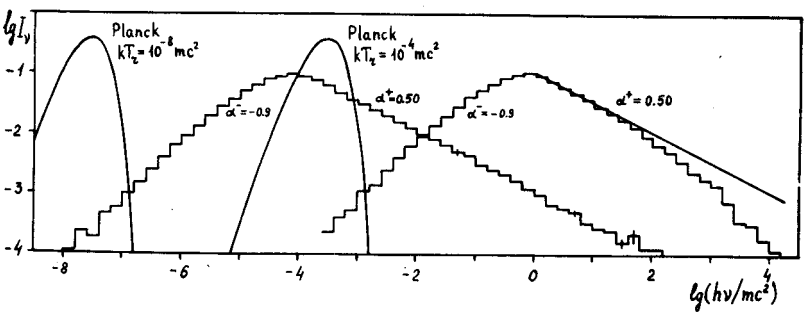

Figure 41 Spectra formed through single scattering of low-frequency photons with a blackbody spectrum by ultrarelativistic electrons with a power-law ($\beta = 2$) energy distribution over the range $30 < \gamma < \infty$. The two spectra shown have been calculated for the same electron distribution but for different temperatures of the low-frequency radiation: $kT_r = 10^{-8}$ mc^2 and $kT_r = 10^{-4}$ mc^2. The first spectrum corresponds to the analytic expressions obtained in the Thomson limit, allowing for the Doppler change in the photon frequencies; the second demonstrates the combined role of the Klein–Nishina decrease in the scattering cross section and the recoil effect (which will influence the amount by which scattering alters the photon frequency).

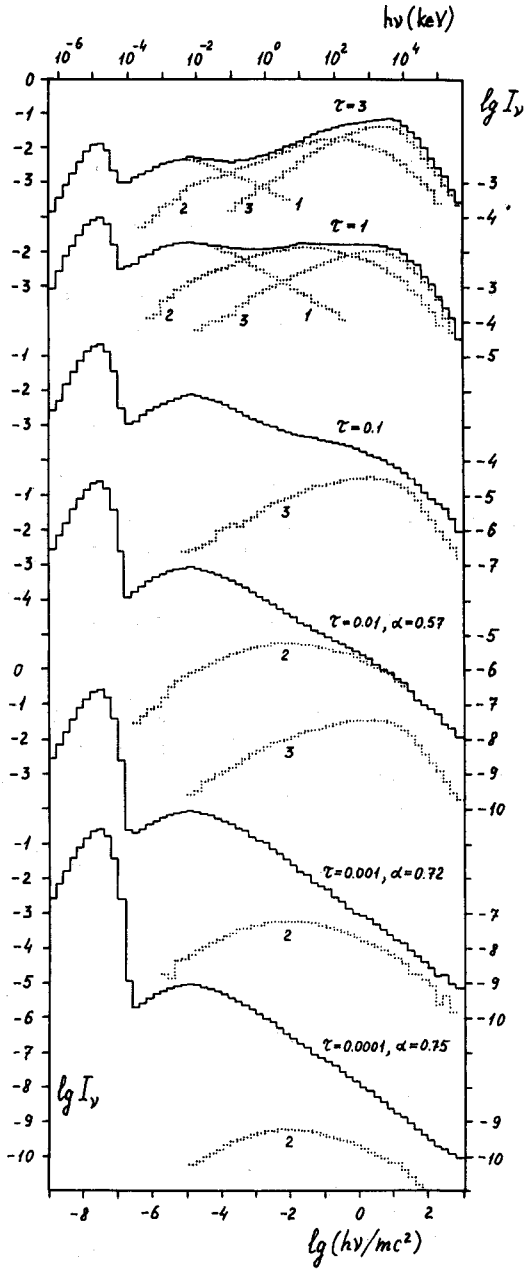

Figure 42a The role played by multiple scattering in a cloud of ultrarelativistic electrons having a power-law energy distribution of the form $\gamma^{-\beta} \exp(-\gamma_0/\gamma)$ and various Thomson-scattering optical depths τ. Curves *1*, *2*, *3* indicate the contributions of the first, second, and third scatterings. The direct-escape spectra at the left are proportional to the radiation spectrum of the low-frequency source.

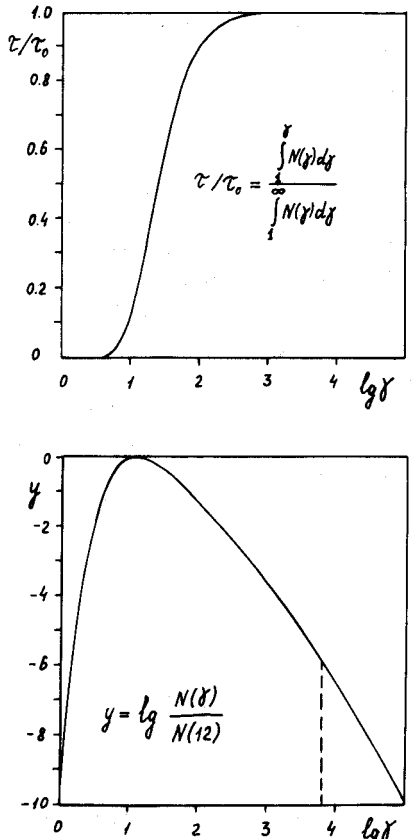

Figure 42b Lower panel, the relativistic-electron spectrum specified by the expression $N(\gamma) = K\gamma^{-2.5}e^{-30/\gamma}$. The spectrum peaks at $\gamma = 12$; by $\gamma = 6000$ it has steepened to $N(\gamma) \propto \gamma^{-3.5}$. The *upper panel* demonstrates that the main contribution to the Thomson-scattering optical depth of the cloud comes from electrons for which $10 < \gamma < 100$.

p^{-2}; that is, β has been set equal to 2. The results of this test calculation agree completely with the analytic theory of the inverse Compton effect: the spectral index of the hard radiation is $\alpha = \frac{1}{2}(\beta - 1) = 0.5$. If the photon source has a high temperature, relativistic effects will become significant; the cross section will diminish according to the Klein–Nishina formula and the law of energy exchange will be altered.

Some useful information will be found in Figure 42. Calculations have been performed for a low-frequency photon source with a Planck spectrum ($kT_r = 10^{-8}mc^2$). The relativistic electrons have been assigned a spectral index $\beta = 2.5$ (corresponding to the electrons responsible for the radio emission of radio galaxies). A cutoff energy $\gamma_0 = 30$ has been adopted, with $N(\gamma) \propto \gamma^{-\beta} \exp(-\gamma_0/\gamma)$. For values $\gamma > 6000$, the energy index has been replaced by $\beta = 3.5$. Notice that as the optical depth increases the contribution of the second scattering steadily grows, and a change occurs in the spectral index of the x and γ rays. The values of τ given in the figure correspond to the simple Thomson formula $\tau = \sigma_T N_e R$, and only relativistic electrons have been included in the calculation.

Actually we are concerned here with the Thomson-scattering optical depth τ_0 of the relativistic component in the cloud. This quantity clearly should be defined as follows:

$$\tau_0 = \sigma_T R \int_1^\infty K e^{-\gamma_0/\gamma} \gamma^{-\beta} d\gamma = \sigma_T R K \gamma_0^{1-\beta} \int_0^{\gamma_0} x^{\beta-2} e^{-x} dx, \qquad (8.1)$$

where $dN_e = Ke^{-\gamma_0/\gamma}\gamma^{-\beta}d\gamma$ specifies the energy distribution of the relativistic electrons; $\int_1^\infty dN_e$ represents the electron number density. In the particular case $\beta = 2.5$ we have

$$\tau_0 = \frac{\sqrt{\pi}}{2} \sigma_T R K \gamma_0^{-3/2}. \qquad (8.2)$$

Beyond question, however, if along with the relativistic electrons the source contains nonrelativistic plasma with $\tau < 10^{-1}$, the emergent radiation spectrum will be decisively altered, since the probability of multiple scattering will rise.

Indeed, suppose the cloud has optical depths $\tau \ll 1$, $\tau_0 \ll 1$ with respect to nonrelativistic and relativistic electrons. Then the probability of a photon escaping from the cloud immediately after its nth scattering will be approximately $(\tau + \tau_0)^n(1 - \tau - \tau_0)$. Using Newton's binomial theorem we

obtain the following probability of escape after r scatterings by relativistic electrons:

$$\tau_0^r \sum_{n=r}^{\infty} \frac{n!}{r!(n-r)!} \tau^{n-r}(1-\tau-\tau_0) = \frac{\tau_0^r(1-\tau-\tau_0)}{(1-\tau)^{r+1}}. \quad (8.3)$$

Denoting the probability (8.3) by

$$p_r(\tau) = \tau_0^r(1-\tau)^{-r-1}(1-\tau-\tau_0), \quad (8.4)$$

and writing the photon escape probability in the absence of cool plasma as $p_r(0) = \tau_0^r(1-\tau_0)$, we obtain the ratio

$$\frac{p_r(\tau)}{p_r(0)} = \frac{1-\tau-\tau_0}{(1-\tau_0)(1-\tau)^{r+1}}. \quad (8.5)$$

If $\tau_0 \ll \tau \ll 1$, the ratio (8.5) will have the leading terms

$$\frac{p_r(\tau)}{p_r(0)} = 1 + r\tau + O(\tau^2). \quad (8.6)$$

Thus the influence of the cool plasma will increase with the scattering multiplicity r. One should recognize that because of the recoil effect scattering by the cool electrons might also significantly distort the radiation spectrum and serve to warm the cool component.

8.2 *Monoenergetic Electrons*

Calculations have been performed for the following model. A cloud of relativistic electrons has a Thomson-scattering optical depth τ_0. At its center is a low-frequency photon source with $kT_r = 10^{-10}mc^2$ (two upper panels in Figure 43) or $kT_r = 100$ eV (lower panel). The electrons are monoenergetic, with $\gamma_0 = 1000$. We are interested in the spectrum of the photons emerging from the cloud.

The spectrum of Planck photons that have been scattered once by monoenergetic, ultrarelativistic electrons can easily be calculated analytically in the Thomson approximation. In this way we obtain the solid curve shown in the middle panel of Figure 43 for $\tau_0 = 10^{-2}$ and the dashed curve in

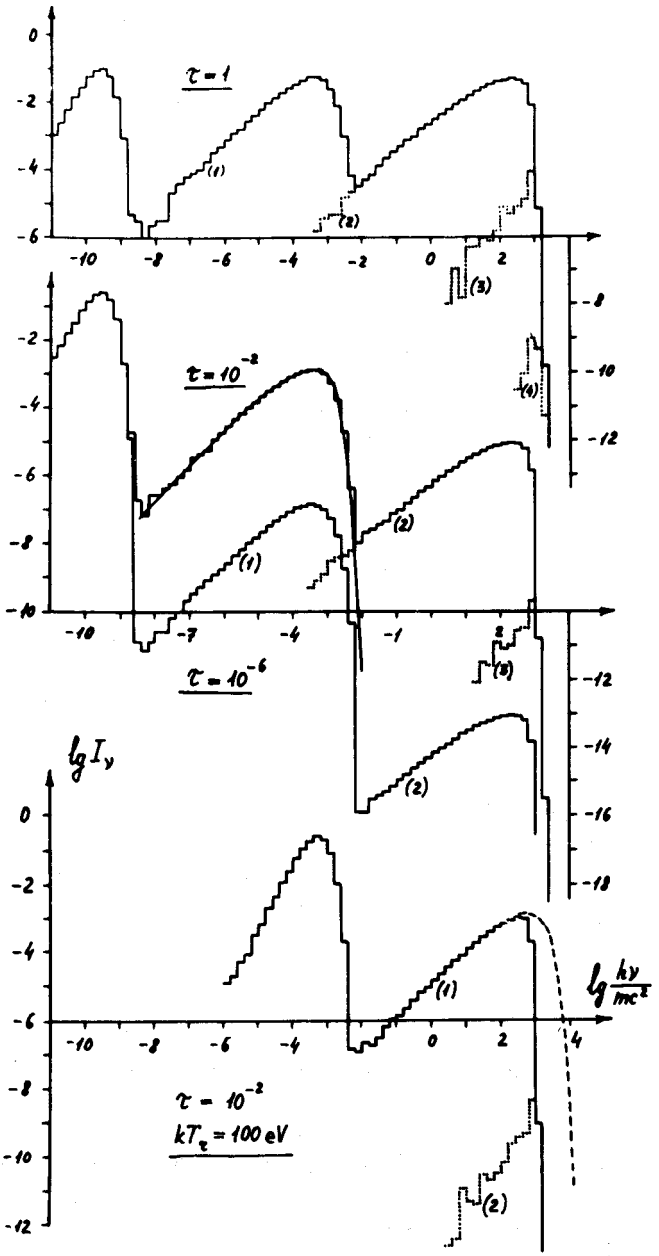

Figure 43 Radiation spectrum formed through Comptonization of low-frequency blackbody photons in a cloud of monoenergetic electrons ($\gamma_0 = 1000$), for several different optical depths with respect to scattering. In the two upper panels the photon source has $kT_r = 10^{-10}$ mc^2.

the lower panel. Clearly in the first case we have an excellent fit to the Monte Carlo results; this agreement served as a check on the calculation. In the lower panel, however, the Monte Carlo curve differs radically from that based on the Thomson approximation—a consequence of the Klein–Nishina corrections to the scattering cross section and the recoil effect, which diminishes the buildup of energy by a photon as it is scattered by ultrarelativistic electrons (compare Figure 8). As a result of these effects the contribution of the third and fourth scatterings to the integrated radiation spectrum turns out to be very small, even when $\tau_0 = 1$. The accumulation of photons in the energy range $h\nu \sim \gamma_0 mc^2$ which might have been expected actually does not take place. Evidently even in the case $\tau \gg 1$ the development of a Wien spectrum will be unlikely.

9 Monte Carlo Techniques for Comptonization Problems

The term Monte Carlo methods refers to numerical procedures for solving mathematical problems by modeling of random variables. Other names are in use as well: synonyms include the method of statistical, or stochastic, tests. In fact, there is no universally accepted definition of Monte Carlo methods. Without dwelling on the advantages of the definition offered above, let us outline some of its features.

In the first place we would emphasize that Monte Carlo methods are numerical techniques; thus they compete with other numerical procedures but not with exact, analytic solution methods.

Second, one can apply the Monte Carlo approach to mathematical problems of any kind, not just to those of probabilistic character. It is important to understand that in many cases simulating a probability process is not the best way to solve problems associated with that process. On the contrary, by renouncing simulation one can sometimes manage to develop considerably more efficient methods of calculation.

Such methods are indeed exemplified by the successful application of Monte Carlo techniques to Comptonization problems. Figure 20, for instance, illustrates a radiation spectrum calculated numerically in which the intensity covers the full range from 10^{-1} to 10^{-24}; yet not even a modern computer is capable of determining event probabilities lower than, say, 10^{-8} by simulating those events.

Third, the definition itself implies that before attempting to cope with

specific problems by the Monte Carlo method one must learn how to model various random variables on a computer.

A fuller explanation of Monte Carlo techniques in general will be found in a book by Sobol' (1973).

9.1 *Modeling Random Variables*

Pseudorandom numbers. A sequence of independent values $\xi_1, \xi_2, \ldots$ of the random variable ξ distributed uniformly on the interval (0, 1) are called ordinary *random numbers*. By using functions of the type $g(\xi_1)$, $g(\xi_1, \xi_2)$, . . . one can construct random variables having other distribution laws. The process of computing values for any random variable by means of ordinary random numbers is termed *modeling*, or "drawing," the random variable.

The concept of "real" random numbers is a mathematical abstraction; there are no such numbers in nature. In place of "real" random numbers, calculations make use of *pseudorandom numbers:* numbers computed from specified formulas (thus they are not random at all, in the usual sense of the word) but satisfying some set of tests just as though they were "real" random numbers.

The most widespread procedure for obtaining pseudorandom numbers is the method of residues (also called the congruential method or the multiplicative method) proposed by D. H. Lehmer. That is how pseudorandom numbers have been computed in our own investigations.

Method of residues. We define a sequence of integers, beginning with $m_0 = 1$, by means of the expression

$$m_k \equiv 5^{17} m_{k-1} \pmod{2^{40}}, \qquad k = 1, 2, \ldots;$$

in other words, m_k is the remainder left when $5^{17} m_{k-1}$ is divided by 2^{40}. Our pseudorandom numbers will then be the quantities

$$\xi_k = 2^{-40} m_k.$$

Method of inverse functions. This method should be considered the basic procedure for modeling random variables. Suppose we require values of a random variable whose distribution function is $F(x)$.

Let $x = G(y)$ be the function inverse† to the function $y = F(x)$; then the expression $\eta = G(\xi)$ will define a random variable with the distribution function $F(x)$. In fact, the probability

$$\mathcal{P}\{\eta < x\} = \mathcal{P}\{G(\xi) < x\} = \mathcal{P}\{\xi < F(x)\} = F(x),$$

since ξ is distributed uniformly on the interval (0, 1).

Example. The free path λ of a photon in a homogeneous medium is a random variable conforming to the exponential law $\mathcal{P}\{\lambda < x\} = 1 - e^{-x/\bar{\lambda}}$, where $\bar{\lambda}$ is the mean free path. The method of inverse functions gives us an expression for modeling the free path of an individual photon: $\lambda = -\bar{\lambda} \ln (1 - \xi)$. Since the random variables ξ and $1 - \xi$ have the same distribution, we can simplify this last expression to: $\lambda = -\bar{\lambda} \ln \xi$.

One special case of the inverse-function method is the following technique for modeling random variables with a discrete distribution. Suppose we require values of a random variable η which may take any of a finite or infinite set of values $x_1, \ldots, x_m, \ldots$ with the probability $p_m = \mathcal{P}\{\eta = x_m\}$. Naturally $\Sigma p_m = 1$.

It can be proved that in this situation the relation $\eta = G(\xi)$ will yield:

$$\eta = x_1 \quad \text{if} \quad \xi < p_1,$$

$$\eta = x_2 \quad \text{if} \quad p_1 \leqslant \xi < p_1 + p_2,$$

$$\eta = x_3 \quad \text{if} \quad p_1 + p_2 \leqslant \xi < p_1 + p_2 + p_3,$$

and so on.

Example: photoabsorption. If a photon has an energy $h\nu > 7$ keV, its photoabsorption by an iron ion will, with 0.34 probability, be accompanied by the emission of a $K\alpha$ photon, whose energy $h\nu = 6.4$ keV. To model the outcome of a collision between the original photon and an iron ion, we draw the next random number ξ. If it turns out that $\xi < 0.34$, we consider that a $K\alpha$ photon will be emitted; if $\xi \geqslant 0.34$, it will not be.

†The function $F(x) = \mathcal{P}\{\eta < x\}$ is nondecreasing, but not necessarily continuous: it may have discrete jumps and intervals of constancy. In cases where it is not evident how to construct the inverse function, one may use the following generalized definition: $G(y) = \inf x$, the lower bound to be taken over the set of all x such that $F(x) > y$.

The inverse-function method enables one to simulate multidimensional random variables. Suppose we require values of a random vector $(\eta_1, \ldots, \eta_n)$ whose density $p(x_1, \ldots, x_n)$ is known. Then we represent this density as a product of conditional densities, say $p(x_1, \ldots, x_n) = p_1(x_1)p_2(x_2|x_1)p_3(x_3|x_1, x_2) \cdots p_n(x_n|x_1, x_2, \ldots, x_{n-1})$, in arbitrary order. Next we consider the conditional distribution functions

$$F_i(x|x_1, \ldots, x_{i-1}) = \int_{-\infty}^{x} p_i(t|x_1, \ldots, x_{i-1})\, dt$$

which correspond to these densities, as well as the functions $x = G_i(y|x_1, \ldots, x_{i-1})$ inverse to $y = F_i(x|x_1, \ldots, x_{i-1})$. Using n random numbers $\xi_1, \ldots, \xi_n$, we can evaluate the components of the vector $(\eta_1, \ldots, \eta_n)$ successively from the relations $\eta_1 = G_1(\xi_1)$, $\eta_2 = G_2(\xi_2|\eta_1)$, $\ldots$, $\eta_n = G_n(\xi_n|\eta_1, \ldots, \eta_{n-1})$.

Unfortunately, it is not uncommon for the inverse function $G(y)$ to take an excessively cumbersome form, and one has to look for other ways to model the corresponding random variable. To speed up the calculations one may, for example, compile a $G(y)$ table, and later evaluate $\eta = G(\xi)$ from the table. But even this approach is far from universal: one often encounters families of distribution functions that depend on parameters, and under such circumstances one must cope with multidimensional tables.

Method of superposition. Suppose we want to obtain values of a random variable η whose distribution function $F(x)$ can be represented as a superposition of distribution functions $F_m(x)$:

$$F(x) = \sum_m c_m F_m(x),$$

where all the $c_m > 0$, and $\Sigma c_m = 1$ (either a finite or an infinite number of terms). Denoting by $G_m(y)$ the function inverse to $y = F_m(x)$, we introduce the random number α, which may take the values $\alpha = 1, 2, \ldots$ with probabilities $\mathcal{P}\{\alpha = m\} = c_m$.

We define the following procedure for drawing values of η: we select two random numbers ξ_1, ξ_2, and using ξ_1 we draw a number α. From ξ_2 we now find the value of $\eta = G_\alpha(\xi_2)$. The distribution function of η will then be $F(x)$.

The validity of this procedure is ensured by the formula for the total probability:

$$\mathcal{P}\{\eta < x\} = \sum_m \mathcal{P}\{\eta < x | \alpha = m\}\mathcal{P}\{\alpha = m\} = \sum_m F_m(x)c_m = F(x).$$

Example. When photons are scattered by cool electrons the scattering angle θ will obey the Rayleigh law: the random variable $\mu = \cos\theta$ will have the probability density $p(x) = \frac{3}{8}(1 + x^2)$, for $-1 < x < 1$. If the inverse-function method were applied to this example, we would have to solve the cubic equation $\mu^3 + 3\mu + 4 = 8\xi$ each time we needed a value for μ. With the superposition method, by setting $p_1(x) = \frac{1}{2}$, $p_2(x) = \frac{3}{2}\mu^2$, $c_1 = \frac{3}{4}$, $c_2 = \frac{1}{4}$ we obtain the explicit modeling expressions:

$$\mu = \begin{cases} 2\xi_2 - 1 & \text{if } \xi_1 < \frac{3}{4}, \\ (2\xi_2 - 1)^{1/3} & \text{if } \xi_1 \geq \frac{3}{4}, \end{cases}$$

Multidimensional modeling functions. Rich opportunities are available in the simulation of random variables if one takes advantage of a more general type of modeling function: $\eta = g(\xi_1, \xi_2)$, $\eta = g(\xi_1, \xi_2, \xi_3)$, ... In fact, the superposition method relies on a function of the form $\eta = g(\xi_1, \xi_2)$. However, few general methods of this kind have been worked out, and we limit attention to a single example (without proof).

Example. A random variable η will conform to a gamma distribution if its probability density

$$p(x) = \frac{a^m}{\Gamma(m)} x^{m-1} e^{-ax}, \qquad 0 < x < \infty.$$

For integers $m = n$ the quantity η can be modeled by the expression $\eta = -a^{-1} \ln(\xi_1 \cdots \xi_n)$, while for half-integers $m = n + \frac{1}{2}$ the modeling formula becomes

$$\eta = -a^{-1} [\ln(\xi_1 \cdots \xi_n) + (\ln \xi_{n+1}) \sin^2(2\pi\xi_{n+2})].$$

Change of variables. In certain problems the modeling formulas can be simplified by changing the variables (recall that in a one-to-one transfor-

mation of variables the density will be multiplied by the absolute value of the Jacobian of the reciprocal transformation).

Example: a random point distributed uniformly over the sphere $x^2 + y^2 + z^2 < R^2$. Inside the sphere such a point will have the constant density $p(x, y, z) = (\frac{4}{3}\pi R^3)^{-1}$. If one attempts to use the representation $p = p_1(x)p_2(y|x)p_3(z|x, y)$, one obtains very complicated modeling formulas. However, the spherical coordinates of the point prove to be independent:

$$p(r, \theta, \varphi) = p(x, y, z)r^2 \sin\theta = \frac{3r^2}{R^3}\frac{\sin\theta}{2}\frac{1}{2\pi},$$

and are readily modeled by the inverse-function technique:

$$r = \xi_1^{1/3} R, \qquad \cos\theta = 2\xi_1 - 1, \qquad \varphi = 2\pi\xi_3.$$

Example. It is not hard to verify that the last two expressions specify a random direction, or, properly speaking, a random direction under circumstances such that all directions are equally probable. Hence the unit vector $\mathbf{v}^0 = \{v_1^0, v_2^0, v_3^0\}$ can be modeled from the two random numbers ξ_1, ξ_2:

$$v_3^0 = 2\xi_1 - 1, \qquad v_2^0 = [1 - (v_3^0)^2]^{1/2} \sin 2\pi\xi_2,$$

$$v_1^0 = [1 - (v_3^0)^2]^{1/2} \cos 2\pi\xi_2.$$

Rejection technique. Consider a random variable η defined by the condition

$$\eta = g(\xi_1, \ldots, \xi_m) \quad \text{if} \quad (\xi_1, \ldots, \xi_m) \in B, \tag{9.1}$$

where B is some fixed region in m-dimensional space. To compute η from expressions of the type (9.1) we choose m random numbers $\xi_1, \ldots, \xi_m$ and test the selection criterion $(\xi_1, \ldots, \xi_m) \in B$. If it is satisfied, we compute $\eta = g(\xi_1, \ldots, \xi_m)$; otherwise we take a new group of random numbers $\xi_1, \ldots, \xi_m$ and test the criterion again.

Equations (9.1) define the rejection technique for modeling η. The selection probability

$$\mathfrak{E} = \mathcal{P}\{(\xi_1, \ldots, \xi_m)\} \in B$$

is called the *efficiency* of the technique (9.1). On the average $m/\mathfrak{E}$ random numbers have to be consumed in order to obtain one value of η from Eqs. (9.1).

Rejection techniques are often used to simulate truncated distributions or to select uniformly distributed points covering complicated regions. The following algorithm, usually called the *generalized von Neumann method*, has many practical applications.

Assume that the probability density $p(x)$ in which we are interested can be represented as a product of the form

$$p(x) = k_1 p_1(x) f(x), \tag{9.2}$$

where k_1 is a constant, $p_1(x)$ is the density of an auxiliary random variable η' which we are able to model, and $0 \leq f(x) \leq c_1$.

Modeling algorithm. Select a pair of values η', ζ' such that ζ' is uniformly distributed in the interval $(0, c_1)$ and is independent of η'; if $\zeta' < f(\eta')$, then set $\eta = \eta'$.

Proof. The number of pairs η', ζ' for which $x < \eta' < x + dx$ is proportional to $p_1(x)\,dx$; among these the number of selected values $\eta = \eta'$ is proportional to $f(x)$. Hence the number of values of η falling within the interval $(x, x + dx)$ will be proportional to $p_1(x)f(x)\,dx$, as required.

The efficiency of a rejection technique based on the representation (9.2) is readily calculated:

$$\mathfrak{E} = \mathcal{P}\{\zeta' < f(\eta')\} = \int_{-\infty}^{\infty} \int_0^{f(x)} p_1(x)\, c_1^{-1}\, dx\, dy = \frac{1}{c_1 k_1}. \tag{9.3}$$

We shall make use of the representation (9.2) in Secs. 9.4 and 9.5.

9.2 *Calculation of Averages*

The crude Monte Carlo method. In the great majority of the problems that are handled by the Monte Carlo method, average values—mathemat-

ical expectations—have to be calculated. Suppose that we are interested in a certain quantity a. We shall devise a random variable η and a function $f(\eta)$ such that the mathematical expectation of $f(\eta)$ is a; that is,

$$\mathbf{M}f(\eta) = a.$$

From this last relation we can develop a Monte Carlo method to evaluate a.

In fact, let $\eta_1, \ldots, \eta_N$ be independent values of the variable η. We form the estimate

$$\theta_N = \frac{1}{N} \sum_{s=1}^{N} f(\eta_s).$$

According to the law of large numbers, as $N \to \infty$ the estimate θ_N will converge stochastically to a. In other words, for large enough N, we will have $a \approx \theta_N$.

Error estimates. If the dispersion

$$\mathbf{D}f(\eta) = \mathbf{M}f^2(\eta) - a^2$$

is finite, then by the central limit theorem of probability theory the quantity θ_N will be asymptotically normal, and its *probable error* will be given approximately by

$$r_N = 0.675 \sqrt{\mathbf{D}f(\eta)/N}. \tag{9.4}$$

Since $\mathcal{P}\{|\theta_N - a| > r_N\} \approx 0.5$, $\mathcal{P}\{|\theta_N - a| < r_N\} \approx 0.5$ for all sufficiently large N, the quantity r_N provides a rough measure of the error. The error itself, $|\theta_N - a|$, can be two or three times as large as r_N, but it can also be smaller than r_N.

The value of the dispersion appearing in Eq. (9.4) is readily estimated in the course of calculating θ_N, for

$$\mathbf{M}f^2(\eta) \approx \frac{1}{N} \sum_{s=1}^{N} f^2(\eta_s);$$

the dispersion need not be estimated to any great accuracy.

Another way to estimate the error is the following. We divide the sample $\eta_1, \ldots, \eta_N$ into several independent subsamples and calculate averages for each of them. Regarding these averages as approximately normal, we can estimate the probable error from a table of Student's distribution.

Finally, the uncertainty of the approximation $a \approx \theta_N$ can be assessed as θ_N is being established, say by comparing the θ_N values for $N = 1000$, 2000, 4000, ... This is the least rigorous procedure, of course.

Comparison of Monte Carlo methods. Equation (9.4) shows that as N increases the probable error will fall off as $N^{-1/2}$. That is a slow rate of decline: in order to develop one further decimal place the sample size N, and hence the volume of computations, would have to be increased a hundredfold. Clearly there is no hope of achieving high accuracy by this route.

However, the same quantity a can be calculated by using different values of η and different functions $f(\eta)$, provided only that $\mathbf{M}f(\eta) = a$. From Eq. (9.4) we see that if the number N of trials is fixed, then the probable error will depend on the value of the dispersion $\mathbf{D}f(\eta)$. Much attention has therefore been given in the theory of Monte Carlo methods to procedures for choosing η and $f(\eta)$ so as to make the dispersion $\mathbf{D}f(\eta)$ as small as possible; indeed, it is claimed that the *accuracy* of the Monte Carlo method is defined by the dispersion $\mathbf{D}f(\eta)$.

But the expression for θ_N still does not determine the calculation algorithm; one requires a formula for modeling η by means of random numbers. A Monte Carlo algorithm is completely specified by two relations:

$$\theta_N = \frac{1}{N}\sum_{s=1}^{N} f(\eta_s), \qquad \eta = g(\xi_1, \xi_2, \ldots).$$

Let t denote the computer time expended in calculating a single value of η and a single value of $f(\eta)$. The product $t \cdot \mathbf{D}f(\eta)$ is called the *laboriousness* of the Monte Carlo algorithm. If the total computer time $T = Nt$ is held fixed, then the less laborious the algorithm, the smaller will be the probable error:

$$r_N = 0.675\sqrt{t \cdot \mathbf{D}f(\eta)/T}.$$

Statistical weights. Assume that the random variable η has the probability density $p_\eta(x)$, so that

$$a = \int_{-\infty}^{\infty} f(x)p_\eta(x)dx.$$

Select an arbitrary random variable ζ whose density $p_\zeta(x)$ is positive at all points x for which $f(x)p_\eta(x) \neq 0$. Then the expression for a may be written in the form

$$a = \int_{-\infty}^{\infty} f(x)w(x)p_\zeta(x)dx,$$

where the function $w(x) = p_\eta(x)/p_\zeta(x)$ is called the *statistical weight*. In view of the last integral above,

$$a = \mathbf{M}f(\zeta)w(\zeta).$$

Thus instead of averaging the values of $f(\eta)$, one may take an average over $f(\zeta)$ with the weight $w(\zeta)$ and use the estimate

$$\tilde{\theta}_N = \frac{1}{N}\sum_{s=1}^{N} f(\zeta_s)w(\zeta_s).$$

The dispersions of the two quantities $f(\eta)$ and $f(\zeta)w(\zeta)$ differ, since

$$\mathbf{M}f^2(\eta) = \int_{-\infty}^{\infty} f^2(x)p_\eta(x)dx$$

whereas

$$\mathbf{M}f^2(\zeta)w^2(\zeta) = \int_{-\infty}^{\infty} f^2(x)w(x)p_\eta(x)dx.$$

It therefore is usually maintained that if the weight $w < 1$, the weighting method will be advantageous, as it will diminish the dispersion.

That claim ought to be refined, however: the inequality $w(x) < 1$ cannot hold for all x, for it is equivalent to the inequality $p_\eta(x) < p_\zeta(x)$. But these functions are both normalized, with $\int p_\eta(x)dx = \int p_\zeta(x)dx = 1$. Nevertheless, one can have a situation in which $w(x) < 1$ at all points where $f(x) \neq 0$, or in which $w(x) < 1$ in the region of greatest importance.

Remark. It is not hard to show that we will have minimum dispersion $\mathbf{D}f(\zeta)w(\zeta)$ if $p_\zeta(x)$ is proportional to $|f(x)|p_\eta(x)$. In practice, however, it is not possible to choose such a density, because its normalization would involve the integral $\int|f(x)|p_\eta(x)dx$, whose evaluation would be equivalent

to calculating the required integral a. Using densities $p_\zeta(x)$ qualitatively similar to $|f(x)|p_\eta(x)$ is called *importance sampling*.

9.3 *Statistical Weights in Radiative Transfer*

Many problems that arise in radiative transfer theory can be handled by introducing weights on the basis of purely physical arguments. If such weights are used, the efficiency of the Monte Carlo method will sometimes be much improved.

Particle-escape weighting. Suppose we are investigating the passage of particles through a finite, homogeneous region G. From some point $\mathbf{r}_i$ within G let a particle begin to move in the direction $\mathbf{\Omega}_i$, its energy remaining unchanged as it traverses its free path. In our simulation we would calculate the distance l_i to the boundary of G (along the direction $\mathbf{\Omega}_i$) and draw a value for the free path length $\lambda = \lambda_i$. If $\lambda_i > l_i$, the particle will be considered to have escaped; otherwise it will undergo a collision at the point $\mathbf{r}_{i+1} = \mathbf{r}_i + \lambda_i\mathbf{\Omega}_i$.

Now let us assign to the model particle a weight† w_i. Knowing the distance l_i, we can readily calculate the probability that our particle will escape from G: $\mathcal{P}\{\lambda > l_i\} = \exp(-l_i/\bar{\lambda}_i)$. We shall regard "a portion" of the particle, with weight $w_i \exp(-l_i/\bar{\lambda}_i)$, as escaping from G, while "the remainder" of the particle, with weight $w_{i+1} = w_i - w_i \exp(-l_i/\bar{\lambda}_i)$, will experience a collision within G. It is easy to see that the free path λ within G for the portion of the particle with weight w_{i+1} will obey the truncated exponential distribution $\mathcal{P}\{\lambda < x\} = [1 - \exp(-x/\bar{\lambda}_i)]/[1 - \exp(-l_i/\bar{\lambda}_i)]$. We therefore obtain a formula different from the one given in Sec. 9.1 for drawing a path length $\lambda = \lambda_i$ within G:

$$\lambda = -\bar{\lambda}_i \ln [1 - \xi(1 - e^{-l_i/\lambda_i})].$$

With such a modeling technique the particle trajectory will theoretically be infinite (provided absorption within G is absent or is taken into account by weights; see below). In practice one will stop computing the trajectory as soon as the cutoff criterion $w_{i+1} < \epsilon$ is satisfied for preassigned ϵ, or as soon as the remaining particle ceases to interest us (for instance, its energy may drop below some threshold).

A tremendous advantage is won by using such weights in problems with a region of small depth $\tau \ll 1$. For example, if $\tau = 10^{-3}$, simulation would

†Intuitively, one may consider a moving packet of w_i identical particles.

demand consideration of more than a million particles in order to obtain only a few doubly scattered particles. On the contrary, when weighing is introduced to allow for escapes each model particle will experience numerous (theoretically, infinitely many) scatterings, but after each scattering its weight will drop about a thousandfold. The energy spectrum of emergent photons illustrated in Figure 20 was compiled from only $N = 20{,}000$ trajectories. This diagram shows the contribution of individual scattering events to the spectrum as well as some of the probable errors (vertical segments). Despite the fantastically low (from the simulation standpoint) probabilities involved, the uncertainty in the results is held to a perfectly acceptable level.

The contribution of multiply scattered photons to the spectrum will increase with the value of τ.

Estimate of dispersion. Place a source of photons, which may undergo scattering, inside a sphere of optical radius τ. We wish to calculate the spectrum of the radiation emerging from the sphere.

Let A_{mj} designate an event whereby a photon, immediately after its mth scattering, escapes with an energy belonging to the jth energy interval, and let $S_{mj} = \mathcal{P}\{A_{mj}\}$ be the probability of event A_{mj}. The quantities S_{m1}, S_{m2}, . . . will evidently determine the spectrum of those photons which escape directly after their mth scattering.

Now let us consider the simulation scheme for calculating the S_{mj}. In selecting a photon from the source and modeling its fortunes we are in effect calculating a random variable η_{mj} which will take the value 1 if event A_{mj} occurs and 0 otherwise. Thus $\mathbf{M}\eta_{mj} = S_{mj}$, $\mathbf{D}\eta_{mj} = S_{mj} - S_{mj}^2$.

If instead the probability S_{mj} is computed using the weights described above, then each photon will make the contribution $\tilde{\eta}_{mj} = w_m \exp(-l_m/\bar{\lambda}_m)$, provided its energy after the mth scattering belongs to the jth interval; otherwise $\tilde{\eta}_{mj} = 0$. As before, we will have $\mathbf{M}\tilde{\eta}_{mj} = S_{mj}$.

Let q_m be an upper bound on the possible values of $\tilde{\eta}_{mj}$; that is, $q_m = \sup w_m \exp(-l_m/\bar{\lambda}_m)$. We will show that

$$\mathbf{D}\tilde{\eta}_{mj} \leqslant q_m \mathbf{D}\eta_{mj}. \tag{9.5}$$

In fact,

$$\mathbf{D}\tilde{\eta}_{mj} = \mathbf{M}\tilde{\eta}_{mj}^2 - S_{mj}^2 \leqslant q_m \mathbf{M}\tilde{\eta}_{mj} - q_m S_{mj}^2 - (1 - q_m)S_{mj}^2$$

$$= q_m(S_{mj} - S_{mj}^2) - (1 - q_m)S_{mj}^2,$$

and since $q_m \leqslant 1$ it follows that $\mathbf{D}\tilde{\eta}_{mj} \leqslant q_m(S_{mj} - S_{mj}^2) = q_m \mathbf{D}\eta_{mj}$.

The estimate (9.5) explains the colossal decrease in dispersion (compared with the simulation estimate) that will occur if $\tau \ll 1$:

$$q_m \leqslant w_m = \prod_{i=0}^{m-1} [1 - \exp(-l_i/\bar{\lambda}_i)] \sim (1 - e^{-\tau})^m \approx \tau^m.$$

And since the maximum probabilities in the spectrum S_{mj} will be of order τ^m if τ is small, they will have $\mathbf{D}\eta_{mj} \sim \tau^m$, $\mathbf{D}\bar{\eta}_{mj} \sim \tau^{2m}$.

Large depths. Figure 40 illustrates a spectrum formed by radiation emerging from a sphere with an optical radius $\tau = 20$. This spectrum has been built up by repeated Compton scatterings within the sphere. The number of trajectories included in the calculation is $N = 500$. The photon source is placed at the center of the sphere; it has a Planck spectrum with $kT_r = 0.1\ mc^2$ (curve *1*). Curve 2, a Wien spectrum with $kT_e = 0.01\ mc^2$, is obtained in the limit $\tau \to \infty$. This example demonstrates that by using weights to allow for particle escape one can deal with problems in which the depth is very substantial.

Absorption weighting. Suppose that in a collision event a model particle may be either scattered or absorbed, and assume that the absorption probability p_a can be computed at any point of the collision. In a simulation one would have to make a draw for the type of interaction in each collision; for example, if $\xi < p_a$, absorption would occur and the trajectory would end, while if $\xi \geqslant p_a$, scattering would take place and the trajectory would continue.

Alternatively, let us assume that prior to the ith collision the particle has the weight w_i. In the collision "a portion" of the particle, with weight $p_a w_i$, will be absorbed, while "the remainder," with weight $w_i - p_a w_i$, will be scattered. This modeling technique will lengthen the trajectory, but the information that can be derived from each trajectory is far richer now: instead of the whole particle being absorbed at a single point, we will have a set of points with fractional amounts of absorption, reflecting to some degree the manner in which absorption is distributed over the region under consideration.

Example: photoabsorption (compare the example in Sec. 9.1). Instead of modeling the outcome of a collision between a photon and an iron ion, we now regard a $K\alpha$ photon as appearing each time; but if the weight of an absorbed photon prior to collision was w_i, the weight of the resultant $K\alpha$ photon will be $w_{i+1} = 0.34 w_i$.

Systematic sampling. Quite a few different procedures are available for

introducing statistical weights into various problems (Sobol' 1973). We shall illustrate the situation by considering just one method, called systematic sampling.

Our task was to model in some fashion a hard radiation spectrum in which the photon frequencies are distributed with a density $p(\nu) = A\nu^{-2}$ for 50 eV $< h\nu <$ 10 MeV. The inverse-function method easily enabled us to derive a modeling formula, but when that formula was put into use, practically no photons of energy above 1 MeV (the ones whose contribution would have been of special interest) were produced, as the probability of their being formed was only $\approx 5 \times 10^{-5}$.

In this example it proved helpful to introduce statistical weights. The frequency interval was divided into a finite number M of subintervals, and frequencies for newly produced photons were drawn from all these intervals in turn. To each such photon an initial weight w_0 was assigned, proportional to the production probability in the corresponding frequency interval. With this modeling technique the number N of model photons has to be a multiple of the number M of intervals.

9.4 *Modeling Photons and Electrons*

Energy of Planck photons. At radiation temperature T_r the number density of photons having an energy $E = h\nu$ is expressed by

$$p(E) = \frac{1}{2\zeta(3)} b^3E^2(e^{bE} - 1)^{-1},$$

where $b = 1/kT_r$; $\zeta(3) = \sum_1^\infty m^{-3} = 1.202$ is the Riemann zeta function.

The function $(e^{bE} - 1)^{-1}$ is easily expanded in powers of e^{-bE}. Introducing the normalized densities $p_m(E) = \frac{1}{2}m^3b^3E^2e^{-bmE}$, we can write the expansion as

$$p(E) = (1.202)^{-1} \sum_{m=1}^{\infty} m^{-3}p_m(E),$$

This expression shows that $p(E)$ may conveniently be modeled by the superposition method: each of the densities $p_m(E)$ represents a gamma distribution and would be modeled by the formula given in Sec. 9.1.

To draw a value for the energy $E = h\nu$ we select four random numbers $\zeta_1, \ldots, \zeta_4$. From ζ_1 we define an auxiliary random number α such that

$$\alpha = \begin{cases} 1 & \text{if} \quad 1.202\xi_1 < 1, \\ m & \text{if} \quad \sum_{1}^{m-1} j^{-3} \leqslant 1.202\xi_1 < \sum_{1}^{m} j^{-3}, \end{cases}$$

where $m = 2, 3, \ldots$; then we set $h\nu = -(kT_r/\alpha) \ln (\xi_2\xi_3\xi_4)$. On the average, $\zeta(2)/\zeta(3) = 1.37$ attempts will be needed to draw the number α. A similar modeling algorithm has been used by Fleck and Cummings (1971).

Momentum of relativistic electrons. The number of Maxwellian electrons having momentum $\mathbf{p}$ is expressed by $N(\mathbf{p})d\mathbf{p} = \exp[-(p^2c^2 + m^2c^4)^{1/2}/kT_e]d\mathbf{p}$. If all directions $\mathbf{p}$ are equally probable, the density of p will be proportional to $p^2 \exp[-(p^2c^2 + m^2c^4)^{1/2}/kT_e]$. Introducing the dimensionless energy $n = kT_e/mc^2$ and momentum $\eta = p/mc$, we have for the density of η:

$$p(x) = B_2x^2 \exp\left(-\frac{1}{n}\sqrt{1 + x^2}\right),$$

where $0 < x < \infty$ and the normalizing constant B_2 is given in terms of the Macdonald function by $B_2 = [nK_2(1/n)]^{-1}$ (Abramowitz and Stegun 1964).

Low-temperature case (Sobol' 1981). We change from the random variable η to a new random variable, the energy of motion $\zeta = (\sqrt{1 + \eta^2} - 1)/n$; thus $\eta = [n\zeta(2 + n\zeta)]^{1/2}$. The probability density of ζ will be $p_\zeta(z) = B_2ne^{-1/n}(2nz + n^2z^2)^{1/2}(1 + nz)e^{-z}$, which may be expressed in the product form (9.2):

$$p_\zeta(z) = k_1p_{\zeta'}(z)(2nz + n^2z^2)^{1/2}(1 + nz)e^{-z/3}, \tag{9.6}$$

where $p_{\zeta'}(z) = \frac{2}{3}e^{-2z/3}$, so that ζ' can easily be modeled. The constant factor $k_1 = \frac{3}{2}B_2ne^{-1/n}$.

To construct a rejection technique corresponding to the representation (9.6), one must prove that the functional factor in that expression is bounded. That will not be true, however, for all n. Define $\psi(y) = (2y + y^2)^{1/2}$

$(1 + y)e^{-y/3n}$; then one can easily verify that the functional factor in Eq. (9.6) is $\psi(nz)$. The following statement holds regarding the boundedness of ψ:

If $n \leqslant \frac{2}{7}$, then $\psi(y) \leqslant 3(2n/e)^{1/2}$ for all y, $0 \leqslant y < \infty$. From this inequality we can formulate a rejection technique for modeling η:

If $n \leqslant 0.29$ (equivalently, if $kT_e \leqslant 150$ keV), we select two random numbers ξ_1, ξ_2 and compute the auxiliary quantity $\zeta' = -\frac{3}{2} \ln \xi_1$. Then if the selection criterion $\xi_2^2 < 0.151(1 + n\zeta')^2\zeta'(2 + n\zeta')\xi_1$ is satisfied, we set $\eta = [n\zeta'(2 + n\zeta')]^{1/2}$; otherwise we select new ξ_1, ξ_2.

The efficiency of this method is given by Eq. (9.3): $\mathfrak{E} = 0.259n^{-1/2}e^{1/n}K_2(1/n)$. Some typical efficiencies are:

n	0.29	0.25	0.20	0.10	0
$\mathfrak{E}$	0.52	0.49	0.46	0.39	0.33

Curiously, the algorithm remains quite efficient as $n \to 0$, relieving us of the need to use the nonrelativistic Maxwell distribution with corrections (Corman 1970) for very small n.

High-temperature case. A highly efficient procedure for modeling the momentum in this case has been described by one of the authors (Sobol' 1976). For the density of η one adopts the product representation

$$p(x) = 2n^3B_2p_{\eta'}(x)f(x), \tag{9.7}$$

where $p_{\eta'}(x) = (2n^3)^{-1}x^2e^{-x/n}$. The functional factor is bounded:

$$f(x) = \exp\left[-\frac{1}{n}(\sqrt{1 + x^2} - x)\right] \leqslant 1.$$

The density $p_{\eta'}(x)$ is the density of a gamma distribution with the parameter $m = 3$; an expression for modeling η' has been given in Sec. 9.1. The rejection technique corresponding to the representation (9.7) may be formulated as follows. We select four random numbers $\xi_1, \ldots, \xi_4$ and compute the two quantities $\eta' = -n \ln (\xi_1\xi_2\xi_3)$, $\eta'' = -n \ln (\xi_1\xi_2\xi_3\xi_4)$. If $(\eta'')^2 - (\eta')^2 > 1$ we set $\eta = \eta'$; otherwise we draw new numbers $\xi_1, \ldots, \xi_4$.

By Eq. (9.3) the selection efficiency $\mathfrak{E} = (2n^2)^{-1}K_2(1/n)$. For $n \geq 1$ it is very high ($\mathfrak{E} \to 1$ as $n \to \infty$), but for small n it falls off rapidly:

n	1.0	0.5	0.29	0.25	0.20	0.10
$\mathfrak{E}$	0.81	0.51	0.21	0.14	0.066	0.001

The method is therefore recommended only for large n, when the foregoing method is inapplicable—that is, for $n > 0.29$, or equivalently, for $kT_e \geq 150$ keV.

Scattering cross section. The cross section $\sigma(x) = 2\pi r_e^2 \hat{\sigma}(x)$ for scattering of a photon by an electron is well established, but the conventional equation,

$$x\hat{\sigma}(x) = \left(1 - \frac{4}{x} - \frac{8}{x^2}\right) \ln (1 + x) + \frac{1}{2} + \frac{8}{x} - \frac{1}{2(1 + x)^2}$$

(see below for the definition of x), is inconvenient for calculations when $x \ll 1$ and is rather cumbersome to integrate. We therefore approximate $\hat{\sigma}(x)$ to high accuracy by means of the simpler functions

$$\hat{\sigma}(x) = \begin{cases} \frac{1}{3} + 0.141x - 0.12x^2 + (1 + 0.5x)(1 + x)^{-2}, & x \leq 0.5; \\ [\ln (1 + x) + 0.06]x^{-1}, & 0.5 \leq x \leq 3.5; \\ [\ln (1 + x) + 0.5 - (2 + 0.076x)^{-1}]x^{-1}, & 3.5 \leq x. \end{cases}$$

The error of this fit is no more than 1 percent.

We will need below to evaluate the function $\Phi(x) = \int_0^x x\hat{\sigma}(x)dx$. By integrating the approximations to $x\hat{\sigma}(x)$ we obtain the computation formulas

$$\Phi(x) = \begin{cases} \frac{1}{6}x^2 + 0.047x^3 - 0.03x^4 + \frac{1}{2}x^2(1 + x)^{-1} & 0 \leq x \leq 0.5; \\ (1 + x) \ln (1 + x) - 0.94x - 0.00925, & 0.5 \leq x \leq 3.5; \\ (1 + x) \ln (1 + x) - \frac{1}{2}x & \\ \qquad - 13.16 \ln (2 + 0.076x) + 9.214, & 3.5 \leq x. \end{cases}$$

Photon mean free path. A photon of energy $h\nu$ and with its momentum in direction $\mathbf{\Omega}$ will have a mean free path

$$\bar{\lambda} = \frac{\int N(\mathbf{p})d\mathbf{p}}{N_e \int \sigma(x)(1 - \mathbf{\Omega} \cdot \mathbf{v}/c)N(\mathbf{p})d\mathbf{p}},$$

where the scattering cross section $\sigma(x)$ and the function $N(\mathbf{p})$ have been defined above. The quantity $x = H\gamma(1 - \mathbf{\Omega} \cdot \mathbf{v}/c)$, with $H = 2h\nu/mc^2$.

Since all directions of $\mathbf{p}$ are equally probable, we align the polar axis with $\mathbf{\Omega}$ and introduce spherical coordinates p, θ, φ to obtain the expression

$$\bar{\lambda} = \frac{4\pi \int_0^\infty e^{-\gamma/n} p^2 dp}{2\pi N_e \int_0^\infty e^{-\gamma/n} p^2 dp \int_{-1}^{1} \sigma(x)[1 - (v/c)\cos\theta] d\cos\theta}$$

The integration over $\cos\theta$ is readily converted to an integration over x, because if γ is fixed, $dx = -H\gamma(v/c)d\cos\theta$. Then retaining the notation of the preceding paragraph we find that

$$\int_{-1}^{1} \sigma(x)\left(1 - \frac{v}{c}\cos\theta\right) d\cos\theta = \frac{2\pi r_e^2}{(H\gamma)^2 v/c} \int_{H\gamma(1-v/c)}^{H\gamma(1+v/c)} x\hat{\sigma}(x)dx$$

$$= \frac{2\pi r_e^2}{H^2\gamma\sqrt{\gamma^2 - 1}} [\Phi(x)]_{x=H\gamma^-}^{x=H\gamma^+},$$

where $\gamma^{\pm} = \gamma \pm \sqrt{\gamma^2 - 1}$.

We substitute this expression into the last formula for $\bar{\lambda}$, note that $\pi r_e^2 N_e = \frac{3}{8}\sigma_T N_e = 0.375\ \tau/R$, and change from an integration over p to an integration over γ (using $p = mc\sqrt{\gamma^2 - 1}$). As a result we finally obtain for the mean free path:

$$\bar{\lambda} = \frac{H^2 \int_1^\infty e^{-\gamma/n} \gamma\sqrt{\gamma^2 - 1}\, d\gamma}{0.375 \frac{\tau}{R} \int_1^\infty e^{-\gamma/n} \left[\Phi(x)\right]_{H\gamma^-}^{H\gamma^+} d\gamma}.$$

Even though the integral in the numerator can be evaluated exactly, we have preferred to compute both integrals (numerator and denominator) numerically at the same integration points. They are both of the form $\int_1^\infty e^{-\gamma/n}\,\Psi(\gamma)d\gamma$. The change of variables $u = \exp[(1 - \gamma)/n]$ transforms the semiaxis $(1, \infty)$ into the interval $(0, 1)$, and the resulting integral can be calculated from the rectangle formula:

$$\int_1^\infty e^{-\gamma/n}\,\Psi(\gamma)d\gamma = ne^{-1/n}\int_0^1 \Psi(1 - n\ln u)du$$

$$\approx \frac{ne^{-1/n}}{\tilde{N}}\sum_{\beta=1}^{\tilde{N}}\Psi\left(1 - n\ln\frac{\beta - \frac{1}{2}}{\tilde{N}}\right).$$

The factor $ne^{-1/n}$ occurs in both integrals and cancels out.

The final computation formulas are as follows:

a) Abscissas of integration $\tilde{\gamma}_\beta = 1 - n\ln[(\beta - \frac{1}{2})/\tilde{N}]$, $\beta = 1, 2, \ldots, \tilde{N}$.

b) The constant quantity

$$g = \frac{1}{0.375(\tau/R)}\sum_{\beta=1}^{\tilde{N}}\tilde{\gamma}_\beta\sqrt{(\tilde{\gamma}_\beta)^2 - 1}.$$

c) The general equation

$$\bar{\lambda} = \frac{gH^2}{\sum_{\beta=1}^{\tilde{N}}[\Phi(x)]_{H\tilde{\gamma}_\beta^-}^{H\tilde{\gamma}_\beta^+}}.$$

d) Case $H \ll 1$. As $H \to 0$ the expression for $\bar{\lambda}$ reduces to an indeterminate form, with $\lim_{H\to 0}\bar{\lambda} = (\tau/R)^{-1}$. We therefore supplement the expression (*c*): if the largest abscissa used in the numerical integration, $\tilde{\gamma}_1 = 1 + n\ln(2\tilde{N})$, and the energy $H = 2h\nu(mc^2)^{-1}$ satisfy the condition $2\tilde{\gamma}_1 H \leqslant 0.01$, then instead of using the equation (*c*) we set $\bar{\lambda} = (\tau/R)^{-1}$.

In our calculations we have adopted the value $\tilde{N} = 40$ (sometimes $\tilde{N} = 20$).

Power-law relativistic-electron spectra. We shall regard the number of electrons with γ values corresponding to the interval $(x, x + dx)$ as given

by $N(x)dx = \chi(x)(\gamma_0/x)^{5/2} \exp(-\gamma_0/x)dx$, where $1 < x < \infty$. The factor $\chi(x) = 1/x$ if $x > \gamma_1$; $\chi(x) = 1/\gamma_1$ if $1 < x < \gamma_1$. In our calculations we have set $\gamma_0 = 30$, $\gamma_1 = 6000$.

We now make the change of variables $y = \gamma_0/x$, so that $0 < y < \gamma_0$, and we introduce the new random variable $\eta = \gamma_0/\gamma$. Then the normalized density of η will be $p(y) = c_0\Psi(y)y^{1/2}e^{-y}$, where $\Psi(y) = \gamma_0\chi(x)$ and c_0 is a normalizing constant. Defining $\kappa = \gamma_0/\gamma_1$, we may write $\Psi(y) = y$ for $0 < y < \kappa$, $\Psi(y) \equiv \kappa$ for $\kappa < y < \gamma_0$. Further, let us agree that $\Psi(y) \equiv 0$ for $y > \gamma_0$; the density $p(y)$ will then be defined for all $0 < y < \infty$.

As an auxiliary quantity we shall adopt a random variable η' with the density $p_1(y) = 2\pi^{-1/2}y^{1/2}e^{-y}$ $(0 < y < \infty)$, which represents a gamma distribution with parameter $m = \frac{3}{2}$. We write the density $p(y)$ in the product form (9.2): $p(y) = \frac{1}{2}c_0\pi^{1/2}p_1(y)\Psi(y)$, where the functional factor is confined to the interval $0 \leqslant \Psi(y) \leqslant \kappa$. Since we know how to model gamma distributions with a half-integer parameter m (Sec. 9.1), we arrive at the following rejection technique for modeling η, and accordingly γ as well:

a) Drawing three random numbers ξ_1, ξ_2, ξ_3, we compute $\eta' = -\ln \xi_1 - (\ln \xi_2) \sin^2 2\pi\xi_3$.

b) If $\kappa < \eta' < \gamma_0$, set $\gamma = \gamma_0/\eta'$.

c) If $\eta' < \kappa$, draw another random number ξ_4 and test the condition $\kappa\xi_4 < \eta'$. If it is satisfied, set $\gamma = \gamma_0/\eta'$; otherwise return to step (*a*).

d) If $\gamma_0 < \eta'$, return to step (*a*).

According to Eq. (9.3) the efficiency of such a selection will be

$$\mathfrak{E} = \frac{2}{\sqrt{\pi}}\left(\frac{1}{\kappa}\int_0^{\kappa} y^{3/2}e^{-y}dy + \int_{\kappa}^{\gamma_0} y^{1/2}e^{-y}dy\right),$$

and for our values of the parameters γ_0 and γ_1, $\mathfrak{E} \approx 1$.

Remark. With an electron spectrum of the type considered here, a change should be made in the final expression for $\bar{\lambda}$: the factor $e^{-\gamma/n}$ in the numerator and denominator should be replaced by $N(\gamma)/\gamma\sqrt{\gamma^2 - 1}$.

9.5 *Modeling Compton Scattering*

Selection of scattering electron. The probability density of the momenta $\mathbf{p}$ of the scattering electrons is proportional to the quantity $\sigma(x)(1 - \boldsymbol{\Omega} \cdot \mathbf{v}/c)N(\mathbf{p})$ appearing in the expression for $\bar{\lambda}$. Since we are capable of modeling the momentum $\mathbf{p}$ for a Maxwellian density, proportional to $N(\mathbf{p})$, it has

proved very convenient to apply a rejection technique (9.2) wherein the density is represented in product form as $p(\mathbf{p}) = k_1 N_1(\mathbf{p}) f(\mathbf{p})$. Here $N_1(\mathbf{p}) = N(\mathbf{p})/\int N(\mathbf{p}) d\mathbf{p}$ is the normalized Maxwellian density; the functional factor $f(\mathbf{p}) = \hat{\sigma}(x)(1 - \mathbf{\Omega} \cdot \mathbf{v}/c)$, and the constant $k_1 = 2\pi r_e^2 N_e \bar{\lambda}$. It is easily shown that the functional factor is bounded: $f(\mathbf{p}) \leqslant 2\,\hat{\sigma}(x) \leqslant \frac{8}{3}$.

We have, then, the following method. Modeling the momentum $\mathbf{p}$ according to Sec. 9.4, we compute $\mathbf{v}$, x, and $\hat{\sigma}(x)$. We take one more random number ξ and test the selection criterion $\xi < 0.375\hat{\sigma}(x)(1 - \mathbf{\Omega} \cdot \mathbf{v}/c)$. If it is satisfied, $\mathbf{p}$ will be accepted; otherwise we choose a new $\mathbf{p}$.

By Eq. (9.3) the efficiency of the selection will be $\mathcal{E} = \frac{3}{8}(2\pi r_e^2 N_e \bar{\lambda})^{-1} = (2\bar{\lambda}\tau/R)^{-1}$. For $x \ll 1$, when $\bar{\lambda} \approx R/\tau$, we will have $\mathcal{E} \approx \frac{1}{2}$; but as x increases, with $\sigma(x)$ diminishing, the efficiency will decrease as well.

In our 1976–1979 papers we regarded the distribution of scattering electrons as identical with the distribution of electrons in space, and we took values for their momenta according to Sec. 9.4, for a density $N_1(\mathbf{p})$. Actually that approach is tenable only if τ is small and the temperature is not too high. We are indebted to W. Wielczewski (Warsaw) for drawing our attention to this inaccuracy. The results presented in this paper (except for Figures 38) have all been developed by means of the rejection technique described above.

Choice of coordinate system. Let the vector $\mathbf{v}^0 = v_1^0\mathbf{i} + v_2^0\mathbf{j} + v_3^0\mathbf{k}$. Assume that $\rho^2 = (v_1^0)^2 + (v_2^0)^2 > 0$, and introduce the unit vectors $\mathbf{w}^0 = (v_2^0\mathbf{i} - v_1^0\mathbf{j})/\rho$, $\mathbf{t}^0 = (v_1^0 v_3^0\mathbf{i} + v_2^0 v_3^0\mathbf{j} - \rho^2\mathbf{k})/\rho$, which together with $\mathbf{v}^0$ form an orthonormal triad. The direction of the vector $\mathbf{\Omega}'$ may conveniently be expressed in the coordinate system $\mathbf{v}^0$, $\mathbf{w}^0$, $\mathbf{t}^0$:

$$\mathbf{\Omega}' = \mu'\mathbf{v}^0 + (1 - \mu'^2)^{1/2}(\mathbf{w}^0 \cos\varphi' + \mathbf{t}^0 \sin\varphi'),$$

where φ' denotes the azimuthal scattering angle, measured from the direction $\mathbf{w}^0$ in a plane perpendicular to $\mathbf{v}^0$.

By substituting the expressions for $\mathbf{w}^0$, $\mathbf{t}^0$ into this last equation, we can readily obtain expressions for the components of $\mathbf{\Omega}'$ in the stationary coordinate system $\mathbf{i}$, $\mathbf{j}$, $\mathbf{k}$:

$$\Omega_1' = \mu' v_1^0 + (1 - \mu'^2)^{1/2}\rho^{-1}(v_2^0 \cos\varphi' + v_1^0 v_3^0 \sin\varphi'),$$

$$\Omega_2' = \mu' v_2^0 + (1 - \mu'^2)^{1/2}\rho^{-1}(-v_1^0 \cos\varphi' + v_2^0 v_3^0 \sin\varphi'),$$

$$\Omega_3' = \mu' v_3^0 - (1 - \mu'^2)^{1/2}\rho \sin\varphi'.$$

The scattering angle can then of course be computed from the relation

$$\boldsymbol{\Omega} \cdot \boldsymbol{\Omega}' = \Omega_1\Omega_1' + \Omega_2\Omega_2' + \Omega_3\Omega_3'.$$

The joint distribution density of the random variables μ' and φ' is given by $p(\mu', \varphi') = \sigma^{-1}d\sigma/d\boldsymbol{\Omega}$. [In Sec. 2 we have given expressions for the differential scattering cross section, Eq. (2.8), and the change in the frequency of a photon when it is scattered, Eq. (2.4).] It is not hard to show (Sobol' 1978) that the joint density can be written in product form:

$$p(\mu', \varphi') = \frac{1}{\hat{\sigma}} p_1(\mu', \varphi')Y, \tag{9.8}$$

where the normalized density $p_1(\mu', \varphi') = [4\pi\gamma^2(1 - \mu' v/c)^2]^{-1}$ and the functional factor Y is bounded:

$$Y = (x'/x)^2 X \leqslant 2. \tag{9.9}$$

The factor $1/\hat{\sigma}$ is independent of μ' and φ', and plays the role of a constant.

Modeling algorithm. Since the random variables μ_1', φ_1' with their density $p_1(\mu', \varphi')$ can easily be modeled by the inverse-function method, the representation (9.8) enables us to devise a rejection technique for modeling μ', φ'. We assume that the quantities x and μ have already been computed.

a) We take two random numbers ξ_1, ξ_2 and compute a possible direction of scattering [for the density $p_1(\mu', \varphi')$]:

$$\mu' = \frac{v/c + 2\xi_1 - 1}{1 + (v/c)(2\xi_1 - 1)}, \qquad \varphi' = 2\pi\xi_2$$

(rather than μ_1', φ_1' we shall write μ', φ', keeping in mind that these are not yet the final quantities).

b) We compute the vector $\boldsymbol{\Omega}'$, the scattering angle $\boldsymbol{\Omega} \cdot \boldsymbol{\Omega}'$, and then the ratio

$$\frac{x'}{x} = \left[1 + \frac{h\nu(1 - \boldsymbol{\Omega} \cdot \boldsymbol{\Omega}')}{\gamma mc^2(1 - \mu' v/c)}\right]^{-1}$$

as well as the factor Y from Eq. (9.9).

c) We draw a random number ξ_3 and test the selection condition $2\xi_3 < Y$. If it is satisfied, the direction $\mathbf{\Omega}'$ will be accepted, and the new photon energy will be $h\nu' = x'[2\gamma(1 - \mu' v/c)]^{-1}mc^2$; if instead $2\xi_3 \geqslant Y$, we return to step (*a*).

By Eq. (9.3) the selection efficiency $\mathfrak{E} = \frac{1}{2}\hat{\sigma}(x)$. As $x \to 0$, $\mathfrak{E}$ tends to $\frac{2}{3}$; but as x increases the efficiency diminishes: $\mathfrak{E}(10) = 0.13$, $\mathfrak{E}(100) = 0.025$. In general, $\mathfrak{E}(x) \sim (2x)^{-1} \ln (x + 1)$ as $x \to \infty$.

Remark. The scattering equations have here been written in a coordinate system different from the one used previously (Sobol' 1978); they enable one to calculate all three components of $\mathbf{\Omega}'$, not just the angle between $\mathbf{\Omega}'$ and $\mathbf{r}$. These equations may also be used in the case $\mathbf{v} = 0$: the vector $\mathbf{v}^0$ can then be chosen arbitrarily, provided only that $\mathbf{v}^0 \neq \mathbf{k}$.

9.6 *Sample Calculation Procedure*

As an illustration of the Monte Carlo approach we shall describe a scheme for calculating a very simple model of a compact x-ray source.

Statement of problem. An isotropic source of low-frequency photons with a Planck spectrum and a radiation temperature T_r is placed at the center of a sphere of radius R filled with Maxwellian electrons whose temperature is T_e. The optical depth τ with respect to electron scattering is specified. We are to calculate the spectrum of the radiation emerging from the sphere.

We begin by adopting a grid of energy values $E = h\nu$ (in the calculations discussed in this review we have usually set $E_0 = 0$, $E_j = 10^{-9+0.2(j-1)}$ for $j = 1, 2, \ldots, 61$, and $E_{62} = 10^{10}$), a cutoff parameter ϵ, and several values for the number of trials N.

Start of trajectory. Setting $x_0 = y_0 = z_0 = 0$, $\Omega_{01} = 1$, $\Omega_{02} = \Omega_{03} = 0$, $w_0 = 1$, we apply the equations of Sec. 9.4 to find a value for $h\nu_0$.

Transition from ith to (i + 1)-th collision ($i = 0, 1, \ldots$).

a) We compute $\bar{\lambda}_i$ from the equations of Sec. 9.4 (the abscissas $\tilde{\gamma}_\beta$ of the numerical integration and the constant g are evaluated only once, before starting to calculate the trajectories; the number $\tilde{N}$ should be preassigned). We compute the distance $l_i = -(\mathbf{r}_i \cdot \mathbf{\Omega}_i) + [R^2 - \mathbf{r}_i^2 + (\mathbf{r}_i \cdot \mathbf{\Omega}_i)^2]^{1/2}$ to the boundary of the sphere ($\mathbf{r}_i = \{x_i, y_i, z_i\}$), and then the escape probability $L_i = \exp(-l_i/\bar{\lambda}_i)$. To the photon escape spectrum (in the energy interval containing $h\nu_i$) we add the weight $w_i L_i$ of the "escaping part" of a photon, and we compute the weight $w_{i+1} = w_i - w_i L_i$ of the "scattered part" of the photon. If $w_{i+1} < \epsilon$, we will stop following the trajectory; otherwise the calculation will continue.

b) Drawing a value for the free path $\lambda_i = -\bar{\lambda}_i \ln [1 - \xi(1 - L_i)]$, we find the next scattering point $\mathbf{r}_{i+1} = \mathbf{r}_i + \lambda_i \boldsymbol{\Omega}_i$.

c) We select a momentum for the scattering electron. First we take a random direction for the velocity: $v_3^0 = 2\xi_1 - 1$, $v_2^0 = [1 - (v_3^0)^2]^{1/2} \sin 2\pi\xi_2$, $v_1^0 = [1 - (v_3^0)^2]^{1/2} \cos 2\pi\xi_2$. Second, we take a possible value for the momentum $\eta = p/mc$, using the equations of Sec. 9.4. Then we calculate the quantities $\gamma = (\eta^2 + 1)^{1/2}$, $v/c = \eta/\gamma$, $\mu = \mathbf{v}^0 \cdot \boldsymbol{\Omega}$, $x = 2\gamma(h\nu_i/mc^2)(1 - \mu v/c)$, $\hat{\sigma}(x)$ as in Sec. 9.4. We draw the next random number ξ and test the selection condition $\xi < 0.375\hat{\sigma}(x)(1 - \mu v/c)$. If it is satisfied, the scattering electron will be accepted; otherwise we start step (*c*) over again.

d) From the equations of Sec. 9.5 we model the scattering, and we set $\boldsymbol{\Omega}_{i+1} = \boldsymbol{\Omega}'$, $h\nu_{i+1} = h\nu'$.

Emergent radiation spectrum. We introduce the auxiliary quantity $\delta(i, j)$, equal to 1 if $h\nu_i$ belongs to the *j*th energy interval, and 0 otherwise. Following through one photon trajectory, we obtain the set of quantities

$$B(j) = \sum_{i=0}^{\infty} w_i L_i \delta(i, j)$$

characterizing "the parts" of the photon that escape with an energy in the *j*th interval, as well as the squares $B^2(j)$, which will be needed for error estimates.

The quantities $B(j)$, $B^2(j)$ are then summed over all trajectories, so that by calculating N trajectories (numbered $s = 1, 2, \ldots, N$) we will obtain the approximate spectrum

$$S_N(j) = \frac{1}{N} \sum_{s=1}^{N} [B(j)]_s$$

and its probable errors

$$\delta S_N(j) = \frac{0.675}{\sqrt{N}} \left\{ \frac{1}{N} \sum_{s=1}^{N} [B^2(j)]_s - [S_N(j)]^2 \right\}^{1/2}.$$

If the energy grid is logarithmic, as suggested above in stating the problem, the quantities $S_N(j)$ will be proportional to the intensities I_ν; if

the grid is uniform, the $S_N(j)$ will be proportional to the flux $I_\nu/h\nu$. In either case the normalization is the same:

$$\sum_j S_N(j) = 1.$$

Appendix: Expansion of Mean Free Path in Powers of $\mathrm{n} = \mathrm{kT_e/mc^2}$

Let $\bar{\lambda}_0$ denote the mean free path of a photon with respect to scattering by cool electrons: $\bar{\lambda}_0 = [N_e\sigma(H)]^{-1}$. The last expression for $\bar{\lambda}$ in Sec. 9.4 may be rewritten as

$$\frac{\bar{\lambda}}{\bar{\lambda}_0} = \frac{2H\Phi'(H)\int_1^\infty e^{-\gamma/n}\gamma\sqrt{\gamma^2-1}\,d\gamma}{\int_1^\infty e^{-\gamma/n}\,[\Phi(x)]_{H\gamma^-}^{H\gamma^+}\,d\gamma}.$$

Making the change of variables $\gamma = 1 + nz$ and abbreviating $a = H(1 + nz)$, $h = H(2nz + n^2z^2)^{1/2}$, we obtain

$$\frac{\bar{\lambda}}{\bar{\lambda}_0} = \frac{2\Phi'(H)\int_0^\infty e^{-z}(1 + nz)h\,dz}{\int_0^\infty e^{-z}[\Phi(a + h) - \Phi(a - h)]dz}.$$

The bracketed quantity in the denominator can be expanded in powers of h:

$$\Phi(a + h) - \Phi(a - h) = \int_{a-h}^{a+h}\Phi'(x)dx$$

$$= 2h\left[\Phi'(a) + \frac{h^2}{6}\Phi'''(a) + \frac{h^4}{120}\Phi^{\mathrm{V}}(a) + \ldots\right].$$

Since the derivatives

$$\Phi'(a) = \Phi'(H) + Hnz\,\Phi''(H) + \tfrac{1}{2}(Hnz)^2\,\Phi'''(H) + \ldots,$$

$$\Phi'''(a) = \Phi'''(H) + Hnz\Phi^{\mathrm{IV}}(H) + \ldots,$$

$$\Phi^{\mathrm{V}}(a) = \Phi^{\mathrm{V}}(H) + \ldots,$$

it is straightforward to expand the denominator in powers of n. Writing a similar expansion for the numerator, we can finally put the equation in the form

$$\frac{\bar{\lambda}}{\bar{\lambda}_0} = 1 + \frac{3}{2}(1 - G)n + \frac{3}{8}[(1 - G)(1 - 6G) - K]n^2 + \ldots,$$

where

$$G = [H\Phi''(H) + \tfrac{1}{3}H^2\Phi'''(H)]/\Phi'(H),$$

$$K = \tfrac{1}{3}[20H^2\Phi'''(H) + 10H^3\Phi^{IV}(H) + H^4\Phi^{V}(H)]/\Phi'(H).$$

Recall that $H = 2h\nu/mc^2$, $\Phi'(H) = H\hat{\sigma}(H)$.

The foregoing expansion, which holds for any $h\nu$, demonstrates that if $n = kT_e/mc^2$ is small (in practice, for $kT_e \lesssim 150$ keV) the ratio $\bar{\lambda}/\bar{\lambda}_0$ will depend linearly on n. In particular, for $h\nu \ll mc^2$ we will have

$$\bar{\lambda}/\bar{\lambda}_0 = 1 + 5(h\nu/mc^2)n + \tfrac{15}{4}(h\nu/mc^2)n^2 + \ldots,$$

while in the opposite limit, as $h\nu \to \infty$,

$$\bar{\lambda}/\bar{\lambda}_0 = 1 + \tfrac{3}{2}n + \tfrac{3}{8}n^2 + \ldots.$$

REFERENCES

Abramowitz, M., and I. A. Stegun (1964), ed. *Handbook of Mathematical Functions* (Natl. Bur. Stand. Appl. Math. Ser. **55**), Washington.

Akhiezer, A. I., and V. B. Berestetskiĭ (1969). *Quantum Electrodynamics*, Nauka, Moscow [Interscience Monogr. Phys. Astr. **11** (1965)].

Allen, C. W. (1973). *Astrophysical Quantities*, 3rd ed., London Univ. Press.

Angel, J. R. P. (1969). *Nature* **224,** 160.

Arons, J. (1971). *Astrophys. J.* **164,** 437.

Babuel-Peyrissac, J. P., and G. Rouvillois (1969). *J. Physique* **30,** 301.

Bahcall, J. N., and C. L. Sarazin (1978). *Astrophys. J.* **219,** 781.

Bai, T. (1980). *Astrophys. J.* **239,** 999.

Bai, T., and R. Ramaty (1978). *Astrophys. J.* **219,** 705.

Baity, W. A., R. E. Rothschild, R. E. Lingenfelter, *et al.* (1981). *Astrophys. J.* **244,** 429.

Basko, M. M. (1978). *Astrophys. J.* **223,** 268.

Basko, M. M., and R. A. Syunyaev (1976). *Mon. Not. R. Astron. Soc.* **175,** 395.

Basko, M. M., R. A. Syunyaev, and L. G. Titarchuk (1974). *Astron. Astrophys.* **31,** 249.

Becker, R. H., R. E. Rothschild, E. A. Boldt, S. S. Holt, S. H. Pravdo, P. J. Serlemitsos, and J. H. Swank (1978). *Astrophys. J.* **221,** 912.

Beĭgman, I. L. (1974). In *X Rays from the Sun and Other Cosmic Objects* [in Russian], *Itogi Nauki i Tekhniki* [Adv. Sci. Tech.], *Ser. Astron.* **9,** VINITI [All-Union Inst. Sci. Tech. Inform.], Moscow, p. 51.
Beĭgman, I. L., L. A. Vaĭnshteĭn, and R. A. Syunyaev (1968). *Usp. Fiz. Nauk* **95,** 267 [Sov. Phys. Usp. **11,** 411 (1969)].
Beĭgman, I. L., L. A. Vaĭnshteĭn, P. I. Klimuk, V. I. Sevast'yanov, I. P. Tindo, and A. I. Shurygin (1976). *Pis'ma Astron. Zh.* **2,** 386 [*Sov. Astron. Lett.* **2,** 150 (1977)].
Bisnovatyĭ-Kogan, G. S., Ya. B. Zel'dovich, and R. A. Syunyaev (1971). *Astron. Zh.* **48,** 24 [*Sov. Astron.* **15,** 17 (1971)].
Blumenthal, G. R., and R. J. Gould (1970). *Rev. Mod. Phys.* **42,** 237.
Burgess, A. (1965). *Astrophys. J.* **141,** 1588.
Canizares, C. R. (1976). *Astrophys. J.* **207,** L101.
—— (1977). *Astrophys. J.* **214,** L119.
Chandrasekhar, S. (1950). *Radiative Transfer,* Oxford Univ. Press.
Chapline, G. F., and J. Stevens (1973). *Astrophys. J.* **184,** 1041.
Colgate, S. A. (1975). *Astrophys. J.* **195,** 493.
Cooper, G. (1971). *Phys. Rev. D* **3,** 2312.
Corman, E. G. (1970). *Phys. Rev. D* **1,** 2734.
Cox, D. P., and W. H. Tucker (1969). *Astrophys. J.* **157,** 1157.
Danese, L., and G. De Zotti (1977). *Riv. Nuovo Cimento* (2) **7,** 277.
—— (1982). *Astron. Astrophys.* **107,** 39.
DeGregoria, A. J. (1974). *Astrophys. J.* **189,** 555.
Dirac, P. A. M. (1925). *Mon. Not. R. Astron. Soc.* **85,** 825.
Eardley, D. M. (1976). In *X-Ray Binaries* (Goddard Space Flight Center sympos., Oct. 1975), NASA SP-389, p. 379.
Eardley, D. M., A. P. Lightman, N. I. Shakura, S. L. Shapiro, and R. A. Syunyaev (1978). *Comments Astrophys.* **7,** 151.
Fabian, A. C., J. E. Pringle, and M. J. Rees (1976). *Mon. Not. R. Astron. Soc.* **175,** 43.
Felten, J. E., and P. Morrison (1966). *Astrophys. J.* **146,** 686.
Felten, J. E., and M. J. Rees (1972). *Astron. Astrophys.* **17,** 226.
Felten, J. E., M. J. Rees, and T. F. Adams (1972). *Astron. Astrophys.* **21,** 139.
Fleck, J. A., and L. D. Cummings (1971). *J. Comput. Phys.* **8,** 313.
Ginzburg, V. L., and S. I. Syrovatskiĭ (1964). *Zh. Éksp. Teor. Fiz.* **46,** 1865 [*Sov. Phys. JETP* **19,** 1255 (1964)].
Gould, R. J. (1972). *Ann. Physics* **69,** 321.
Grindlay, J., and H. Gursky (1976). *Astrophys. J.* **205,** L131.
Grindlay, J., H. Gursky, H. Schnopper, D. R. Parsignault, J. Heise, A. C. Brinkman, and J. Schrijver (1976). *Astrophys. J.* **205,** L127.
Hatchett, S., J. Buff, and R. McCray (1976). *Astrophys. J.* **206,** 847.
Illarionov, A. F., and R. A. Syunyaev (1972). *Astron. Zh.* **49,** 58 [*Sov. Astron.* **16,** 45 (1972)].
—— (1974*a*). *Astron. Zh.* **51,** 698 [*Sov. Astron.* **18,** 413 (1975)].
—— (1974*b*). *Astron. Zh.* **51,** 1162 [*Sov. Astron.* **18,** 691 (1975)].
Illarionov, A. F., T. Kallman, R. McCray, and R. R. Ross (1979). *Astrophys. J.* **228,** 279.
Imshennik, V. S., and Yu. I. Morozov (1981). *Radiative Relativistic Gas Dynamics of High-Temperature Phenomena* [in Russian], Atomizdat, Moscow.
Ivanov, V. V. (1969). *Radiative Transfer and the Spectra of Celestial Bodies,* Nauka, Moscow [*Transfer of Radiation in Spectral Lines* (Natl. Bur. Stand, Spec. Publ. **385**), Washington (1973)].
Jauch, J. M., and F. Rohrlich (1955). *The Theory of Photons and Electrons,* Addison-Wesley; 2nd ed., Springer (1976).
Jones, F. C. (1968). *Phys. Rev.* **167,** 1159.

Katz, J. I. (1976). *Astrophys. J.* **206,** 910.
Katz, J. I., and E. E. Salpeter (1974). *Astrophys. J.* **193,** 429.
Kestenbaum, H. L., K. S. Long, R. Novick, M. C. Weisskopf, and R. S. Wolff (1977). *Astrophys. J.* **216,** L19.
Klebesadel, R. W., I. B. Strong, and R. A. Olson (1973). *Astrophys. J.* **182,** L85.
Kolykhalov, P. I., and R. A. Syunyaev (1983). *Pis'ma Astron. Zh.* **9** [*Sov. Astron. Lett.* **9**] (in press).
Kompaneets, A. S. (1956). *Zh. Éksp. Teor. Fiz.* **31,** 876 [*Sov. Phys. JETP* **4,** 730 (1957)].
Kylafis, N. D., and D. Q. Lamb (1979). *Astrophys. J.* **228,** L105.
Landau, L. D., and E. M. Lifshits (1976). *The Classical Theory of Fields,* 4th ed., Pergamon.
Levich, E. V., and R. A. Syunyaev (1971). *Astron. Zh.* **48,** 461 [*Sov. Astron.* **15,** 363 (1971)].
Levich, E. V., R. A. Syunyaev, and Ya. B. Zel'dovich (1972). *Astron. Astrophys.* **19,** 135.
Lewin, W. H. G., J. Doty, G. W. Clark, *et al.* (1976). *Astrophys. J.* **207,** L95.
Liang, E. P. T., and R. H. Price (1977). *Astrophys. J.* **218,** 247.
Lightman, A. P. (1981). *Astrophys. J.* **244,** 392.
Lightman, A. P., and G. B. Rybicki (1979). *Astrophys. J.* **232,** 882.
Lightman, A. P., R. Giacconi, and H. Tananbaum (1978). *Astrophys. J.* **224,** 375.
Loh, E. D., and G. P. Garmire (1971). *Astrophys. J.* **166,** 301.
Lorentz, M. (1981). Max-Planck-Inst. Phys. Astrophys., Inst. Extraterr. Phys. (Garching/München), Preprint No. 171.
Lynden-Bell, D. (1969). *Nature* **223,** 690.
Lynden-Bell, D., and M. J. Rees (1971). *Mon. Not. R. Astron. Soc.* **152,** 461.
Lyubarskiĭ, Yu. É., and R. A. Syunyaev (1982). *Pis'ma Astron. Zh.* **8,** 612 [*Sov. Astron. Lett.* **8,** No. 5 (1983)].
Lyutyĭ, V. M., and R. A. Syunyaev (1976). *Astron. Zh.* **53,** 511 [*Sov. Astron.* **20,** 290 (1976)].
Matsuda, T., H. Sato, and H. Takeda (1971). *Progr. Theor. Phys.* **46,** 416.
Mazets, E. P., and S. V. Golenetskiĭ (1981). *Sov. Sci. Rev. E: Astrophys. Space Phys. Rev.* **1,** 205.
McCray, R., and F. K. Lamb (1976). *Astrophys. J.* **204,** L115.
Mitchell, R. J., J. L. Culhane, P. J. N. Davison, and J. C. Ives (1976). *Mon. Not. R. Astron. Soc.* **175,** 29P.
Miyamoto, S. (1978). *Astron. Astrophys.* **63,** 69.
Neugebauer, G., J. B. Oke, E. Becklin, and G. Garmire (1969). *Astrophys. J.* **155,** 1.
O'Dell, S. L. (1981). *Astrophys. J.* **243,** L147.
Osterbrock, D. E. (1962). *Astrophys. J.* **135,** 195.
Payne, D. G. (1980). *Astrophys. J.* **237,** 951.
Perotti, F., A. Della Ventura, G. Sechi, *et al.* (1979). *Nature* **282,** 484.
Peyraud, P. (1968). *J. Physique* **29,** 88, 306, 872.
Pozdnyakov, L. A., I. M. Sobol', and R. A. Syunyaev (1976). *Pis'ma Astron. Zh.* **2,** 140 [*Sov. Astron. Let.* **2,** 55 (1976)].
—— (1977). *Astron. Zh.* **54,** 1246 [*Sov. Astron.* **21,** 708 (1978)].
—— (1979*a*). *Astron. Astrophys.* **75,** 214.
—— (1979*b*). *Pis'ma Astron. Zh.* **5,** 279 [*Sov. Astron. Lett.* **5,** 149 (1979)].
Pravdo, S. H., and R. F. Mushotzky (1980). Preprint.
Pravdo, S. H., R. H. Becker, E. A. Boldt, S. S. Holt, P. J. Serlemitsos, and J. H. Swank (1977). *Astrophys. J.* **215,** L61.
Pringle, J. E., and M. J. Rees (1972). *Astron. Astrophys.* **21,** 1.
Rees, M. J. (1967). *Mon. Not. R. Astron. Soc.* **137,** 429.
Ross, R. R., R. Weaver, and R. McCray (1978). *Astrophys. J.* **219,** 292.
Rybicki, G. B., and A. P. Lightman (1979). *Radiative Processes in Astrophysics,* Wiley.

Serlemitsos, P. J., B. W. Smith, E. A. Boldt, S. S. Holt, and J. H. Swank (1977). *Astrophys. J.* **211,** L63.
Shakura, N. I., and R. A. Syunyaev (1973). *Astron. Astrophys.* **24,** 337.
—— (1976). *Mon. Not. R. Astron. Soc.* **175,** 613.
Shapiro, S. L., A. P. Lightman, and D. M. Eardley (1976). *Astrophys. J.* **204,** 187.
Shklovskiĭ, I. S. (1967). *Astron. Zh.* **44,** 930 [*Sov. Astron.* **11,** 749 (1968)].
Shulman, S., H. Friedman, G. Fritz, R. C. Henry, and D. J. Yentis (1975). *Astrophys. J.* **199,** L101.
Sobol', I. M. (1973). *Numerical Monte Carlo Methods* [in Russian], Nauka, Moscow, 311 pp.; *The Monte Carlo Method,* Univ. Chicago Press (1974), 67 pp.
—— (1976). In *Monte Carlo Methods in Computational Mathematics and Mathematical Physics* [in Russian], Computation Center Siber. Branch USSR Acad. Sci., Novosibirsk, p. 24.
—— (1978). *Vychisl. Mat. Mat. Fiz.* **18,** 1034 [*USSR Comput. Math. Math. Phys.* **18,** No. 4, 217 (1979)].
—— (1981). In *Voprosy Kibernetiki* No. 82, Moscow.
Sobolev, V. V. (1967). *A Course in Theoretical Astrophysics* [in Russian], Nauka, Moscow; 2nd ed. (1975).
Syunyaev [Sunyaev], R. A. (1971). *Astron. Zh.* **48,** 244 [*Sov. Astron.* **15,** 190 (1971)].
—— (1976). *Pis'ma Astron. Zh.* **2,** 287 [*Sov. Astron. Lett.* **2,** 111 (1976)].
—— (1980). *Pis'ma Astron. Zh.* **6,** 387 [*Sov. Astron. Lett.* **6,** 213 (1981)].
—— (1983). *Pis'ma Astron. Zh.* **9** [*Sov. Astron. Lett.* **9**] (in press).
Syunyaev, R. A., and L. G. Titarchuk (1980). *Astron. Astrophys.* **86,** 121.
—— (1983). In press.
Syunyaev, R. A., and J. Trümper (1979). *Nature* **279,** 506.
Syunyaev, R. A., and Ya. B. Zel'dovich (1970). *Astrophys. Space Sci.* **7,** 20.
—— (1980). *Ann. Rev. Astron. Astrophys.* **18,** 537.
Takahara, F. (1980). *Progr. Theor. Phys.* **63,** 1551.
—— (1981). *Progr. Theor. Phys.* **65,** 883.
Thorne, K. S. (1981). *Mon. Not. R. Astron. Soc.* **194,** 439.
Tucker, W. H., and M. Koren (1971). *Astrophys. J.* **168,** 283.
Vaĭnshteĭn, L. A., and R. A. Syunyaev (1982). *Preprint Inst. Kosm. Issled. Akad. Nauk SSSR.*
Weaver, T. A., and G. F. Chapline (1974). *Astrophys. J.* **192,** L57.
Weymann, R. (1965). *Phys. Fluids* **8,** 2112.
—— (1967). *Astrophys. J.* **147,** 887.
White, R. S., B. Dayton, R. Gibbons, J. L. Long, E. M. Zanrosso, and A. D. Zych (1980). *Nature* **284,** 608.
Woodward, P. (1970). *Phys. Rev. D* **1,** 2731.
Worrall, D. M., R. F. Mushotzky, E. A. Boldt, S. S. Holt, and P. J. Serlemitsos (1979). *Astrophys. J.* **232,** 683.
Zel'dovich, Ya. B., and E. V. Levich (1970). *Pis'ma Zh. Éksp. Teor. Fiz.* **11,** 57 [*JETP Lett.* **11,** 35 (1970)].
Zel'dovich, Ya. B., and N. I. Shakura (1969). *Astron. Zh.* **46,** 225 [*Sov. Astron.* **13,** 175 (1969)].
Zel'dovich, Ya. B., and R. A. Syunyaev (1969). *Astrophys. Space Sci.* **4,** 301.
Zel'dovich, Ya. B., E. V. Levich, and R. A. Syunyaev (1972). *Zh. Éksp. Teor. Fiz.* **62,** 1392 [*Sov. Phys. JETP* **35,** 733 (1973)].